Structure and physical properties of transition metal based compounds

STRUCTURE AND PHYSICAL PROPERTIES OF TRANSITION METAL BASED COMPOUNDS

BY

SHEIKH JAMIL AHMED, M.Sc.

A THESIS

SUBMITTED TO THE DEPARTMENT OF MATERIALS SCIENCE & ENGINEERING

AND THE SCHOOL OF GRADUATE STUDIES

OF MCMASTER UNIVERSITY

IN PARTIAL FULFILMENT OF THE REQUIREMENTS

FOR THE DEGREE OF

DOCTOR OF PHILOSOPHY

Doctor of Philosophy (2018) McMaster University

(Materials Science & Engineering) Hamilton, Ontario, Canada

TITLE:	Structure and physical properties of transition metal based compounds
AUTHOR:	Sheikh Jamil Ahmed M.Sc., (Physics) Lakehead University, Thunder Bay, Ontario
SUPERVISOR:	Dr. Marek Niewczas
NUMBER OF PAGES:	xxv, 147

Dedicated to my parents, wife and son.

Abstract

Crystalline systems formed with transition metal elements tend to exhibit strong magneto-structural coupling that gives rise to unusual but exciting physical phenomena in these materials. In this dissertation, we present our findings from the studies of structural and physical properties of single phase compounds Co_2MnSi, $Ni_{16}Mn_6Si_7$ and $Mn(Ni_{0.6}Si_{0.4})_2$. In addition, the stability of a Ni_2MnSi composition in a multiphase system is discussed by both theoretical and experimental approaches. All the works have been conducted with a focus on explaining the fundamental behaviors of these systems that have not been adequately addressed by other studies in the literature.

We present an experimental and theoretical investigation of the half-metallic Heusler compound, Co_2MnSi to address disorder occupancies and magnetic interactions in the material. Contrary to previous studies, our neutron diffraction refinement of the polycrystalline sample reveals almost identical amount of Mn and Co antisite disorders of $\sim$6.5% and $\sim$7.6%, respectively which is also supported explicitly by our first-principles calculations on the system with defects. A reduction of the net moment of Co_2MnSi due to an antiferromagnetic interaction introduced by disordered Mn is observed by our theoretical study. The neutron refinements at 298 K, 100 K, and 4 K further supports such reduction of moments. The work also reports the growth of single crystal by the Czochralski method and determination of a Curie temperature of $\sim$1014 K measured by both the electrical

resistivity and dilatometry measurement.

Studies of a Ni_2MnSi Heusler system reveal two new systems i.e., the $Ni_{16}Mn_6Si_7$ G-phase and the $Mn(Ni_{0.6}Si_{0.4})_2$ based Laves phase with complex crystal structures. These systems exhibit strong magneto-structural coupling that could lead to interesting physical behaviors. The lack of thorough understanding of the properties of these materials inspired us to undertake the present studies.

We address the geometrically frustrated two-dimensional magnetic structure and spin canted weak ferromagnetic behavior of $Ni_{16}Mn_6Si_7$. Our magnetization and specific heat measurements on a Czochralski grown single crystal sample depicts the paramagnetic to antiferromagnetic transition at 197 K, and a second phase change at 50 K. Furthermore, a gradual drop of zero field cooled magnetic susceptibility is observed below 6 K that is associated with the spin freezing effect. The neutron diffraction on the polycrystalline powder samples at the temperatures of interest reveals that the antiferromagnetism is governed by the magnetic ordering of the Mn ions in the octahedral network. Below the Néel temperature of 197 K, the 2/3 of Mn atom moments form a two-dimensional magnetic arrangement, while the 1/3 moments remain geometrically frustrated. The phase transition at 50 K is found to be associated with the reorientation of the 2D moments to a canted antiferromagnetic state and development of ordering of the frustrated paramagnetic ions. Magnetization measurements as a function of temperature and magnetic field in principal directions, permit to determine the anisotropic magnetic behavior of $Ni_{16}Mn_6Si_7$ in terms of the magnetic structure obtained by the neutron diffraction measurements. We also report an irreversible smeared spin-flop type transition for the system at a higher magnetic field.

The diffuse scattering due to the short-range ordering is a commonly occurring phenomenon in Laves phase materials. The occurrence of such distinct atomic arrangement

can considerably influence the physical behavior of the material. Nevertheless, no structural reconstruction of such atomic distribution in Laves phase has ever been reported in the literature. In this work, we present the structural ordering, and the associated physical behavior of an antiferromagnetic Ni-Mn-Si Laves phase with a composition $Mn(Ni_{0.6}Si_{0.4})_2$. The possibility of unique short-range ordering in the material is first concluded based on our single crystal diffraction analysis. With the high-resolution transmission electron microscopy and electron energy loss spectroscopy analysis, our work resolves the distinct atomic ordering of the Laves phase system. The investigations reveal the origin of the short-range ordering to arise from a unique arrangement between Ni and Si. The study also presents the atomic resolution mapping of the Si atoms which has never been reported by any previous studies. With further electrical conductivity measurement, we find one of the consequences of the unique ordering reflected in a semiconducting like temperature dependence of the compound. The neutron diffraction at 298 K suggests $Mn(Ni_{0.6}Si_{0.4})_2$ to be a strong antiferromagnetic system, which is further supported by the successive magnetic susceptibility measurement. The Néel temperature is determined to be 550 K.

We also address the stability of the hypothetical ferromagnetic Heusler compound Ni_2MnSi which has been proposed to be a stable system by numerous theoretical studies. Our first-principles work corroborates those studies with a negative formation enthalpy of -1.46 eV/f.u.. However, after numerous attempts to synthesize the composition, we conclude that a single phase Heusler Ni_2MnSi compound can not form under ambient conditions. Our results show that the system crystallizes as a mixture of the two Ni-Mn-Si compounds, i.e., the $Ni_{16}Mn_6Si_7$ type G-phase and $Mn(Ni_{0.6}Si_{0.4})_2$ based Laves phase. Our work provides a possible explanation for the unstable Ni_2MnSi Heusler compound with the calculation of formation enthalpy of the hypothetical Heusler system in terms of

the computed energies of the neighboring phases $Ni_{16}Mn_6Si_7$ and $Mn(Ni_{0.6}Si_{0.4})_2$.

Acknowledgements

I would first like to thank Dr. Marek Niewczas for his support and guidance throughout my Ph.D. study. The values he imparted to me during my work under his supervision are of highest quality. I would also like to express my gratitude to Dr. John Greedan who introduced me a to several fundamentals magnetic phenomena and guided to refine the magnetic structures of materials. This work would never have been completed successfully without his input.

I would also like to thank my committee members, Dr. Yurij Mozharivskyj and Dr. Adrian Kitai for valuable suggestions during the meetings which helped me a lot to plan my research for every upcoming year.

A special thanks from must go to Dr. Oleg Rubel for giving me access to his computational facilities and sharing his research experience with me that helped me a lot finish the work successfully.

I must also thank Dr. Anton Dabkowski for training me and giving me uninterrupted access to his crystal growth facility.

Due to the work requiring the use of several different facilities, I have the pleasure of working with some fantastic and kind-hearted people. Without their assistance, this work would never have finished successfully. I would like to express my deepest appreciation towards them. Dr. Jim Britten and Victoria Jarvis trained me and guided me a lot to perform

the X-ray diffraction experiment. The Neutron diffraction experiment data collection was done with assistance from Dr. Zin Tun and Chad Boyer. Jim Garret and Fang Yuan helped me a lot with their expertise during polycrystalline sample synthesis. Paul Dube was of great assistance to be with valuable discussions and training me to use the SQUID system. Dr. Andy Duft helped cutting and preparation of the samples. Also, special thanks must be given to Dr. Andreas Korinek for assisting with the HRTEM and EELS data collection.

Finally, I would like to thank all the members of my family especially my mother and my wife Jerin Lubna for being so understanding and putting my Ph.D. work as more priority than other life goals.

Preface

Chapter 1 of the dissertation familiarizes the reader to the Heusler compound, ternary G phase and the Laves phase that have been studied during this work. The description of each compound is arranged in the following manner. First, the basic crystal structure of the compound is discussed. Then, a brief introduction to the major phenomena that will be addressed in this work is presented.

Chapter 2 the chapter introduces the compounds that were studied during this work.

Chapter 3 discusses the research objectives of the dissertation.

Chapter 4 introduces several experimental techniques and apparatus that have been used in this work for structural and physical properties characterization of different materials. The chapter also includes a short description of the first-principles density functional theory method used in ab-initio studies of the structure and properties of the compounds.

Chapter 5 contains our results and discussion of the structural and physical properties of the half-metallic Co_2MnSi system, Ni-Mn-Si based ternary G phase $Ni_{16}Mn_6Si_7$, Ni-Mn-Si based ternary Laves phase $Mn(Ni_{0.6}Si_{0.4})_2$ and the multiphase Ni_2MnSi system.

Chapter 6 provides a summary of the works performed during this study.

Contents

List of Figures

List of Tables

Chapter 1

Introduction

The geometry of the crystal structure and the associated strong nearest neighbor interactions in compounds containing transition metal ions gives rise to complex yet interesting phenomenon like geometric frustration, noncollinear magnetism and in several cases, a coupling of both [3–10]. Such materials exhibit physical properties like canted antiferromagnetic state [11–14], non collinear ferrimagnetism [15], metamagnetism [16], giant magnetostriction [17, 18], unusual magnetic hysteresis [19], giant magnetoresistance [20] and so on. These enhanced magnetic interactions are considered to be an essential requirement for applications related to quantum computation, data storage, magnetic refrigeration, and spintronics [21–25]. Current work is focused on synthesizing and characterizing physical properties of such compounds that crystallize in novel structures.

1.1 Heusler alloys

Heusler compounds are named after F. Heusler who discovered unusual ferromagnetic behavior in Cu_2MnAl [26–28] which was of particular scientific interest as none of the

constituent elements (Cu, Mn, and Al) are of ferromagnetic in nature. Compounds in this group usually offer pronounced scalability of desired electronic structure which can be achieved merely by varying the constituent elements. Such modification induces various unusual phenomenon such as half-metallic ferromagnetism [29], shape memory transition [30], non-magnetic semiconducting behaviour [31], magnetocaloric effect [30], which make them potential candidates for broad range of applications such as solar cells, spintronics, thermoelectric devices and many others [32, 33] within this crystal class.

1.1.1 Crystal structure of Heusler compounds

The Heusler compounds exist mainly in two different configurations which are determined by the number of the constituent elements. The first type is the $C1_b$ type ternary compound which is also known as the "half-Heusler" compound. The second class is called the $L2_1$ type "full-Heusler" compound.

$C1_b$

The XYZ type $C1_b$ structure crystallizes in the cubic space group 216 $F\overline{4}3m$. Here, the X, Y, and Z atoms are located on the Wyckoff positions 4c (3/4, 1/4, 1/4), 4b (1/2, 0, 0) and 4a (0, 0, 0), respectively. The crystal system can be interpreted as a combination of rock-salt (NaCl) configuration formed by the Y and Z atoms and a zinc-blend type structure formed by the X and Z elements which are illustrated in Fig. 1.1. Since a rock-salt type structure can only be formed by an ionic bond with elements having largest electronegativity differences; Y and Z in the $C1_b$ structure usually have the largest electronegativity difference.

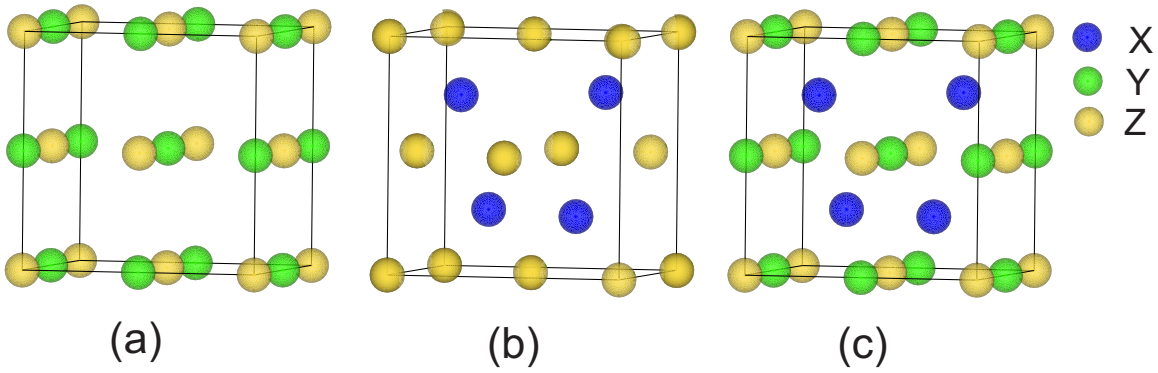

Figure 1.1: Crystal structure of $C1_b$ Heusler alloys. (a) A rock-salt structure is formed by Y and Z. (b) Zinc-blend is formed between X and Z elements. (c) Combination of both rock-salt and zinc-blend leads to a XYZ type half-Heusler compound.

In these compounds, the electropositive Y transfers the valence electrons to the electronegative X and Z. A semiconducting behavior is observed when the system contains 18 valence electrons. In such scenario, Y empties its valence orbital by transferring electrons to the electronegative Y and Z elements that undergo the stable closed shell configurations d^{10} and s^2p^6, respectively. Changing the number of valence electrons, $N_v \neq 18$ leads to a metallic and magnetic compound. A $C1_b$ type structure can hold one magnetic atom (Y) only in the fcc sublattices (Fig. 1.2) [28]. Consequently, most XYZ compounds containing two magnetic atoms crystallize in a different structure than $C1_b$ that can facilitate two magnetic atomic sites [34–36]. Nevertheless, compounds such as MnNiSb, MnPdSb and MnPtSb crystallize in the $C1_b$ structure despite containing two magnetic elements as they assume a stable configuration of $Mn^{3+}(d^4)$, $Ni/Pd/Pt^0$ (d^{10}) and Sb^{3-} (s^2p^6) [31, 37].

$L2_1$

The X_2YZ type structure falls within the space group 225 $Fm\overline{3}m$. Here, the X, Y, and Z atoms occupy the Wyckoff positions 8c ((3/4, 1/4, 1/4), 4a (0,0,0) and 4b (1/2, 1/2, 1/2),

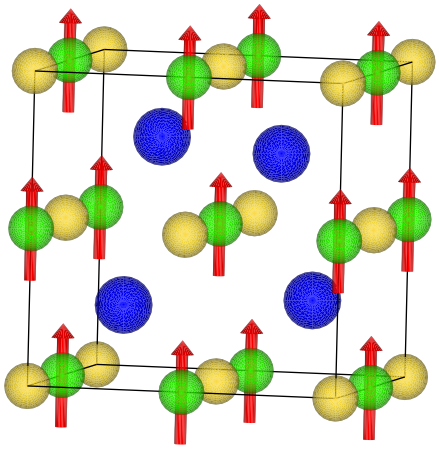

Figure 1.2: Magnetic structure of the $C1_b$ half-Heusler compound which shows that it can hold only one magnetic atom (Y) in the fcc sublattices.

respectively. Similar to the $C1_b$, the $L2_1$ structural group is also formed by a combination Y and Z rock-salt and the zinc-blend of X and Z atoms. Furthermore, the tetrahedral holes that are empty in the $C1_b$ structure are filled by an additional X atom to form a X_2YZ type system (Fig. 1.3). In the $L2_1$ full-Heusler compound, the valence electron number, N_v=24

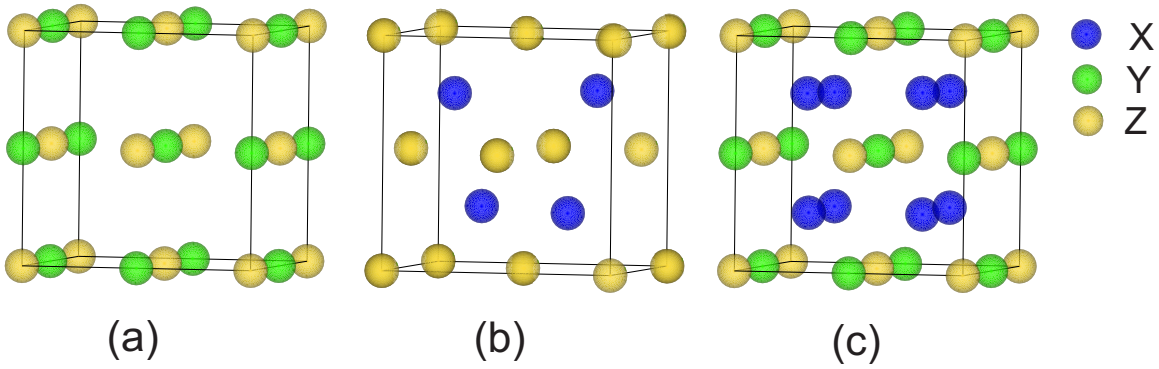

Figure 1.3: Crystal structure of $L2_1$ Heusler alloys. (a) A rock-salt structure is formed by Y and Z. (b) Zinc-blend is formed between X and Z elements. (c) A rock-salt and zinc-blend combination with the tetrahedral holes filled by X atoms leading to the X_2YZ type full-Heusler compound.

results in a stable semiconducting configuration. The structure can hold two magnetic

atoms (Fig. 1.4). As a result, changing $N_v \neq 24$ allows engineering of magnetic compounds with exceptional properties one of which was focused in this work.

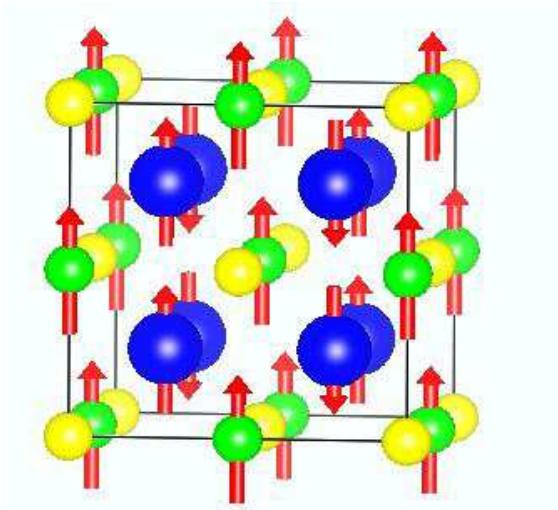

Figure 1.4: Full-Heusler compound can hold two magnetic atoms (X and Y) in the crystalline unit cell.

1.1.2 Fundamental phenomena associated with the Heusler compounds

Classification of magnetic materials

Based on the response of a material to the external applied field, magnetism can be classified into three different categories, i.e., diamagnetism, paramagnetism and collective magnetism. The collective magnetism class covers the fundamental exchange interaction based phenomena such as ferromagnetism, antiferromagnetism and ferrimagnetism.

Diamagnetism is a very weak phenomenon where magnetic moments orients in a direction opposite to the applied magnetic field (a negative magnetization). It originates from contributions of atoms that posses no net magnetic moment. The diamagnetic susceptibility, χ is negative and temperature independent (Fig. 1.5a). Nearly every material possesses

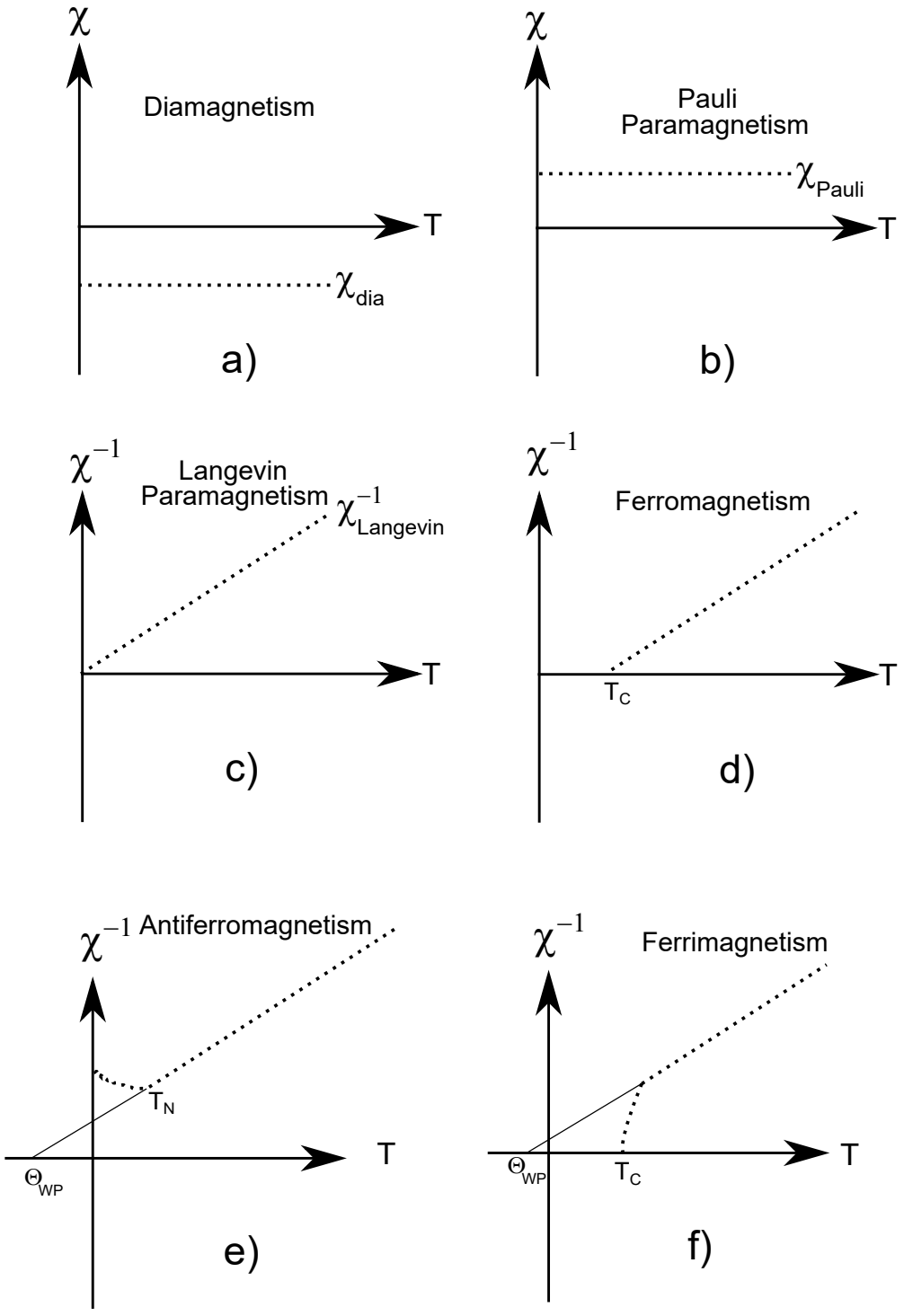

Figure 1.5: Temperature dependent magnetic susceptibility, χ variation of a) diamagnetic, b) Pauli paramagnetic materials and inverse magnetic susceptibility, χ^{-1} variation of c) Langevin paramagnetic, d) ferromagnetic, e) antiferromagnetic and f) ferrimagnetic materials.

a certain diamagnetic contribution.

Paramagnetic materials are characterized by the presence of permanent magnetic dipoles that under an external magnetic field orient in the direction of the field. Paramagnetic materials can be further categorized into Pauli and Langevin paramagnet. The positive Pauli paramagnetic response is caused by the itinerant moments and the magnetic susceptibility is temperature independent (Fig. 1.5b). Langevin paramagnetism originates from the localized moment due to partially filled inner shell. The Langevin magnetic susceptibility is dependent on the temperature (Fig. 1.5c) and can be expressed by the Curie law as,

$$\chi(T) = \frac{C}{T} \tag{1.1}$$

where, C is the Curie constant.

Different types **collective** magnetic phenomena occur depending on the nature of exchange interactions between permanent magnetic dipoles that leads to a net spontaneous magnetic moment in the material. The three most fundamental behaviors as a consequence of these interactions are ferromagnetism, antiferromagnetism and ferrimagnetism, which in the paramagnetic region are described by the Curie-Weiss law,

$$\chi(T) = \frac{C}{T - \Theta_{WP}} \tag{1.2}$$

where, C is the Curie constant and Θ_{WP} is the Weiss constant.

Ferromagnetism is characterized by the parallel alignment of the magnetic sublattices due to positive exchange interaction (Fig 1.6a). Such ordering persists until a critical temperature called the Curie point, T_C is reached above which the material behave as a

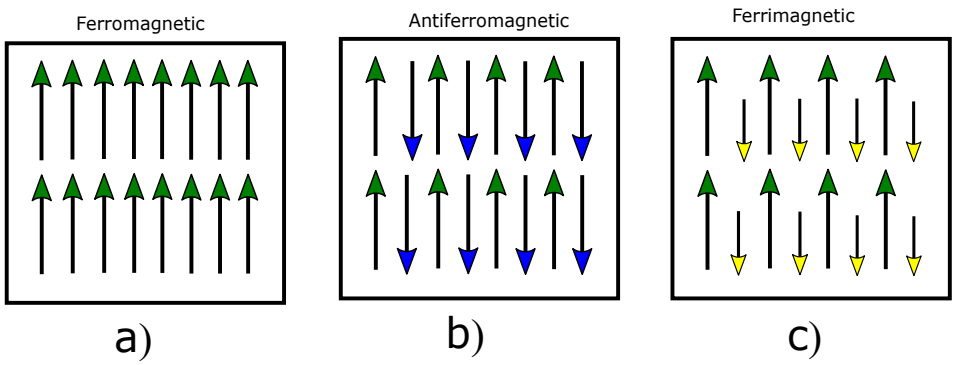

Figure 1.6: Alignment of magnetic moments for a) ferromagnetic, b) antiferromagnetic and c) ferrimagnetic materials.

paramagnetic. A typical ferromagnetic Curie-Weiss behavior in terms of inverse susceptibility, χ^{-1} vs. temperature plot is shown in Fig. 1.5d. The Weiss constant, Θ_{WP} of a ferromagnetic material is usually (but not necessarily) equal to the Curie temperatures, T_C.

In **antiferromagnetic** materials, magnetic sublattices of identical moments are oriented antiparallel to each other due to a negative exchange interaction (Fig 1.6b). Antiferromagnetic material also undergoes a phase transition to a paramagnetic system above the Néel temperature, T_N (Fig. 1.5e). The antiferromagnetic Weiss constant is negative and are usually of same magnitude of the Néel temperature (exception occurs in case phenomenon such as geometric frustration).

In **ferrimagnetism**, the magnetic sublattices of imbalanced moments are oriented antiparallel to each other (Fig 1.6b). As a consequence, the material possesses a net spontaneous moment. A typical Curie-Weiss plot for ferrimagnetic material is shown in Fig. 1.5f. Unlike for ferromagnetic material where the χ^{-1} changes linearly as a function of temperature near the phase transition, the ferrimagnetic χ^{-1} demonstrate a hyperbolic temperature dependence near the phase transition. The ferrimagnetic Weiss constant, Θ_{WP} can be either

positive or negative depending on the type of interaction between sublattices.

Slater-Pauling rule

The Slater-Pauling rule [38, 39] is an electron counting principle that provides useful guidance to predict the electronic and magnetic properties of materials before synthesizing. For Heusler compound, the method can predict the net ferromagnetic moment from the difference between the majority and minority spin valence electrons. For the $C1_b$ type half-Heusler compound, it is expressed as,

$$M = N_v - 18 \ (\mu_B/f.u.) \tag{1.3}$$

where, M is the net magnetic moment per formula unit (f.u.). N_v is the total number of valence electrons. The number 18 stands for the total number of valence electrons that do not contribute to the net magnetic moment. It is deduced by considering the average number of minority spin valence electrons per atom (9/3=3) that pair with the majority spin electrons. For $C1_b$, there are 3 atoms per unit cell leading 3×2×3=18 paired electrons.

Similarly, the Slater-Pauling rule for $L2_1$ type full-Heusler alloy is expressed as,

$$M = N_v - 24 \ (\mu_B/f.u.) \tag{1.4}$$

where, there are 24 valence electrons (4 atoms per unit cell and average number of minority spin valence electrons per atom is 12/4=3 leading to 4×2×3=24 paired electrons) who are paired up and do not contribute any magnetic moment. Figure 1.7 shows the Slater-Pauling curve for Co based full-Heusler compounds which shows that the net magnetic moment calculated based on the Slater-Pauling rules are usually in good agreement with

the experimentally observed results.

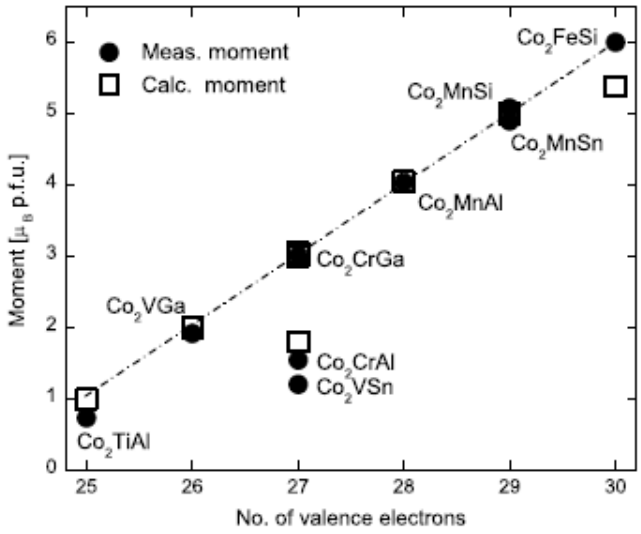

Figure 1.7: Slater-Pauling graph for Co based full-Heusler compounds [1]. The curve compares the Slater-Pauling rule based magnetic moments to the experimentally obtained values.

Another alternative parameter that is often used to address the Slater-Pauling rule is called the electron to atom ratio, (e/a). For the X_2YZ type Heusler compound, the quantity is determined in terms of number of valence electrons per atom as,

$$e/a = \frac{(2 \times n_X)(n_Y)(n_Z)}{4} \tag{1.5}$$

where, n_X, n_Y and n_Z are the number of valence electrons for X, Y and, Z, respectively. The factor of 2 in the numerator is to consider the two X atoms, and the number 4 in the denominator represents the total number of atoms in the full-Heusler compound.

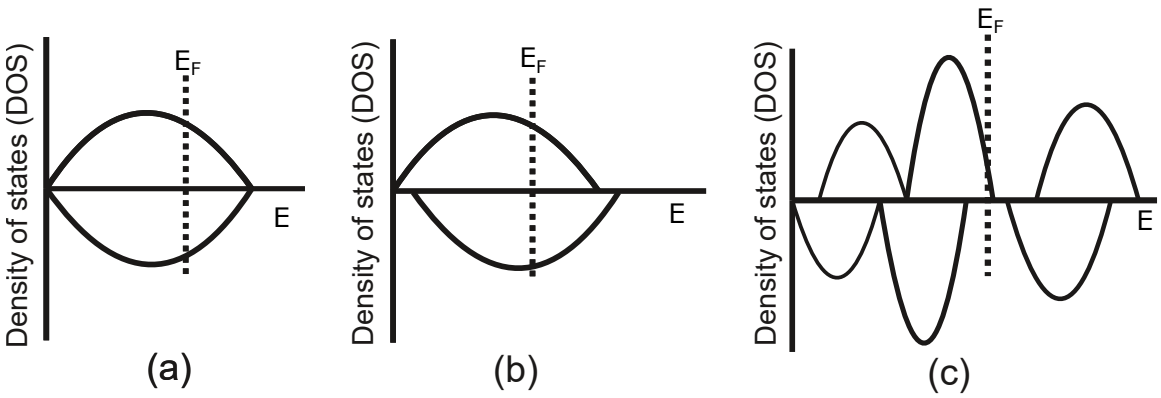

Figure 1.8: Energy as a function of density of states (DOS) for (a) paramagnetic material with no net spin polarization (b) ferromagnetic material with spin polarization less that 100% (c) Half-metal with 100% spin polarization

Half-metallic ferromagnetism

The discovery of the giant magnetoresistance in imbalanced spin states compounds [40, 41] has led to tremendous scientific quest in search of new spin-polarized materials which has ultimately revolutionized the field of spintronics [33]. The electronic spin polarization of a material is defined as the ratio of the density of states (DOS) of the majority and minority spin electrons,

$$P = \frac{DOS\uparrow - DOS\downarrow}{DOS\uparrow + DOS\downarrow} \tag{1.6}$$

where, $DOS\uparrow$ and $DOS\downarrow$ are the density of states at E_F for majority and minority spins, respectively.

Paramagnetic materials have an equal but opposite DOS value for majority and minority spin electrons (Fig 1.8(a)). Consequently, they have zero spin polarization. Ferromagnetic materials on the other hand, exhibit a difference in the DOS at E_F for opposite spin electron (Fig 1.8(b)). As a result, they have a finite spin polarization that implies the presence

of a net magnetization. In the ideal scenario for spintronic devices, the material will exhibit a metallic behavior for one spin state and semiconducting nature in the other which is termed as the half-metallic behavior. In this phenomenon, a material attains the 100% spin polarization (P=100%) at the Fermi level (E_F). In such condition, a material has one spin channel with zero DOS value while the other spin channel has a finite value. A typical DOS curve for a half-metal is shown as a function of energy in figure 1.8(c). In contrast to ferromagnetic materials, half-metallic materials have the DOS of an insulator or semiconductor in one spin channel and that of metal in another. Therefore, these materials can be regarded as a hybrid of metals and semiconductors. The presence of a 100% spin polarization promises a 100% spin injection which can increase the efficiency of magnetoelectric devices.

The phenomenon was first predicted in the half-Heusler NiMnSb compound by De Groot et al. [42] which attracted a lot of interest. A subsequent theoretical study by Kübler et al. [43] demonstrated the same phenomenon for full-Heusler Co_2MnSn. A growing interest since then led to several compounds in the Heusler group to be predicted as half-metallic ferromagnet [44–49]. From the experimental view, such a 100% spin-polarized state can only be attained under a vanishing spin-orbit coupling and at zero temperature conditions. The transition metal based Heusler compounds offer large scalability of electronic properties and negligible spin-orbit coupling effects [33, 50–59] and are therefore, a widely investigated class of materials for spintronic applications. Also, Heusler alloys usually exhibit high Curie temperatures that facilitate their operation at ambient temperatures [33].

Despite the tremendous theoretical effort, a 100% spin polarization has not yet been observed experimentally in any Heusler compounds. The discrepancy between theoretical

predictions and experimental results has mainly been attributed to the presence of structural disorder and the finite temperature effects. The transition metal elements in these compounds tend to swap sites with each other which introduces new states in the minority spin gap and destroys half-metallicity. Another cause for the destruction of the 100% spin polarization is thought to be the spin disorders that appears at finite temperatures [60–63].

1.1.3 Structural stability of Heusler compound

A full-Heusler compound X_2YZ is formed by the following chemical reaction,

$$2\,X + Y + Z \longrightarrow X_2YZ \tag{1.7}$$

The formation enthalpy of the compound can then be computed using the expression,

$$\Delta H = E_{tot}(X_2YZ) - 2E_{tot}(X_{bulk}) - E_{tot}(Y_{bulk}) - E_{tot}(Z_{bulk}) \tag{1.8}$$

where, $E_{tot}(X_2YZ)$ is total energy per formula unit (f.u.) of X_2YZ type structure. $E_{tot}(X)$, $E_{tot}(Y)$ and $E_{tot}(Z)$ are the total energy of X, Y and Z per f.u., respectively in their bulk form. These energies can be easily obtained from a first-principles study, and thus, the stability of the Heusler compound can be predicted by the formation enthalpy using Eq 1.8. A negative energy indicates that the reaction in equation 1.7 will go in the forward direction and the structure is stable in the X_2YZ state.

Table 1.1 lists formation enthalpy values of some selected Heusler compounds that have been computed in the present work. The energies for different systems were computed using the first-principles method implemented in WIEN2k [64].

Table 1.1: Formation enthalpy parameters of several Heusler compounds calculated using the first-principles method

Compound	Formation enthalpy (eV/f.u.)
Ni_2MnGa	-2.08
Co_2MnSi	-2.39
Co_2FeSi	-1.65
Ni_2MnSi	-1.46

1.2 G phase

The G phase system was discovered by Beattie and VerSnyder [65] in 1956. The system crystallizes in a complex crystal structure with at least one the constituting elements being a transition metal or rare earth ion [65–68]. Since, such combination of structure and elements are usually thought to be promising candidate for applications related to magnetic suppression and superconductivity, the system was the focus of several theoretical and experimental interests [66–71]. However, no such behavior has yet been observed in these materials. Nevertheless, a complex crystal structure containing transition metal and rare earth elements holds promises for unique magnetic coupling in these compounds.

1.2.1 Crystal structure of G phase compounds

The ternary $X_{16}Y_6Z_7$ type G phase crystallizes in a $Cu_{16}Mg_6Si_7$ type structure (also known as $Mn_{23}Th_6$ type) in the $Fm\bar{3}m$ spacegroup. The asymmetric unit contains five atoms where the X atoms occupy two 32f positions; the Y atoms sit at the 24e and the Z atoms in 4a and 24d Wyckoff site making a total of 116 atoms in the unit cell (Fig 1.9 (d)). The structure can be simplified in terms of two interpenetrating tetrahedra formed by the X elements(Fig 1.9 (a)), an octahedron formed by the 24e Y and another octahedron formed by the 24d Z(Fig 1.9 (c)). The Y octahedra are arranged in a NaCl like pattern with the 4a

Z atoms(Fig 1.9 (b)).

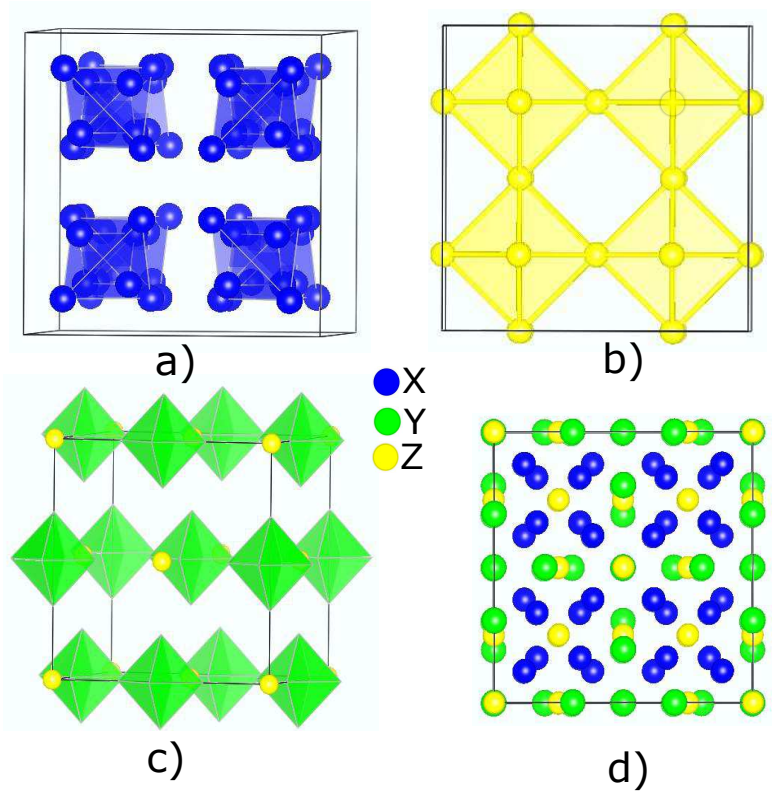

Figure 1.9: Crystal structure formation of a $X_{16}Y_6Z_7$ type ternary G Phase. a) Two interpenetrating tetrahedra by X, b) octahedra of Z, c) NaCl type formation of 4a Z and Y octahedra, and d) a complete crystal structure of $X_{16}Y_6Z_7$.

1.2.2 Fundamental phenomena associated with the ternary G phase

Geometric frustration

Magnetic frustration is a phenomenon in which competing or contradictory constraints act on identical magnetic sites of a material. It was first observed by Anderson [72] while studying the magnetic ordering of ferrites. Later a firm basis on the phenomenon was provided by Toulouse [73]. When magnetic frustration occurs due to a geometric constraint,

it is defined as the geometric frustration. A simplistic explanation of such lattice constraint can be given with a triangular ”plaquette” involving three nearest neighboring spins connected by the exchange constant, J in antiferromagnetic configuration [5]. The Hamiltonian for interaction between any two of these neighboring spins can be written as,

$$H_{ex} = -2J\,\mathbf{S_1}.\mathbf{S_2} \tag{1.9}$$

The negative sign in equation 1.9 accounts for the antiferromagnetic interaction. It is evident from figure 1.10 that only any two of the three spin configurations can be satisfied simultaneously and the system is described to be geometrically frustrated. The phenomenon can also appear due to a three-dimensional constraint in the system. The present work addresses a compound with the frustration of Mn atoms in the octahedral arrangement.

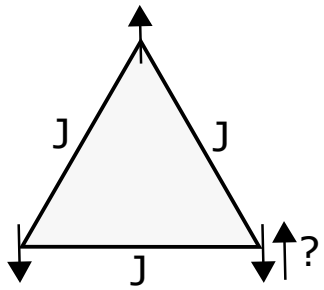

Figure 1.10: Equilateral triangle explaining geometric frustration.

Since, geometric frustration occurs due to the symmetry of lattice, breaking of crystalline symmetry or antisymmetric exchange constant can often relieve the frustration of magnetic lattices.

Canted antiferromagnetism

The appearance of a weak ferromagnetism due to spin canting in antiferromagnetic materials was first realized in α Fe_2O_3 by Dzyaloshinsky [74]. Later a firm theoretical basis was provided by Moriya [75]. In this phenomenon of Canted antiferromagnetism, a non-collinear arrangement of spins with respect to the axis in two different magnetic sublattices gives rise to net ferromagnetic moment for the system (Fig 1.11). Such a phenomenon usually occurs from two different sources of anisotropic coupling (single-ion anisotropy and anisotropic spin coupling). The former one arises when the single-ion anisotropy energies of the magnetic sublattices are different which makes the easy directions for the spins at those positions to be anisotropic. As a result, canting of magnetization at those sublattices takes place. Another mechanism for canting occurs due to an antisymmetric superexchange interaction of spins which is also known as Dzyaloshinsky-Moriya (DM) interaction. Such anisotropic spin-spin coupling is heavily influenced by the crystal symmetry, and is only present in the absence of a center of inversion between magnetic sites.

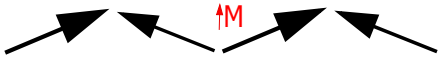

Figure 1.11: Canted antiferromagnetism: Non collinear arrangement of spins resulting a net magnetic moment.

1.3 Laves phase

Laves phase (also known as Friauf-Laves phases) is the result of separate investigations of Friauf and Laves on the crystal structure of $MgCu_2$, $MgZn_2$ and $MgNi_2$ [76–78]. With more than 1400 reports of stable binary and ternary compound, Laves phase contains the largest group of the intermetallic family [79]. This largest group of material demonstrate

a wide variety of physical properties since a stable Laves phase is formed with most of the elements that are present on the periodic table. Some of the novel properties of these materials include high strength, corrosion resistance, high temperature stability, itinerant magnetism, metamagnetism, magnetocaloric effect and many others [79–83].

1.3.1 Crystal structure of Laves phase compounds

Laves phase are found in three different polytypes that comprise one cubic and two hexagonal type structures. The first type is the C15 type cubic $MgCu_2$. The second and third class contain hexagonal structures of the C14 type $MgZn_2$ and C36 type $MgNi_2$.

C15 type $MgCu_2$

Materials in the C15 type structure crystallizes in a XY_2 cubic face centered structure in the $Fd\bar{3}m$ space group with eight formula units. The asymmetric unit contains two different type of atoms. The X atoms with largest atomic radius occupy the 8a site, and the Y atoms are located in the 16c site. A $MgCu_2$ type crystal structure is shown in figure 1.12(a).

C14 type $MgZn_2$

In a XY_2 type structure, the material crystallizes in the hexagonal $P63/mmc$ group with four formula units. In the asymmetric unit, the largest atomic radius atoms X sit in the 4f position while the atoms Y occupy the 2a and 6h positions (Fig 1.12(b)).

C36 type $MgNi_2$

The C36 type XY_2 crystal is also found in the hexagonal $P63/mmc$ group with eight formula units. The asymmetric unit contains five different sites with X taking the 4f and 4e

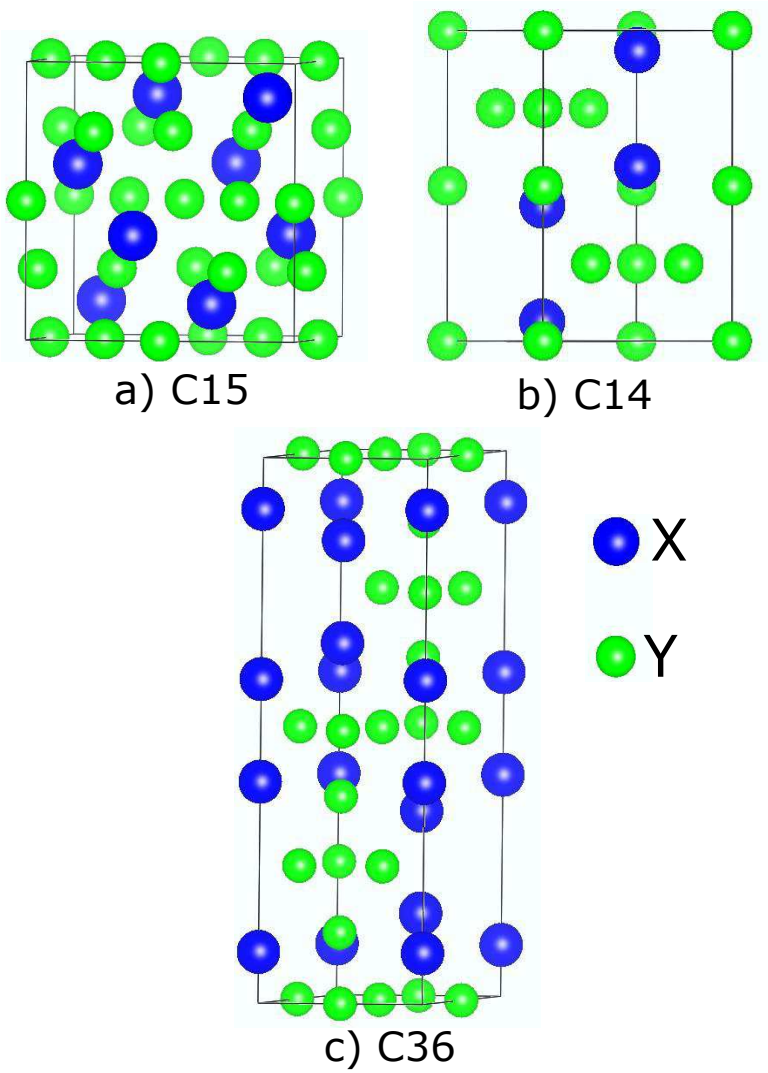

Figure 1.12: Crystal structure of XY_2 type Laves phase in a) $MgCu_2$ type C15 , b) $MgZn_2$ type C14 and c) $MgNi_2$ type C36 structure.

and the Y taking the 6h, 6g and 4f positions (Fig 1.12(c)).

1.3.2 Ternary Laves phase

The ternary Laves phase system can be divided mainly into several different categories [84]. In the first type, a binary Laves phase, XY_2 in the C14, C15 or C36 type structure dissolve a certain amount of a third element forming a $X(YZ)_2$ or $(XZ)_1(Y)_2$ type system that has the same structure as the parent phase. Some examples of these systems are the C15 type $Nb(Cr_{1-x}V_x)_2$ [85], the C15 type $(Nb_{1-x}Ti_x)Cr_2$ [85] and the C14 type $Ti(Fe_{1-x}Al_x)_2$ [86].

In another type, the addition of the third element in a particular binary Laves phase crystalizes the system in a different polytype. One such example is the Cu-Al-Mg system where addiction of 20% of Al in the C15 type $MgCu_2$ stabilizes the system in a C14 type configuration [87].

Another type of ternary system is formed when two binary Laves phase materials are mixed together which then stabilizes the ternary system into a different polytype. An example is the mixing of $NbCr_2$ and $NbCo_2$ which are both C15 type. The resultant $Nb(Co_{1-x}Cr_x)_2$ compound is found to be stabilizing in a C14 type structure [88].

The last type of ternary system forms when the addition of the third element in a non-Laves binary phase stabilizes a C14 type Laves phase structure. A ternary C15 or C36 type structure in this group has not yet been reported. Nevertheless, these C14 type ternary Laves phases can undergo a structural transformation to the C15, or C36 type under the influence of external perturbations such as temperature or pressure. Some examples of these materials are Ni-Ti-Zr [89], Ni-Ta-Al [90], Cu-Ti-Zr [91], Cu-Mn-Si [83] type Laves phase. The Ni-Mn-Si type that will be discussed in the present work falls into this family of C14 Laves phase system and will be focused in preceding sections.

1.3.3 Site occupancy in C14 type ternary Laves phase

In a XY_2 type binary Laves phase, most stable system is found at the ideal atomic size ratio, $\frac{r_X}{r_Y} \approx 1.225$. This implies that in the C14 system the X (4f) is to be occupied by the element with the largest atomic size. If a third element, Z with an atomic size similar or close to X is added, it will most likely sit in the $4f$ position forming $(XZ)_1(Y)_2$. If the third alloying element has an atomic radius close to Y, it will occupy either the 2a or the 6h positions depending on the crystal chemistry. However, if the atomic size of X and Y are similar or the size of Z lies in between X and Y, the site occupancy becomes unpredictable [84]. Furthermore, in case of the ternary $X(YZ)_2$ formation, the concentration and atomic size of Z and Y plays an important role in determining their occupancy in 2a and 6h.

The most compelling explanation of the substitutional 2a and 6h occupancy emphasizes on the nearest neighbor or pair interaction of atoms in these sites [92]. In the C14 Laves phase, the spacing between Y (or Z) atoms is always smaller than their interatomic spacing in the bulk element which implies an attractive Y-Y (or Z-Z) interaction. The spacing between X and Y, on the other hand, are so large that formation of a X-Y bond is not feasible. Based on aforementioned, Faller and Skolnick [92] predicted that Y and Z would be distributed in 2a and 6h sites in either homonuclear (Y-Y or Z-Z) or heteronuclear (Y-Z) bonds depending on whichever configuration is energetically more favorable. In a C14 system, an atom in either 2a and 6h have 12 nearest neighbors. 6 of these are X and 6 are Y (or Z). In case of an atom in 2a, all 6 of the identical nearest neighbor atoms are located in 6h. For an atom in 6a, 4 of the nearest neighbors are located in 6a, and 2 of them are in 2a. For example if a system favors Y-Z type or heteronuclear bonds and a small concentration of Z is added, then Z will preferentially occupy the 2a site as that will maximize the Y-Z connections. There is not a complete theory that can clearly identify

whether a homonuclear or heteronuclear bond will be formed. One of the explanations which often successful is made in terms of the electronegativity difference between Y and Z. If the difference is small, charge transfer is unlikely, and homonuclear bond will be more favorable. When the electronegativity difference is large, then charge transfer will take place, and heteronuclear bonds will be formed.

Chapter 2

Compounds of interest and knowledge gap

2.1 Co_2MnSi

Co_2MnSi has been one of the most widely investigated systems for half-metallic ferromagnetism [50, 52, 93–104]. The interest began to develop because of their theoretically predicted 100% spin polarization [45], high Curie temperature [105, 106] and low dampening of the magnetic relaxation [107]. The material crystallizes in the $L2_1$ type of structure with a net magnetization of $5\ \mu_B/Unit\ cell$ based on the Slater-Pauling rule. A stable configuration of the system in the $L2_1$ structure is also reflected in the negative formation energy of $-2.39\ eV$ obtained from the first-principles calculation. As shown in figure 2.13, the material posses a band gap for the minority spin channels, and as a result, the spin polarization of 100% is theoretically feasible. Similar to other systems, the expected half-metallic behavior was also never observed in the experiments. The deviation from the half-metallic behavior has been mainly attributed to the presence of atomic disorder in the material [94, 95, 103].

The highest spin polarization value reported for Co_2MnSi is $93(^{+7}_{-11})$% which was measured on the bulk sample by ultraviolet-photoemission spectroscopy at room temperature [102]. For thin films, spin polarization value up to 89% was observed only at low temperatures because of the effect of the spin disorder being minimum [97]. Recently, Moges et al. [108] studied the relationship of spin disorder with the temperature in an off-stoichiometric $Co_2MnSi_{0.84}$ thin films. With a maximum applied field of 3 kOe the authors reported a transverse magnetoresistance (TMR) ratio of 1400% at 4.2 K compared to 300% at room temperature in this compound.

Despite numerous investigations on the Co_2MnSi system, there are still several open questions that arise mainly from the disagreements between experimental and theoretical results. One such discrepancy concerns the structural disorder between Co and Mn sites that is one of the cause for the loss of the half-metallicity. The site occupancy parameters for Co_2MnSi was studied by Ravel et al. [94] using the neutron diffraction and X-ray absorption fine structure (EXAFS) technique. Their study pointed towards a similar disorder affinity for both Co and Mn sites with $\sim$4-7% of the Co sites being occupied by Mn and $\sim$8-14% of the Mn sites being occupied by Co. On the contrary, a theoretical study by Picozzi et al. [99] reported the disorder affinity for Co sites to be almost twice less than the Mn sites. Although their study further pointed the disagreement with experimental observations to be related to the computational parameters, there has not been any further attempts to address this problem.

Another question that persists in the literature concerns the magnetic moment of Co_2MnSi. Previous neutron diffraction studies without any applied magnetic field reported moments in the range of 5.16-5.62 $\mu_B/f.u.$ at room temperature [94, 106] and 5.07 $\mu_B/f.u.$ at 4

K [105]. A recent theoretical study by Pradines et al. [103] and the earlier work by Picozzi et al. [99] on the other hand, suggested a reduction of the total magnetic moment in equilibrium conditions at 0 K, due to antiferromagnetic interactions induced by Mn antisite disorder. Such antiferromagnetic predictions have not yet been reflected in any experimental neutron diffraction measurements.

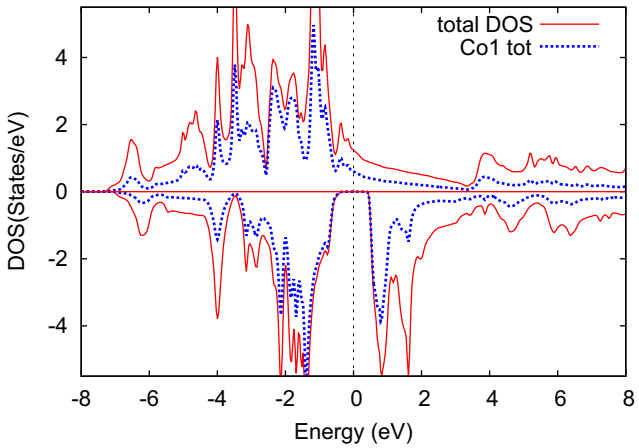

Figure 2.13: The DOS plot for Co_2MnSi as a function of energy showing a half metallic gap at the Fermi energy, E_F.

2.2 The Ni-Mn-Si based G-phase compound, $Ni_{16}Mn_6Si_7$

A complex crystal structure containing transition metal and rare earth elements holds promises for unique magnetic coupling in the ternary G-phase compounds. The Ni-Mn-Si based $Ni_{16}Mn_6Si_7$ type G-phase is one such transition metal rich compounds, which has been proposed to be an antiferromagnetic system below 200 K by Stadnik and Sklozdra [109]. Further neutron diffraction and magnetization analysis by Kolenda et al. [2] proposed a body-centered antiferromagnetic configuration of Mn^{2+} ions dominating the magnetic properties

of the compound. However, several aspects of the physical properties of the system are still unanswered. The neutron diffraction refined magnetic moment of 2.7 μ_B/Mn obtained by Kolenda et al. [2] is much lower compared to the expected value of $5\mu_B$ for $S = \frac{5}{2}$ system. Also, the magnetic susceptibility variation as a function of temperature reported is found to behave somewhat unusually from the conventional antiferromagnetic behavior of a polycrystalline system.

2.3 The Ni-Mn-Si based Laves phase

There has been a very limited number of studies on the structural and magnetic properties of Laves phase containing Ni, Mn, and Si [83, 110, 111]. Phase equilibria of the Ni-Mn-Si system suggested the phase to be stable within a wider homogeneity range of 26-30 atomic percent of Si, 31-35 atomic percent of Mn and balance Ni [112, 113]. The material falls into the category in which the addition of a third element (Si) in a non-Laves transition metal compound stabilizes a C14 type structure [80, 114–117]. Such modification has been a topic of great scientific interest as the resulting transition metal-silicon compounds demonstrate superior magnetic, electronic, thermal and mechanical properties[80–83]. The stabilization is believed to be due to a reduction of effective electron concentration by the absorption or localization of the transition metal electrons by silicon [80, 114, 118].

A comprehensive study of structural and magnetic properties on Ni-Mn-Si laves phase was performed by Yan et al. [83] where a Mn($Ni_{0.625}Si_{0.375}$)$_2$ composition was investigated. The system found to be an antiferromagnet with a Néel temperature of 630 K, and a possible magnetic configuration was proposed. The study reported the preferential site occupations of Ni and Si in 2a and 6h where the two sites were found to facilitate the atoms in unconventional proportion. As discussed in section 1.3.3, these sites are occupied in

the form of either a heteronuclear or homonuclear arrangement depending on the chemistry of system. Such a distinct atomic arrangement is expected to give rise some special atomic ordering in the system. In fact, the presence of short-range ordering in Laves phase systems is a very well known phenomenon that has been observed as diffused scattering in the diffraction intensity in many other studies [119–124]. However, to the best of our knowledge there has been no report of a structural reconstruction of such ordering.

2.4 Ni_2MnSi

Several first-principles studies have proposed the hypothetical Ni_2MnSi Heusler system to be a stable system [125–128]. Additionally, a recent machine-learning study by Oliynyk et al. [129] predicted a probability of 99% for the compound to be formed. Furthermore, our first-principles study on the compound also yielded negative formation energy of $-1.46\,eV$ which is usually an indication of a stable configuration of the system. No successful synthesis of the compound, however, is reported in the literature. The compound posses a N_v value of 31 (e/a=7.75) and consequently, is not expected to show a magnetic shape memory distortion in the stoichiometric composition. The inability to undergo any tetragonal distortion can also be confirmed by DOS curve (Fig 2.14) which shows no unstable d orbital peak in the curve.

Our initial attempt, however, could not successfully obtain a single phase Ni_2MnSi for the sample that was annealed at 800^0C for two weeks after arc-melting. Instead, a mixture of the $Ni_{16}Mn_6Si_7$ type ternary-G phase and $Mn(Ni_{0.6}Si_{0.4})_2$ based Laves phase was found in the Ni_2MnSi composition. A similar situation of instability in the Heusler compound was detected by Adem et al. [130] while synthesizing the Ni_2MnGe compound. In their study, however, a nearly pure L_{21} compound was obtained later by annealing the material

at higher temperatures.

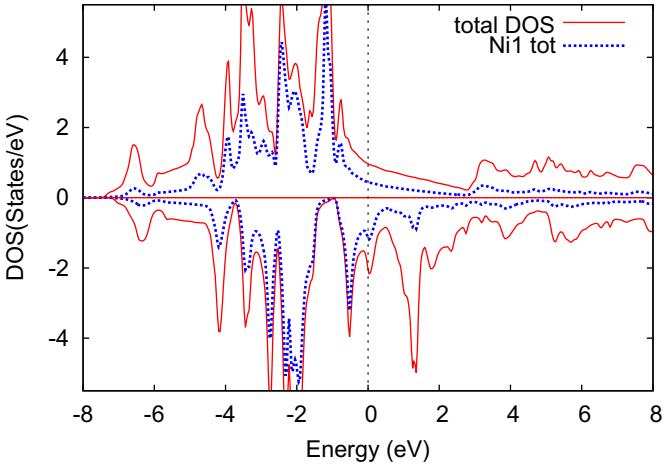

Figure 2.14: The DOS plot for Ni_2MnSi in the $L2_1$ as a function of energy.

Chapter 3

Research objectives

The objective of the research was to develop an understanding of the correlations between structure and physical properties of the transition metal based half-metallic Co_2MnSi system, Ni-Mn-Si based ternary G phase $Ni_{16}Mn_6Si_7$, Ni-Mn-Si based ternary Laves phase $Mn(Ni_{0.6}Si_{0.4})_2$ and the multiphase Ni_2MnSi system. The compounds were chosen based on the potentials of these systems to demonstrate interesting magneto-structural coupling. The work was focused on the characterization of fundamental properties of these materials that have either not been addressed or discussed adequately by previous literature. Results and conclusions from this work will help in understanding the complex behaviors of these materials and should encourage futures studies to focus on the unexplored areas by adopting a similar approach.

3.1 Co_2MnSi

In an effort to shed light on the correlation between the occupancies of disorder and the magnetic moments, we performed a combined experimental and theoretical study of the

Co_2MnSi half-metallic Heusler system. The powder neutron diffraction study of the compound was conducted at 298 K, 100 K, and 4 K to retrieve the structural and magnetic parameters. Subsequent first-principles calculations with defects were performed to validate the experimental observations and to provide a consistent explanation of the disorder occupancies and the magnetic moments. Single crystal of Co_2MnSi grown by the Czochralski method was used to characterize the physical properties with the dilatometry and electrical resistivity measurement.

3.2 The Ni-Mn-Si based G-phase compound, $Ni_{16}Mn_6Si_7$

The relationship between crystallographic structure and magnetic properties reported by previous works prompted a comprehensive investigation of the magnetostructural coupling of $Ni_{16}Mn_6Si_7$. The studies were performed on a single crystal $Ni_{16}Mn_6Si_7$ grown by the Czochralski method. The magnetic structures were obtained from the neutron diffraction experiments at 298 K, 100 K, and 4 K. The focus of the study was to develop a better understanding of the correlations between magnetic structure and the physical behaviour of the compound in a broad range of temperatures. The work addressed the geometric frustration in the system observed below the Néel temperature. The measurements also revealed a spin canted antiferromagnetic phase change at 50 K and evidence of spin-freezing below 6 K that were not reported in any previous studies.

3.3 The Ni-Mn-Si based Laves phase

The lack of a structural mapping of the preferential ordering of Laves phase encouraged us to conduct a study to determine the atomic ordering of the system and its influence

on the physical properties. The ternary Laves phase with the composition $Mn(Ni_{0.6}Si_{0.4})_2$ was chosen in this work based on the previous reports that hinted unique structural ordering of the system. The single crystal sample grown by the Czochralski method was used for structural refinement. Based on the analysis of the single crystal diffraction data, subsequent high-resolution transmission electron microscopy (HRTEM) and electron energy loss spectroscopy (EELS) analysis were performed on the (0001) oriented surface to observe the unique short-range atomic ordering of the Ni and Si atoms. Successive electrical conductivity measurements were then conducted to discuss the consequences of such atomic arrangement on the transport properties. We have also performed a neutron diffraction experiments to determine the magnetic structure, and a high temperature magnetic susceptibility measurements to depict the ordering temperature.

3.4 Ni_2MnSi

Inability to synthesize a single phase Ni_2MnSi during the initial part of the work compelled us to attempt a high temperature synthesis condition and examine the validity of the theoretical prediction of a stable compound. The as-cast sample, as well as the specimen that was annealed at higher temperatures, were studied in an attempt to obtain a single phase Ni_2MnSi. Neutron diffraction studies were performed at 298 K, 100 K, and 4 K, respectively to examine the presence of any unusual phase transitions at low temperatures. Finally, a first-principles calculation of the formation enthalpy with regard to the neighboring phases was conducted to discuss the stability of a single phase Ni_2MnSi.

All the relevant works on these compounds are presented in **Chapter 5**

Chapter 4

Experimental methods

4.1 Arc-melting synthesis

The high temperature arc-melting in an inert atmosphere is an attractive method to grow high-melting point compounds with good homogeneity. Figure 4.15a shows the photograph of the arc-melting configuration that was used for polycrystal synthesis in this work. The system consists of a power supply, and a chamber (Fig. 4.15b) where the synthesis was done. The melting chamber was sealed by a large quartz tube. During the melting, the chamber was evacuated to remove the oxygen and is filled with high purity inert argon gas. The high purity starting materials were placed on a water cooled copper hearth that acts as a cold crucible. The arc was generated using a tungsten electrode. During the synthesis, the ingot was remelted several times to improve the homogeneity of the compound. One of the challenges of the high temperature arc-melting is the loss of some starting materials due to evaporation. To overcome this issue, the melting of our compound was conducted with excess Manganese that evaporates during arc-melting. The mass of excess Mn was determined by adopting a trial and error method. To further improve the crystallinity, all

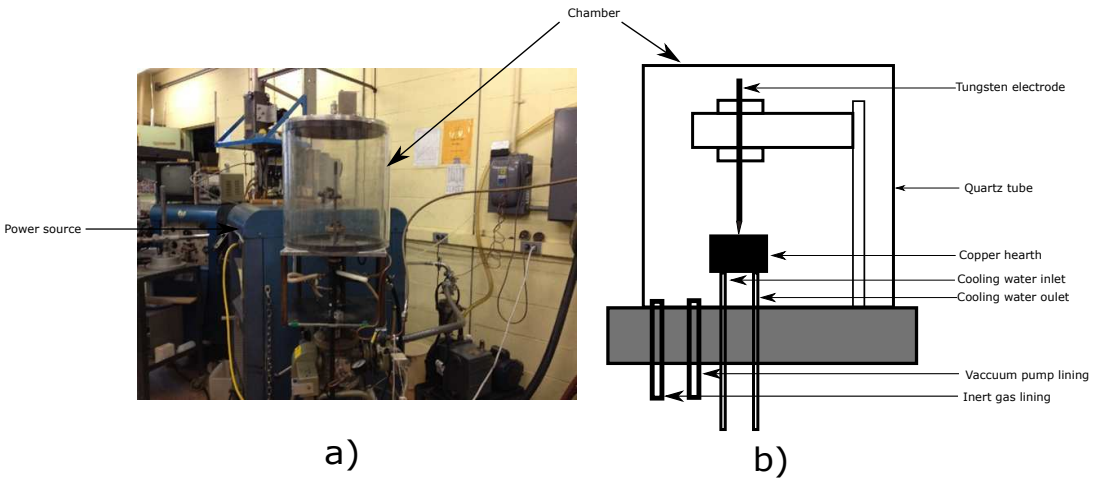

Figure 4.15: a) The arc-melting system used in this work. b) Schematic of the cross-section of the arc-melting chamber.

compounds were sealed in an evacuated silica tube, annealed at 800^0 C for two weeks and subsequently, quenched in ice water mixture.

4.2 Czochralski crystal growth

All the single crystals studied in the present work were grown using the RF heating Czochralski crystal growth furnace in an argon atmosphere. The method is a widely used to grow single crystals of complex compounds from the melt. The process was invented by Polish scientist Jan Czochralski in 1918 [131]. A cross-sectional view of the RF heated Czochralski growth chamber used in this work is shown in figure 4.16. A high-frequency induction current passed through water-cooled copper coil was used as the heating source. To protect copper coil from the high temperature of the melt, the alumina crucible was placed inside a quartz tube filled with insulating fibres. The choice of using alumina crucible was influenced by the consideration of the thermal expansion of materials being synthesized. Tungsten wire was used as seed material. The system also included a weight measuring

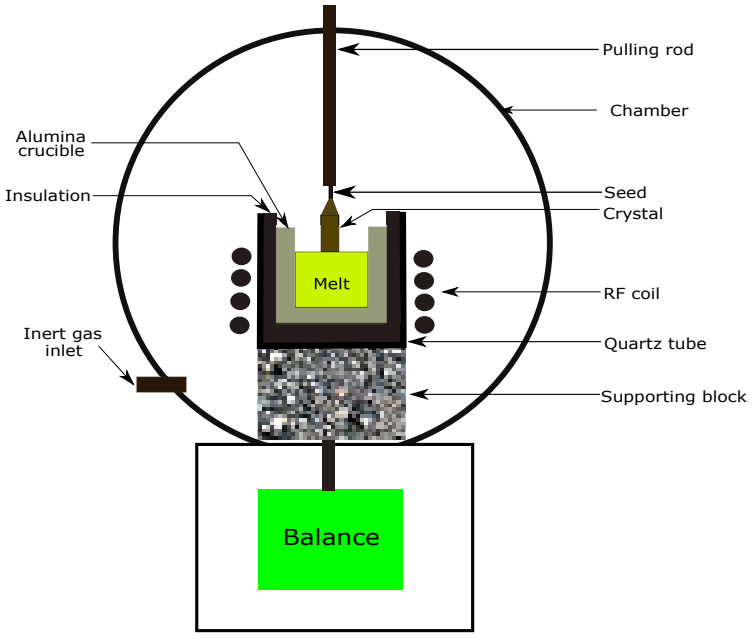

Figure 4.16: A schematics of the Czochralski growth system used in this work.

balance to measure the weight loss of the melt during the growth. The crystal growth process, including heating, seed rotation and pulling the crystal from the melt, was controlled by a computer. The operation procedure of the Czochralski crystal growth system that was maintained in this work is described as follows.

- The starting material was loaded inside the alumina crucible, and the chamber was closed.

- Inert argon was blown to the chamber for up to 24 hours at a flow rate of 15 L/hr. The longer flow of argon reduces the oxygen level in the chamber to up to 0.5% that helps to prevent oxidation of melt.

- The temperature was raised slowly by passing the high-frequency alternating current through the RF coils until the starting materials melt to form the compound. The melting of the material is observed visually as the system is not equipped with any thermometer.

- The melt was held at a constant temperature for homogenization. The high-frequency

magnetic field generated in the coils also assists the process by stirring the hot metallic samples.

- The melt temperature was slowly lowered to achieve supercooling and incipient nucleation.

- Once the system was stabilized, the rotating seed was dipped into the melt.

- When the seed was grown to the desired diameter, pulling of the incipient crystal was done at a predetermined rate that maintains the crystal size and growth.

A successful Czochralski crystal growth requires a strict control of the process parameters like the stability of the melt, interface angle between the crystal and the melt, seed rotation rate, and crystal pulling rate. These parameters are specific to the material being synthesized and are dependent on each other. An imbalance in the control of these factors leads to the failure of the whole process. A successful crystal growth thus involves a trial and error type approach to determine exact process parameters. Table 4.2 lists the parameters for the single crystal growth used in our work along the crystal growth direction found determined by the Laue diffraction.

Table 4.2: Single crystal growth parameters used in this work.

Crystal	Rotation (rpm)	Pulling rate (mm/min)	Orientation of the crystal grown)
$Ni_{16}Mn_6Si_7$	30	0.5	$< 110 >$
Co_2MnSi	30	0.5	$< 100 >$
$Mn(Ni_{0.6}Si_{0.4})_2$	30	0.5	$< 0001 >$

4.3 X-ray diffraction

Knowledge of the spatial distribution of atoms is a fundamental requirement in explaining the physical behaviors of any material. The phenomenon of diffraction by the crystalline solid is one of the techniques that facilitates such crystal mapping. In this method, the scattering of particles such as electrons, neutrons or protons by the atoms or molecules of the system is employed to construct the detailed information about the crystal or magnetic structure. X-ray diffraction is one such phenomenon that is very commonly used to map the crystal structure of materials and was used extensively in this work.

The most elementary example of diffraction by solid can be given in terms of a regular lattice of discrete atoms (Fig. 4.17). If an atom in such a system is excited by an electromagnetic wave, the resulting wave will be in phase with the incident wave and will reradiate in all direction. The amplitude of these wave in any direction can be determined by summing up contributions in that direction from each atom taking the phase difference into account. Diffraction tends to appear when there is a constructive inference between the resultant waves. The condition for diffraction maximum is given by the Bragg law [132],

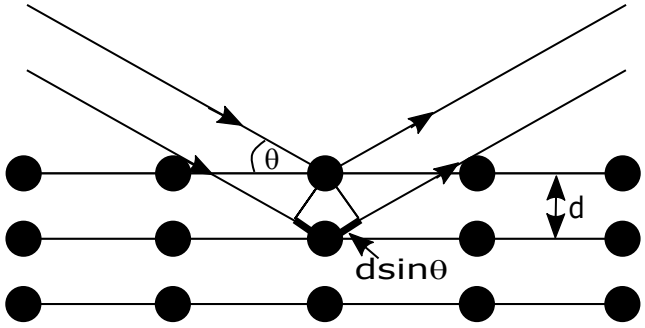

Figure 4.17: Diffraction of X-ray in a periodic lattice of discrete atoms.

$$2dsin\theta = n\lambda \tag{4.10}$$

where, d is the interplanar separation, θ is the angle of incidence, λ is the wavelength of the incident X-ray and n is the order of reflection. Diffraction maximum will occur based on the different values of n. For a given set of planes, the Bragg's law (Eq. 4.10) only predicts the geometric conditions that need to be satisfied to observed diffraction. The experimental determination of a particular structure was made possible with the incorporation of the concept of reciprocal lattice with Bragg's condition by Ewald [133]. In this method, a reciprocal space is constructed that consists of the lattice vectors, $\mathbf{a}^*$, $\mathbf{b}^*$ and $\mathbf{c}^*$ which are related to the lattice constant, $\mathbf{a}$, $\mathbf{b}$ and $\mathbf{c}$ by,

$$\mathbf{a}^* = \mathbf{2}\pi\frac{\mathbf{b}\times\mathbf{c}}{\mathbf{a}.(\mathbf{b}\times\mathbf{c})},\ \mathbf{b}^* = \mathbf{2}\pi\frac{\mathbf{a}\times\mathbf{c}}{\mathbf{b}.(\mathbf{a}\times\mathbf{c})},\ \mathbf{c}^* = \mathbf{2}\pi\frac{\mathbf{b}\times\mathbf{a}}{\mathbf{c}.(\mathbf{b}\times\mathbf{a})} \tag{4.11}$$

A particular crystallographic plane (hkl) in the real space is expressed in the reciprocal space with the reciprocal lattice vector, $\mathbf{d_{hkl}}$ by

$$\mathbf{d_{hkl}} = h\mathbf{a}^* + k\mathbf{b}^* + l\mathbf{c}^*. \tag{4.12}$$

The crystal is placed in the middle of an Ewald sphere with a radius of $1/\lambda$ (Fig. 4.18). Diffraction spots from a particular (hkl) plane is observed only when corresponding reciprocal lattice vector lies on the surface of the sphere. An example of such diffraction process is presented in figure 4.18 where an incident X-ray with propagation vector, k_0 hits a crystal at the origin of the sphere. The scattered vector, k_1 that corresponds to the diffraction from the (hkl) plane lies on the surface of the sphere and will, therefore, be observed as a spot. If the incident X-ray passes straight through the crystal, it has the lattice point (000) on the surface of the crystal. Since k_0 and k_1 have the same length of $1/\lambda$, the incident and diffracted beam will be of the same wavelength if the scattering process is elastic. With

the rotation of the crystal or the incident beam, more diffraction spots that intercept with the surface of the sphere appears that allows a complete structural characterization of the material.

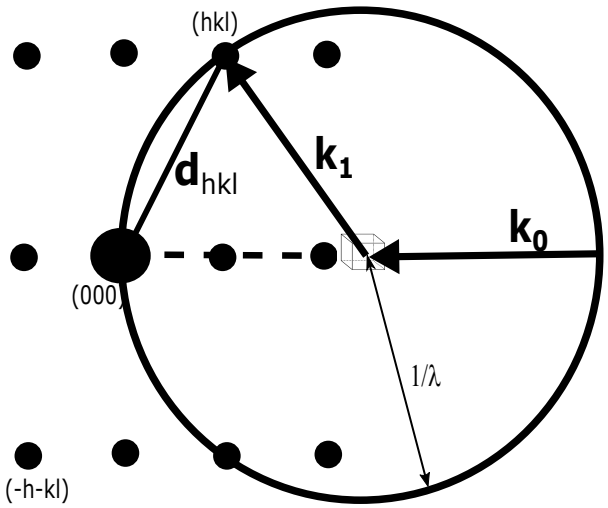

Figure 4.18: Ewald sphere for X-ray diffraction in a periodic lattice of discrete atoms.

Scattering from particular (hkl) of a unit cell is expressed by the structure factor, F_{hkl} which is written as,

$$F_{hkl} = \sum_{j=1}^{N} f_j(\frac{sin\theta_{hkl}}{\lambda}) e^{2\pi i(hx_j + ky_j + lz_j)} \tag{4.13}$$

where N is the number of atoms in the unit cell, $f_j(\frac{sin\theta_{hkl}}{\lambda})$ is the atomic scattering factor of atom j that is located in (x_j, y_j, z_j). The intensity of the diffracted beam from (hkl) is proportional to the $|F_{hkl}^2|$. A fourier transformation of the intensities obtained from equation 4.13 allows to obtain the electron density distribution in the real space by,

$$\rho(x,y,z) = \frac{1}{V} \sum_{h} \sum_{k} \sum_{l} |F_{hkl}|.e^{i\phi_{hkl}} e^{2\pi i(hx_j + ky_j + lz_j)} \tag{4.14}$$

where, V is the volume of the unit cell, ρ is the electron density, $|F_{hkl}|$ and $e^{i\phi_{hkl}}$ are the

amplitude and phase of the structure factor, respectively.

Equation 4.14 implies that a complete crystal structure determination requires information about both the phase, $|F_{hkl}|$ and amplitude, $e^{i\phi_{hkl}}$ of the structure factor. However, the observed intensities from a X-ray diffraction experiment only contain the $|F_{hkl}|$ ($I \propto F_{hkl}^2$) values and the phase component $e^{i\phi_{hkl}}$ remains unknown. The situation is defined as the phase problem which is overcome using two primary methods, the Patterson, and the direct method.

The Patterson method employs a map produced from the known values ($|F_{hkl}|$) according to equation 4.15 [134]. An ideal electron density solution obtained using equation 4.13 would produce a contour map where a peak will represent an atomic site. The Patterson method, on the other hand, generates a contour map with a peak corresponding to vectors between a pair of atoms which is used to determine where the atoms lie relative to each other. The peak width obtained from Patterson map have the contribution from a pair of atoms which is much larger compared to the peak from electron density map. The situation complicates identification of individual peaks due to excessive overlap especially for crystals containing atoms of similar atomic numbers. The method is useful for solving crystal structure with heavy atoms.

$$P(x,y,z) = \frac{1}{V}\sum_h \sum_k \sum_l |F_{hkl}| e^{2\pi i(hx_j + ky_j + lz_j)} \tag{4.15}$$

The direct method attempt to determine the phases directly from the observed intensities. The method relies on the assumption that crystal is made of similarly shaped atoms and the electron density in the unit cell cannot be less than zero. Then, some statistical relationship is derived between sets of structure factors that is used to generate a set of the trial phases and thus, the corresponding electron density map. The trial and error method is repeated

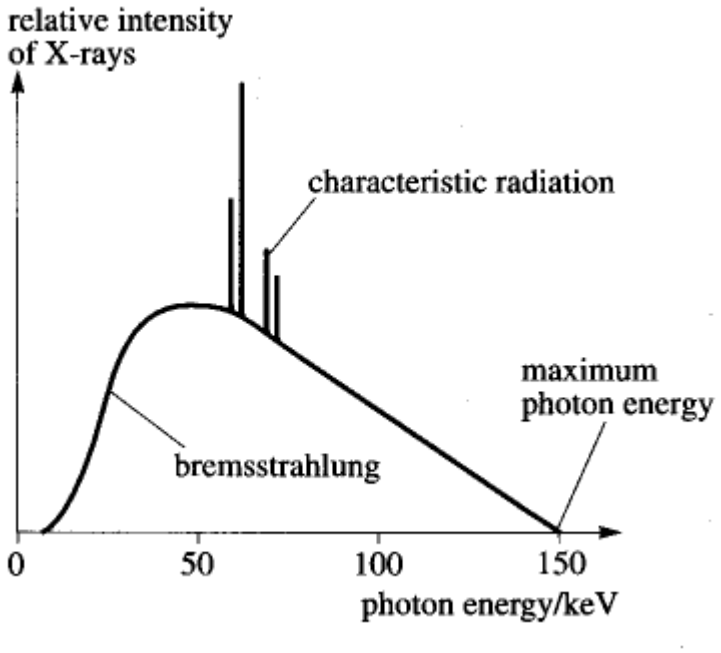

Figure 4.19: A X-ray emission spectra showing the gradually changing Bremsstrahlung and sharp characteristic emission. [Source: koukalaka.wordpress.com/tag/cathode-rays/]

until an acceptable solution is obtained.

4.3.1 X-ray generation

X-rays are generated using the braking radiation or Bremsstrahlung. A metallic cathode is first heated to a high temperature (below the melting point) and, a voltage is applied between the cathode and anode. The resulting electric field pulls the higher energy electrons from cathode towards the anode. When the electrons reach the anode, they transfer part of their kinetic energy due to acceleration to the atomic and conduction electrons which are then excited to higher energy level. When these excited electrons are reverted to their original energy level, electromagnetic radiation of Bremsstrahlung continuous or characteristic type X-ray are emitted. The Bremsstrahlung continuous type X-rays have a wide range

of wavelengths (Fig. 4.19) and, can be generated with any anode material. For a certain potential drop, V, the smallest wavelength that can be generated by an X-ray tube is given by,

$$\lambda_{min} = \frac{h\,c}{e\,V} \tag{4.16}$$

where, h is the plank constant, c is the speed of light and e is the elementary charge of electrons.

Characteristic X-ray radiations are evident as sharp peaks in the spectrum (Fig. 4.19). When the incoming electrons strike an anode material, electron from a particular energy level is excited to a higher and unoccupied state which leaves a hole in the shell. Another electron from the higher energy level then fall into the low energy empty shell with the emission of a photon with wavelength,

$$\lambda = \frac{hc}{E_{higher} - E_{lower}} \tag{4.17}$$

where, E_{higher} and E_{lower} are the energies of the higher orbital and lower orbital, respectively. Since, the orbital energies are a specific property of a particular atom, the wavelength of the characteristic X-ray peak depends on the type of anode materials used. The strongest characteristic emission is observed for de-excitation involving the first level of the L-shell into the K-shell which is defined as K_α and usually used for X-ray diffraction experiments. The phase identification for polycrystalline samples in this work was performed on a *PANalytical X'Pert Pro diffractometer* with Co Kα_1 radiation. The single-crystal diffraction (SCD) was acquired using the *Bruker Smart Apex2 CCD* with Mo Kα_1 radiation on a tiny crystal piece. The MAX3D [135] software was used to visualize the reciprocal space that

confirmed the crystallinity of the material. All the crystal structure was solved using the SHELXS and SHELXL [136] software packages.

4.4 Neutron diffraction

Neutron diffraction is a powerful tool that is employed to overcome challenges and limitations of X-ray diffraction. The neutron diffraction studies of several compounds discussed in the thesis were performed at the Canadian Neutron Beam Centre in Chalk River on the C2 High-Resolution Powder Diffractometer with a wavelength of 1.33Å. The diffraction data were collected on about 4 grams of the powdered sample, sealed in a thin-walled vanadium tube under argon atmosphere. Refinement of the diffraction data was performed using the full-profile Rietvelt refinement implemented in the FullProf program [137–139]. The magnetic configurations were generated with the representation analysis program SARAh [140].

The phenomenon of X-ray scattering is based on scattering by the electron cloud. Consequently, the technique becomes inefficient to locate lighter elements properly when they are present alongside heavy elements due to weaker scattering from a small concentration of electrons. The X-ray diffraction also fails to properly distinguish between elements that have atomic numbers closer to each other as they have similar scattering power. Another downside of the X-ray diffraction method is the loss of intensity at higher 2θ angles due to the angular dependence of the atomic scattering factor that makes the refinement of crystal with those data inefficient.

Neutrons, on the other hand, are neutral particles that interact with the atomic nuclei and, the scattering power thus depends on the size of the nucleus. Figure 4.20 shows the

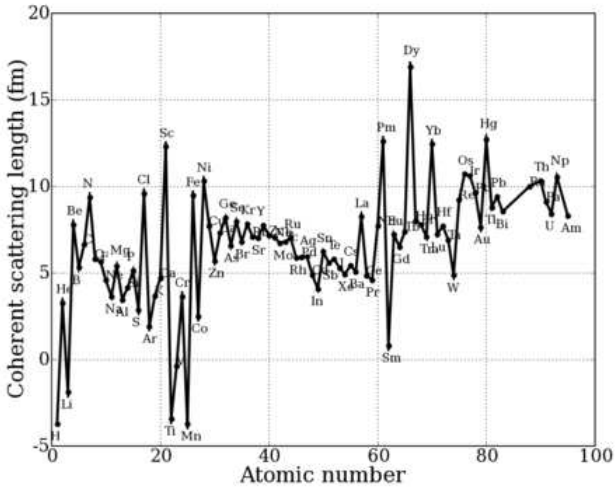

Figure 4.20: Neutron scattering length of elements as a function of atomic number. [Source: gisaxs.com/index.php/Neutron_scattering_lengths]

neutron scattering length of elements in the periodic table as a function of the atomic number which indicates that the scattering power is not a function of the atomic number and there is smaller variation between the scattering of the heavier and lighter elements. Therefore, determination of crystal structure of compounds consisting of both heavier and lighter elements is more feasible. It can also be seen from figure 4.20 that elements with similar atomic number have much different scattering lengths in contrast to scattering by electrons in X-ray diffraction. These variations in scattering length are due to the resonance absorption causing a compound nucleus formation that reduces the scattering cross-section. The magnitude and sign of the resonance contribution are responsible for variation in the scattering lengths for elements that have similar electron density. Also, the atomic nucleus is approximately four to five orders of magnitude smaller than the wavelength of the neutron. Therefore, the nucleus can be treated as point scattering source which implies that the scattered intensity does not have any angular dependence and diffraction maximum can also be

observed at higher 2θ values.

Besides, neutrons also posses a magnetic dipole moment that interacts with the magnetic moments in the solid occurring from the electrons occupying incomplete shell. The resulting diffracted intensity contains both nuclear and magnetic contribution. Unlike the nuclear intensity, however, the magnetic scattering is treated in a similar manner as X-ray with an angular dependence of the scattering length, b_M that is expressed as,

$$b_M = sin\beta(\frac{e^2\gamma}{m_e c^2})Sf_s \tag{4.18}$$

where, e is the elementary charge, γ expresses magnetic dipole moment of the neutron, m_e is the mass of electron, c is the speed of light, S is the total spin angular momentum, and f_s is the magnetic form factor. The use of neutron scattering thus allows determination of the magnetic structure as well.

4.4.1 Neutron generation

The neutron is an unstable fundamental particle discovered by Sir James Chadwick in 1932 [141]. It is electrically neutral particle consisting of positively charged protons and negatively charged π mesons. Within the nucleus, the π mesons are continuously exchanged with other protons. The orbit of the π mesons around the proton gives rise to magnetic dipole moment for the neutron. The neutron for a neutron scattering experiment is usually generated either by nuclear fission from a reactor source or the spallation source. A typical research reactor uses the fission product from a reaction involving absorption of neutrons by atoms and subsequent chain reaction. One such reaction involving Uranium is

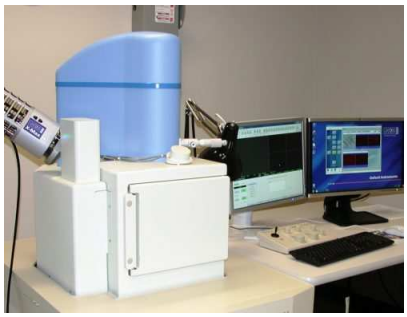

Figure 4.21: JOEL6610LV SEM/EDX system used in the characterization of the microstructure and chemical composition of the phases.

shown in equation 4.19 which is a common source for many reactors.

$$^{235}_{92}U +^{1}_{0} n \rightarrow^{236}_{92} U \rightarrow^{144}_{56} Ba +^{89}_{36} Kr + 3\,^{1}_{0}n + 177MeV \tag{4.19}$$

More intense neutrons are produced in the spallation sources by bombarding heavy nuclei with high energy light particles like protons or alpha sources.

The fast neutrons produced by a reactor or pulsed sources are usually too penetrating to be used in a diffraction experiment. To make them operable, they are often thermalized through interaction with a moderator material like water, heavy water, and pure graphite.

4.5 Scanning electron microscopy/energy dispersive X-ray spectroscopy (SEM/EDX)

The scanning electron microscopy (SEM) combined with the energy dispersive X-ray spectroscopy (EDX) in this work has been done the Ni_2MnSi sample on a JEOL 6610LV system (Fig. 4.21).

In an SEM system, a beam of electrons is generated using a tungsten filament or field

emission gun source under high vacuum. The electron beam is then accelerated by a high voltage and passed through the system of apertures and lenses to produce a thin electron beam which scans the specimen surface by means of a scan coil [142].

The EDX system that is usually incorporated with the SEM is used to determine the composition of the material being studied. The system works based on the principles of characteristics X-ray discussed earlier (Fig. 4.19). In the operation of EDX, the electron beam generates X-rays within the samples being studied that may have the energies characteristics of the constituting element. Measurement of those energies allows accurate determination of the element. Furthermore, a precise control of the EDX system allows determination of the concentration of the elements in the compound [142].

4.6 High resolution transmission electron microscopy (HRTEM) and electron energy loss spectroscopy (EELS)

The high-resolution transmission electron microscopy (HRTEM) and electron energy loss spectroscopy (EELS) has been done on a (0001) oriented $Mn(Ni_{0.6}Si_{0.4})_2$ single crystal sample using the FEI Titan 80-300 LB system that was incorporated with the K2 summit direct electron detection camera [143]. The data collection was done by Dr. Andreas Korinek at the Canadian Centre for Electron Microscopy.

4.7 SQUID magnetometry

The magnetization measurements in this work was performed with a Quatum design magnetic property measurement system (MPMS) with a maximum error of 0.5% in the obtained

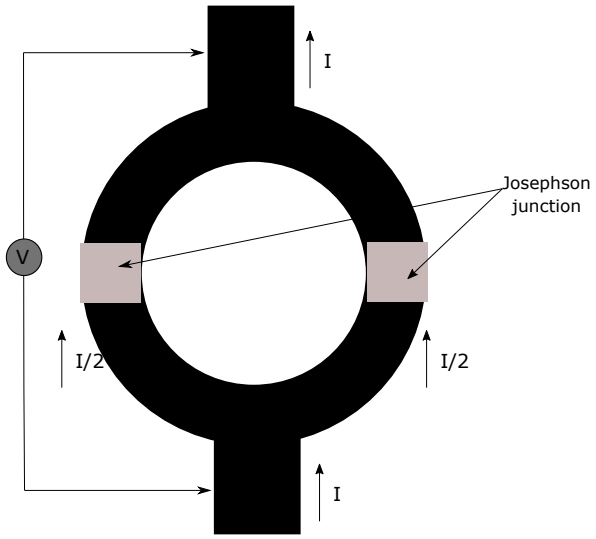

Figure 4.22: Schematic of SQUID device showing the formation of two Josephson junctions.

results. Superconducting quantum interference device (SQUID) of the MPMS is a powerful tool that can measure the magnetic properties of a material in extremally small magnetic fields (as small as 10^{-14} Tesla) and was used extensively in this work for magnetic characterization. The device consists of a loop formed with two semi-circular superconductors separated by two insulating links that form two Josephson junctions (Fig. 4.22). In the absence of an external magnetic field, when a current I is applied through the junction; it flows equally through both the junction by splitting into half as I/2. If an external field is applied, a screening current, I_s flows through the loop that generates another magnetic field to cancel the magnetic flux. The current, I_s causes a difference with a I/2+I_s flowing through one junction and I/2-I_s in another. When the current in any of the junction is more than a certain critical current, a voltage is generated across the junction. A SQUID magnetometer operates by moving the sample across the superconducting loop in the form of a first or second order gradiometer. The output voltage due to the applied field is measured as a function of sample position that has the form of flux profile. Therefore, determination

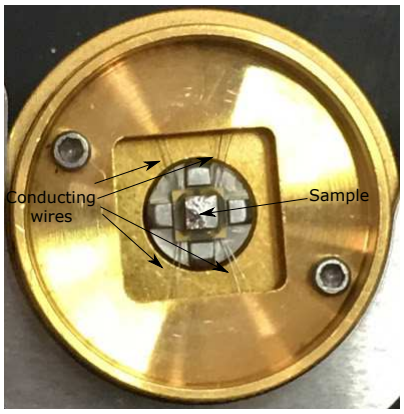

Figure 4.23: The thermal puck with a mounted sample for heat capacity measurement.

of initial sample position is an important task in SQUID measurement. With the fitting of measured flux profile of the sample to that of expected for a point dipole, the magnetization is deduced. The incorporation the SQUID in MPMS allows to measure magnetic properties from temperature as low as 2 K to up to 400 K. Since, the SQUID magnetization requires the flux profile obtained by rotation of the sample around the pick up loop at every temperature or magnetic field of measurement, the process is usually time consuming.

4.8 PPMS heat capacity measurement

The physical property measurement system (PPMS) is an unique equipment that allows accurate characterization of different physical properties of materials. The system consists of a three-walled dewar that allows cooling down from room temperature to up to 1.7 K by using liquid helium as refrigerants. The system is also equipped with a superconductive electromagnet that can create magnetic field up 9 Tesla. In this work, the heat capacity of the materials has been measured using the PPMS system with a high precision of $\sim$0.5%.

PPMS measure heat capacity at a constant pressure, C_P $(= (\frac{dQ}{dT})_P)$ with the Quantum design heat capacity option that controls the heat added and removed from the system as result of a temperature change. The sample is mounted in a platform (Fig 4.23) with a small amount of Apiezon N grease that provides the required thermal contact. The sample platform is connected to the thermal bath (the puck) by eight thin wires. During the measurement ultra-high vacuum is maintained to provide good thermal conductance between the sample platform and puck. Before measuring the sample, the heat capacity of the system with the grease is measured separately. During the measurement, the sample is heated at constant power for a specific period of time which is then followed by cooling for the same duration. The entire temperature response is then fitted with a model to deduce the heat capacity of the material.

4.9 Electrical resistivity measurement

In general, the resistivity of a material is usually measured in terms of resistance and specimen geometry with the two point method which can be expressed as,

$$\rho = \frac{RA}{L} \tag{4.20}$$

where, R is the resistance, A is the cross-sectional area, and L is the length of the sample. The resistivity measured using this technique also contains contributions from the resistance between the contact wire. The additional contact resistance causes a challenge in determining actual resistivity especially for samples with low resistance. Also, the metal contacts can sometimes form a junction with the sample being measured to give an incorrect estimation.

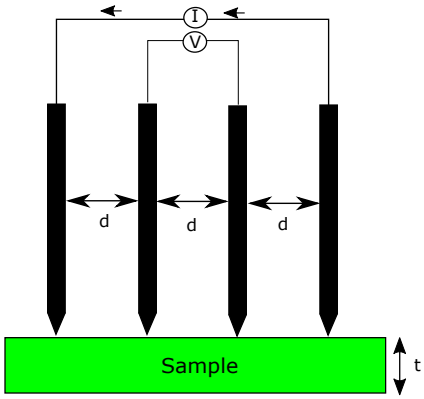

Figure 4.24: A four point resistivity measurement setting.

The four point measurement technique overcomes the limitations of the two point technique and can be used to measure the resistivity of a sample with arbitrary geometry but uniform thickness. A typical four point measurement setting is shown in figure 4.24. The system consists of four equally spaced probes with current passed through the outer probes and voltages being measured through the inner probes. For thicker samples, the bulk resistivity can be expressed as,

$$\rho = \frac{\pi t}{ln(\frac{sinh\,(t/d)}{sinh\,(t/2d)})}\frac{V}{I} \tag{4.21}$$

where t is the sample thickness and d is the probe spacing. If the sample thickness is smaller than half of the probe spacing (t<d/2), the resistivity is computed as,

$$\rho = \frac{\pi}{ln2}\frac{V}{I}t \tag{4.22}$$

Electrical resistivity in this work has been measured with a four point measurement system built in the lab using a Keithley 2182A nanovoltmeter with Keithley 6221 current source. The resistivity measurement from 2 K to 302 K has been done with the system attached to the PPMS device for temperature variation. The sample was mounted on a

platform with a spring-loaded, point-contact potential and current leads. The potential drop was measured in Delta mode as the average of 100 current reversals. The high temperature measurements were done with a separate system in a resistance furnace inside the quartz tube under argon protective atmosphere. Kethley 2400 sourcemeter was used in this case to control current and measure potential drop. A separately developed ceramic holder with a pressure-loaded, point-contact potential and current leads was used in high temperature resistivity measurements. The temperature was controlled with the thermocouple in the vicinity of the sample. In this work, the electrical resistivity was measured on the arbitrary shaped Co_2MnSi and $Mn(Ni_{0.6}Si_{0.4})_2$ samples having uniform thicknesses of 3.41 mm and 3.58 mm, respectively.

4.10 Dilatometry measurement

The dilatometry measurements of Co_2MnSi were carried out on a push-rod dilatometer system with a cylindrical sample that was 33 mm long having a non-uniform diameter of $\sim$2 mm.

The push rod dilatometry is a useful technique that is based on the detection of the length change of materials. Here, the sample lies between the tips of a fixed quartz rod and a frictionless sensing rod. The whole setting is placed on a furnace for temperature variation. Any length change as result of a temperature variation is transmitted to a recording system though the sensing rod. The temperature change is measured by a thermocouple attached near the sample. Dilatometry has been used successfully before to study the magnetic phase transitions as these phase changes are usually associated with a variation in the length change response of the material [144–147].

4.11 Theoretical calculations

The first-principles calculations were carried out within a linear augmented plane wave method using the density functional theory (DFT) implemented in WIEN2k [64] and VASP [148, 149] package. Density functional theory is a widely used theoretical approach to compute electronic properties of materials using an approximate solution of Schrödinger equation with a reasonable balance between accuracy and scalability.

Physical properties of any given system can be determined by solving the corresponding many-body Schrödinger equation [150],

$$H\Psi(\mathbf{R},\mathbf{r}) = E\Psi(\mathbf{R},\mathbf{r}) \tag{4.23}$$

where, *H* is the Hamiltonian, *E* is the energy eigenvalue, $\Psi(\mathbf{R},\mathbf{r})$ is the corresponding eigenstate or the wave function, $\mathbf{R}$=$\{\mathbf{R}_n, n = 1, ..., K\}$ is a set of nuclear coordinates and $\mathbf{r}$=$\{\mathbf{r}_i, n = 1, ..., N\}$ corresponds to the electronic coordinates. The Hamiltonian, *H* that describes the coulombic electrostatic interactions between atomic nuclei and electrons can be written as,

$$H(\mathbf{R},\mathbf{r}) = T_i(\mathbf{R}) + U_{ii}(\mathbf{R}) + T_e(\mathbf{r}) + U_{ee}(\mathbf{r}) + U_{ie}(\mathbf{r},\mathbf{R}) \tag{4.24}$$

$T_i(\mathbf{R})$ is the kinetic energy operator for nuclei and $U_{ii}(\mathbf{R})$ is the potential energy operator that describes the nuclei-nuclei interactions. $T_e(\mathbf{r})$ and $U_{ee}(\mathbf{r})$ are the corresponding kinetic energy and potential energy operator for electrons, respectively. $U_{ie}(\mathbf{r},\mathbf{R})$ operator represents the external potential or the potential energy due to the interaction of electrons with the nuclei. Solving Eq. (4.23) is practically impossible for most of the solids within a full quantum mechanical framework which implies that both the electrons and nuclei are in

constant motion. A full treatment of the problem requires the knowledge of the locations of nuclei and electrons for any particular state of the system.

Combining the postulates of Born-Oppenheimer approximation [151], mean field theory by Hartree [152], Hartree-Fock theory [153], and the Hohenberg-Kohn [154], a powerful method to simplify the problem and calculate the ground state properties of materials was introduced by Kohn-Sham [155]. The work of Kohn-Sham provided the basis of modern density functional theory and is presently called as Kohn-Sham density functional theory. The simplified Kohn-Sham Hamiltonian, H_{KS} is expressed as,

$$H_{KS} = -\frac{\hbar^2}{2m}\nabla^2(\mathbf{r}) + U_{Hartee} + U_{xc} + U_{ie} \tag{4.25}$$

where, the first term is the Kohn-Sham kinetic energy operator. U_{Hartee} is known as the Hartree energy that represents the interaction of an electron with the time averaged electron density of the system which is expressed as,

$$U_{Hartree}(\mathbf{r}) = \frac{e^2}{4\pi\epsilon_0}\int \frac{\rho(\mathbf{r}')}{|\mathbf{r}-\mathbf{r}'|}\, d\mathbf{r}' \tag{4.26}$$

where, $\rho(\mathbf{r}')$ is the time averaged density of the system. For a system with N electrons, the ground state density is expressed as,

$$\rho(\mathbf{r}') = \sum_{i=1}^{N} |\Psi_i(\mathbf{r}'|^2 \tag{4.27}$$

U_{xc} in equation 4.25 is the exchange correlation functional. There are several schemes of exchange correlation functional applied in DFT. In this work, the generalized gradient approximation (GGA) exchange correlation functional [156] along with Hubbard correction U has been used to properly address the electron localization of 3d states of transition

metals. In addition, some energy calculations were also performed with the computationally expensive HSE06 hybrid functional that estimates the exchange interaction more efficiently [157].

DFT aims at solving the Schrödinger equation with the Kohn-Sham Hamiltonian, H_{KS} for any interacting many electron systems. Because of the consideration of all the possible interaction terms almost accurately, the majority of the electronic structure calculations for solids are based on DFT.

Chapter 5

Results

5.1 Characterization of the Co_2MnSi based Heusler compound

5.1.1 Single crystal diffraction (SCD)

Co_2MnSi crystalizes with the $L2_1$ type crystal structure within the space group 225 $Fm\overline{3}m$. The Co, Mn, and Si atoms are situated in the Wyckoff position 8c (3/4, 1/4, 1/4), 4a (0,0,0) and 4b (1/2, 1/2, 1/2), respectively. The refined single crystal structural parameters are summarized in Table 5.3 and 5.4. The obtained crystal structure was found to be in good agreement with previously published results [105, 158–162] available in the inorganic crystal structure database (ICSD) [163]. Note that, the refined XRD-SCD parameters did not yield the information on the transition metal Co-Mn antisite disorder that is one of the main reasons for the weakening of half-metallicity in Co_2MnSi compound. The absence of the very well known disorders can be explained by the similar X-ray scattering power of Co and Mn. Consequently, disorders in the range of $\sim$ 10% that was observed previously

by Ravel et al. [94] are indistinguishable with XRD.

Table 5.3: Crystallographic data for Co_2MnSi single crystal obtained from refinement of X-ray diffraction data (Mo K_α radiation, 298K)

Refined composition	Mn Co_2Si
Space group	$Fm-3m$
Lattice constant $(\mathring{A})$	$5.6585(4)$
Volume $(\mathring{A}^3)$	$181.18(2)$
$\rho_{calc}(g/cm^3))$	7.3642
Z	4
2θ range	$12.48-88.3$
Index ranges	$-7 \leq h \leq 10, -10 \leq k \leq 11 - 9 \leq l \leq 11$
Reflections collected	537
Independent reflections	$58[R_{int} = 0.0168,\ R_{sigma=0.0098}]$
Data/restraints/parameters	$58/0/4$
Goodness-of-fit on $\lvert F\rvert^2$	1.185
Largest diff. peak/hole (e/$\mathring{A}^3$)	$0.72/-0.59$
R indices $[I >= 2\sigma(I)]$	R_1=0.0175 wR_2 =0.0487

Table 5.4: Occupancy and isotropic displacement parameters for Co_2MnSi single crystal.

Atom	x	y	z	Site	Occupancy	U_{eq} (Å^2)
Co	3/4	3/4	1/4	8c	1.00008	0.00406(18)
Mn	1/2	1/2	0	4a	0.99984	0.00404(19)
Si	0	0	1/2	4b	0.99984	0.005(3)

5.1.2 Neutron powder diffraction

In contrast to X-ray, neutron beam offers coherent scattering lengths of 2.53 fm for Co and -3.73 fm for Mn, respectively. As a consequence, antisite disorder between Co and Mn atoms becomes distinguishable. In this work, the neutron diffraction data were collected at 4 K, 100 K, and 298 K in an effort to accurately refine the structure, the magnetic

moments and their variation with decreasing temperature. One of the challenges in performing a precise refinement for Co_2MnSi is the lack of paramagnetic state diffraction data that makes it difficult to differentiate between the structural and magnetic reflections. An ideal approach would involve conducting a refinement on data collected above the Curie temperature to obtain structural information which can then be used successively for magnetic structure determination. Nevertheless, the high Curie temperature of Co_2MnSi does not permit the data collection in the paramagnetic state. Furthermore, as discussed earlier, X-ray diffraction can not also successfully capture the Co-Mn disorder accurately which makes refinement more challenging.

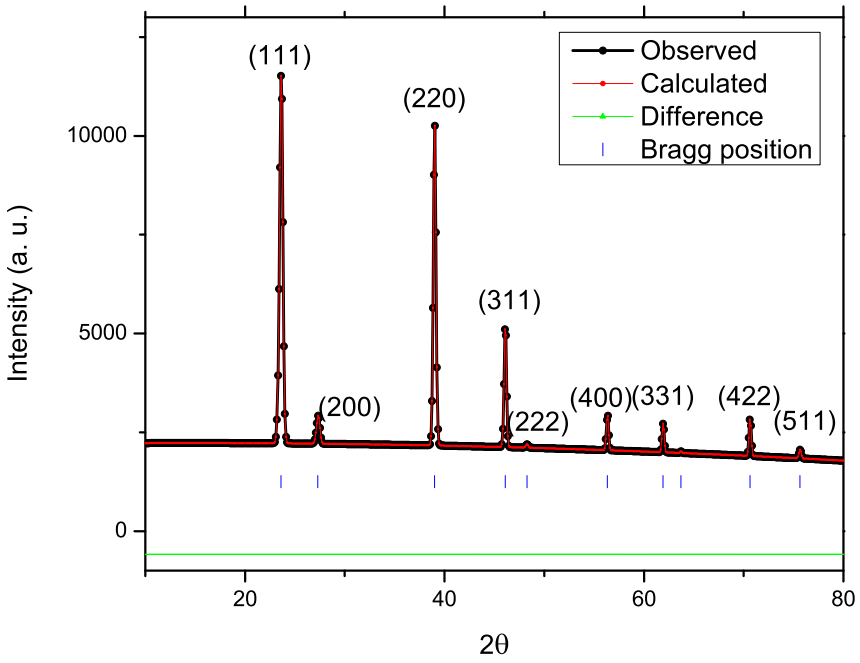

Figure 5.25: Neutron pattern simulation of the magnetic structure with the parameters obtained from the first-principles calculation of defect free Co_2MnSi.

Simulation of magnetic reflections with the theoretically obtained magnetic moments

(Fig. 5.25) suggested the presence of three very dominant reflections (111), (220) and (311) for Co_2MnSi. Among these, the intensity of (111) and (310) are also significant to determine the Mn-Si disorder as they fall into the category with h, k, l all being odd [105]. As a result, separating these magnetic reflections becomes crucial for a good refinement.

The pattern simulation in Fig. 5.25 showed that all the major magnetic peaks lie below the 2θ value of 46.5^0. If the weak magnetic reflections above 46.5^0 are considered negligible, it can provide a means to obtain Co-Mn disorder more accurately. In this work, the structural refinement for Co_2MnSi was performed at higher angles within the range (47^0 - 117^0). Such a refinement is feasible in the present case because in neutron scattering stronger reflections are observed at higher angles that allow proper identification of elements. The refinement profile is shown in Fig. 5.26a and refined structural parameters are listed in Table 5.5. It can be seen that Mn and Co tend to from antisite disorder among themselves with $\sim$6.5% (3.25$\times$2) Co sites being occupied by Mn and $\sim$7.6% Mn sites being replaced by Co. Refinement involving a portion of Mn and Si sitting in each other's sites yielded almost negligible occupancy and was ignored in the subsequent refinement. The obtained occupancy parameters were kept constant and used in the successive magnetic refinements at 298 K, 100 K, and 4K. It should be noted that although, the refinement ignored the presence of weaker magnetic reflections at higher angles, their presence in the refinement should be within the limit of experimental errors.

The magnetic structure at 298 K was refined with all structural parameters obtained from the higher angle refinement. The initial values of the magnetic moments were taken from our first-principles calculation that will be discussed in an upcoming section. The

solution of the magnetic structure was based on the representation analysis approach using SARAh [140]. For the ordering, wave vector k = (0 0 0) was used since no extra magnetic reflection was observed. The method yielded only one basis vector, γ_9 that corresponds to a ferromagnetic interaction. The final refined structural parameters are listed in Table 5.5, and the refinement profile is shown in Fig. 5.26b. Our obtained magnetic moment values of 2.432(37) $\mu_B/f.u.$ for 4a site (Mn and Disorder Co) and 0.962(30) $\mu_B/f.u.$ for 8c (Co and Disorder Mn) is much smaller compared to the previous results at 298 K [94, 106].

The refinement of the 100 K and 4 K diffraction data were also performed with the occupancy parameters obtained from 298 K high angle structural refinement. No additional reflections were observed at low temperature revealing lack of any structural or magnetic transition below 100 K. The refinement profile is shown in Fig. 5.26c (100 K) and 5.26d (4 K), respectively. The relevant structural and magnetic parameter are listed in Table 5.5. The lattice constant of Co_2MnSi is less sensitive to the temperature, which can be understood by comparing their values at different temperatures. The magnetic moments are increased as the temperature is lowered. Nevertheless, the refined values at 4 K are much lower compared to the results of Webster [105] at the same temperature.

5.1.3 Magnetization behavior

The hysteresis behavior of the Co_2MnSi compound at 4 K, 100 K and 298 K is shows in Fig. 5.27. The compound showed almost identical saturation magnetization of (M_S) 4.94, 4.99 and 4.89 $\mu_B/f.u.$ at 4 K, 100 K, and 298 K, respectively. Previous experimental measurements also reported comparable results of 4.96 $\mu_B/f.u.$ [106] and 5.15 $\mu_B/f.u.$ [94]. The coercive field was found to be $\sim$20 Oe at all three temperatures.

Table 5.5: Refined structural parameters for Co_2MnSi

Temperature	298 K-high angle	298 K	100 K	4 K
Spacegroup		Fm3m		
Lattice constant($\mathring{A}$)	5.6406(4)	5.6406	5.6301(7)	5.6301(2)
Magnetic phase	-	Ferromagnetic		
Co and disorder Mn; and 8c (3/4, 3/4, 1/4)				
Occupancy (Co)		0.9675		
Occupancy (Mn)		0.0325		
B($\mathring{A}^2$)	0.607(2)	0.607	0.4318(13)	0.3565(5)
M($\mu_B/f.u.$)	-	0.962(30)	1.008(16)	0.906(18)
Mn and Disorder Co; 4a (1/2, 1/2, 0)				
Occupancy (Mn)		0.924		
Occupancy (Co)		0.076		
B($\mathring{A}^2$)	0.6877(1)	0.6877	0.4759(5)	0.5561(15)
M($\mu_B/f.u$)	-	2.432(37)	2.456(32)	2.62(20)
Si; 4b (0, 0, 1/2)				
Occupancy (Si)		1		
B($\mathring{A}^2$)	1.0177(14)	1.0177	1.1147(27)	1.1114(16)
χ^2	2.92	5.64	4.44	5.57
R_{wp}	14.5	13.6	13	13.1
R_F	4.38	4.58	6.16	6.23
R_{mag}	-	3.57	2.37	3.64

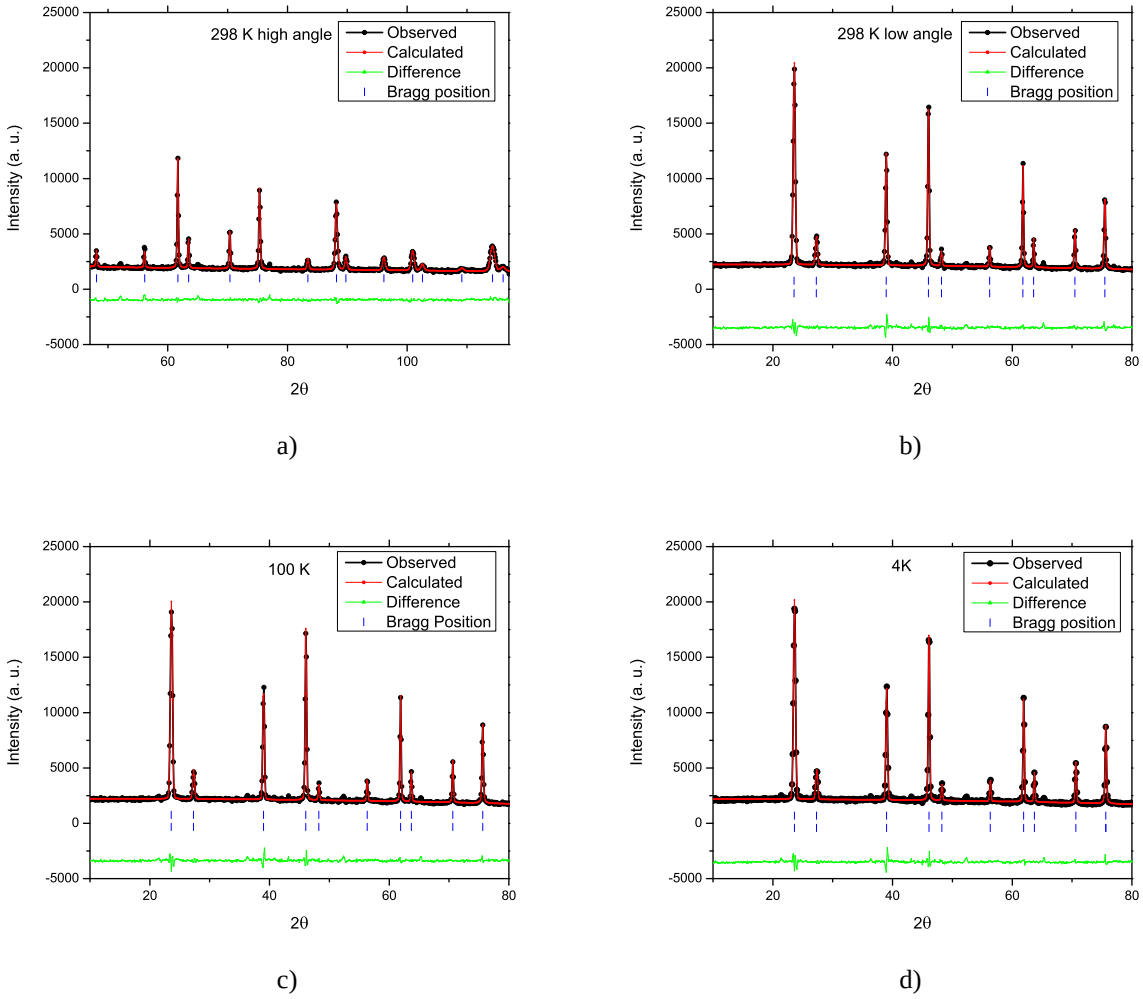

Figure 5.26: Rietveld refinement profile for Co_2MnSi at a) 298 K with high angle structural refinement, and b) 298 K c) 100 K and d) 4 K structural and magnetic refinement.

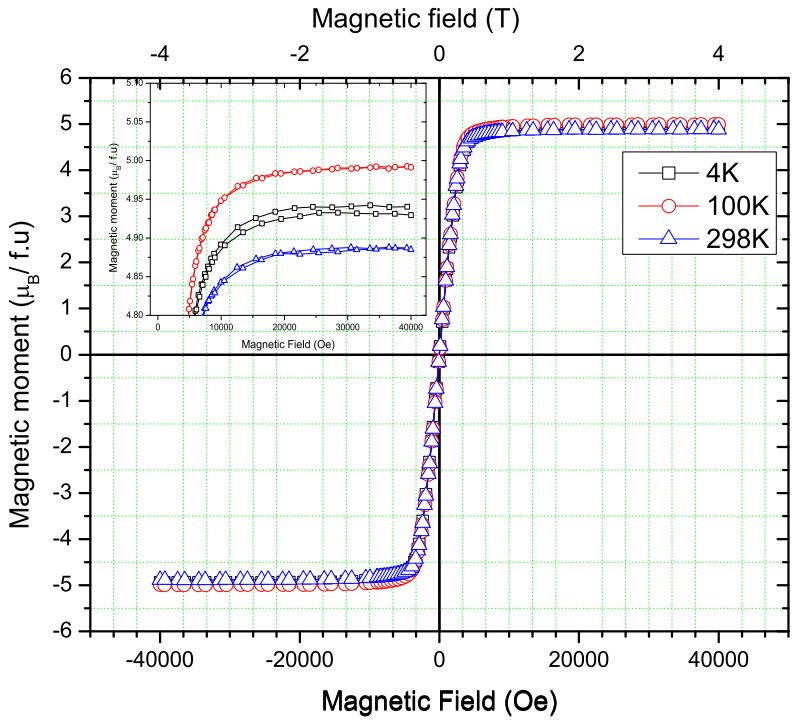

Figure 5.27: Magnetic hysteresis loop of Co_2MnSi at 4 K, 100 K and 298 K, measured with the applied field up to 40 kOe. Inset shows the saturation magnetization at the corresponding temperatures.

5.1.4 Dilatometric measurements

The dilatometric measurements were performed on a single crystal sample to determine the Curie temperature. The technique has been successfully used previously to determine the ferromagnetic to paramagnetic transition temperature of several compounds [144–147]. The change of length, ΔL and the derivative with respect to temperature, $\frac{d(\Delta L)}{dT}$ values as a function of temperature for Co_2MnSi is shown in the Fig. 5.28. It can be seen that the length change starts to deviate from a linear responsive behavior at higher temperatures where the ferromagnetic to paramagnetic phase transition takes place. From the sharp peak in the $\frac{d(\Delta L)}{dT}$, the Curie temperature was identified to be 1018 K which compares well with the previously published value of 985 K [105, 106]

5.1.5 Electrical resistivity measurement

Electrical resistivity variation as a function of temperature in Fig. 5.29a shows a temperature independent behavior below 30 K, indicating that Co_2MnSi is a good metal within that range of temperatures. The residual resistivity, ρ_0 for Co_2MnSi was determined to be $\sim$33.7 $\mu\Omega$.cm. Previous literature showed a wide range of values for ρ_0 with $\sim 2\mu\Omega$.cm for single crystal, to values like 16, 19, 22, 96 and 105 $\mu\Omega$.cm for polycrystals and thin films [95]. The large variation of ρ_0 can be attributed to the presence of different concentrations of impurities and grain boundaries as they significantly affect the transport properties of a system [95]. Our obtained value of $\sim$33.7 $\mu\Omega$.cm, however, agrees well with the theoretically predicted value of $\sim$38 $\mu\Omega$.cm by Kota and Sakuma [164] for the $\sim$7% Co-Mn disorder. The residual resistivity ratio (RRR) at 300 K, i.e., the ratio of the resistance of the sample at 300 K over the resistance at 2 K, was found to be 3.5. The Curie temperature was extrapolated from the high temperature resistivity measurement with an apparent sudden

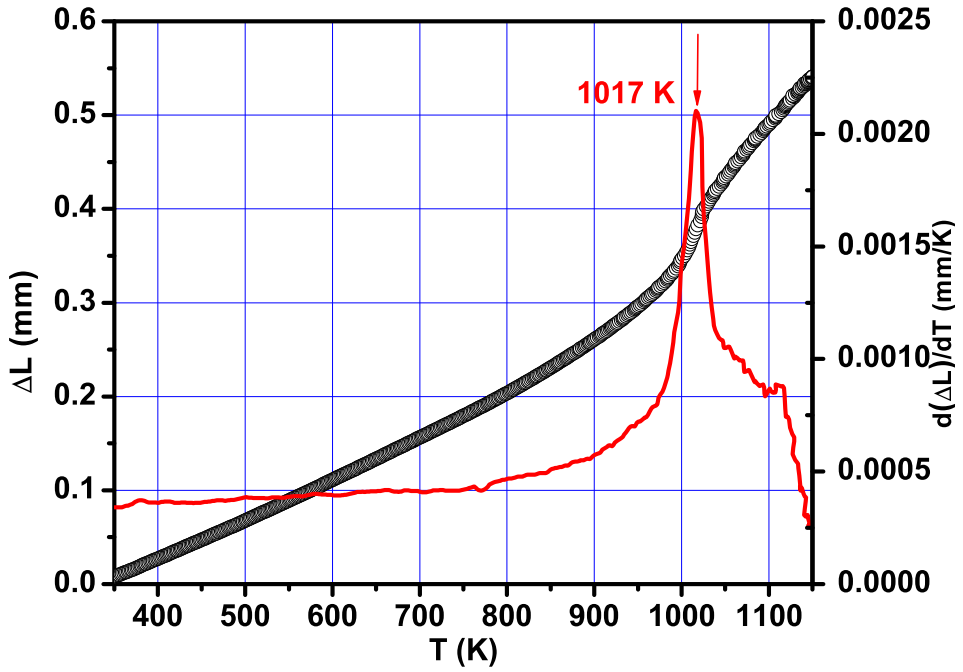

Figure 5.28: ΔL and $\frac{d(\Delta L)}{dT}$ of Co_2MnSi as a function temperature measured from 350 K to 1150 K. ΔL shows a linear response with temperature until near the magnetic phase transition point where the response changes. The Curie temperature was identified to be 1018 K from the sharp peak in the $\frac{d(\Delta L)}{dT}$ vs T plot.

change in the electrical resistivity at higher temperatures (Fig. 5.29b). From the peak of the $\frac{d(\rho)}{dT}$ vs. T plot, the Curie temperature was identified to be 1014 K which corresponds very well to the dilatometry measurements. The RRR value for Co_2MnSi was found to reach $\sim$ 50 near the transition temperature.

5.1.6 First-principle calculations

Calculations were carried out on a pure Co_2MnSi, as well as the structures with different concentrations of disorder that are relevant to the experimental observations. Before energy computation, a complete first-principles structural relaxation was performed. Here, we consider various Co-Mn antisite disorders and discuss their propensity to form in terms of the energy difference with the ideal Co_2MnSi. Note that, our calculations did not include any disorder involving the Si (4b) site as they have not been observed in any experimental investigations including the present work [94, 105, 106]. Four different types of defects were studied with all the calculations done with a 128 atoms unit cell. The first one is a Mn only antisite disorder created by replacing one Co atom to obtain a $(Co_{0.984}Mn_{0.016})_2MnSi$ stoichiometry. The second one corresponds to a Co only antisite with a composition of $(Co_2(Mn_{0.969}Co_{0.031})Si$. The third and fourth type of defects involves disorder between both Co-Mn at concentrations that are relevant to the experimental results. It should be noted that the neutron refinement in this study and other experimental investigations indicated slightly different disorder affinity for the Mn and Co sites. In the first-principle calculations, however, we adjusted the identical disorder occupancy between Co and Mn to preserve accurate stoichiometry. The computed energies are listed in Table 5.6.

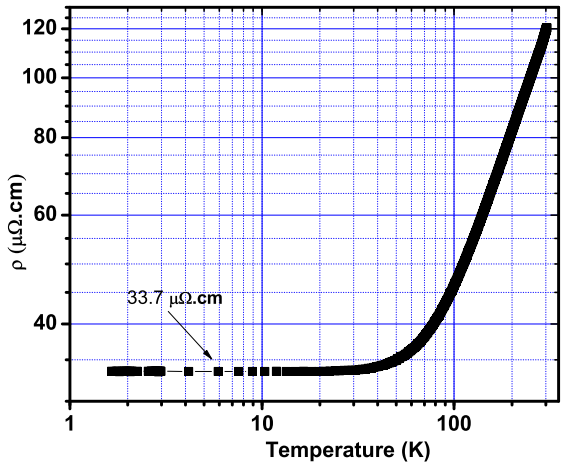

a)

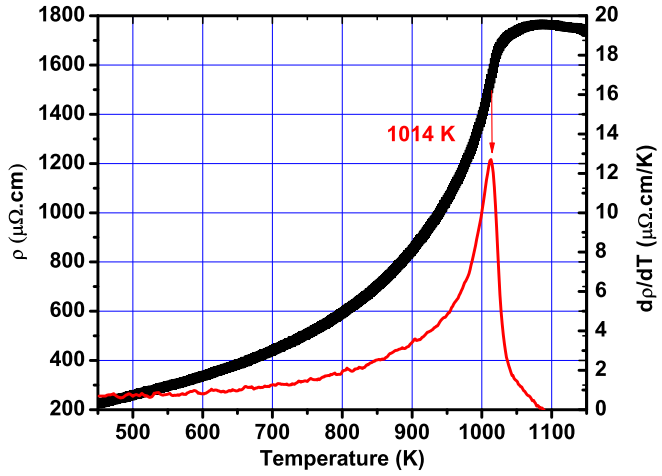

b)

Figure 5.29: a) Low temperature (1.8 K to 300 K) single crystal electrical resistivity, ρ of Co_2MnSi as a function of temperature plotted on a ln scale to identify the temperature independent residual resistivity of $\sim$33.7 $\mu\Omega$.cm. b) High temperature electrical resistivity, ρ and $\frac{d\rho}{dT}$ as function of temperature measured from 450 K to 1150 K. The Curie temperature was determined to be 1014 K from the sharp change in the temperature dependence of $\frac{d\rho}{dT}$.

Table 5.6: Energy required to form a disordered configuration in the 128 atoms supercell Co_2MnSi. The energy for the ideal structure without any defect is taken as 0.

Type of disorder	Composition	Required energy (eV/f.u.)
Defect free	Co_2MnSi	0
One Mn antisite	$(Co_{0.984}Mn_{0.016})_2MnSi$	0.041
One Co antisite	$(Co_2(Mn_{0.969}Co_{0.031})Si$	0.30
Two Co and two Mn disorder	$(Co_{0.969}Mn_{0.031})_2(Mn_{0.938}Co_{0.062})Si$	0.015
Three Co and three Mn disorder	$(Co_{0.953}Mn_{0.047})_2(Mn_{0.906}Co_{0.094})Si$	0.073

From Table 5.6, it can be seen that formation of a single Mn antisite defect in Co_2MnSi requires external energy of 0.041 eV/f.u while the Co counterpart requires 0.3 eV/f.u. However, the formation of these defects also require an additional supply of Mn/Co from the reservoir and expelling of an equivalent concentration Co/Mn from the ideal structure to maintain the stoichiometry. Consequently, generation of only one type of antisite defects can be regarded as highly unlikely as it will require precipitation of excess Co/Mn to balance the stoichiometry. In comparison, the equivalent Mn-Co antisite disorder with ideal stoichiometry is energetically more favorable as they involve identical concentrations of disorder atoms replacing each other to maintain the Co:Mn:Si ratio of 2:1:1. In our calculations, the formation of 6.2% and 9.4% antisite Co-Mn disorder was found to require energies of 0.015 eV/f.u. and 0.073 eV/f.u, respectively. These correspond to thermal energies at temperatures of 173 K and 846 K, which are usually encountered during the experiments. Consequently, the formation of the Co-Mn disorder is energetically favorable. Note that, our computed energies are in good agreement with the reported energies by Pradines et al. [103] with similar defect concentrations.

In the next step, we studied the effect of defect concentrations on the magnetic properties of Co_2MnSi. Here, we compared the ideal Co_2MnSi with the structure containing 6.2% and 9.4% Co-Mn antisite disorder, discussed above. The magnetic moments are listed in

Table 5.7.

Table 5.7: Average magnetic moment from the first-principle calculations. Column "A" stands for the $(Co_{0.969}Mn_{0.031})_2(Mn_{0.938}Co_{0.062})Si$ composition. Column "B" describes $(Co_{0.953}Mn_{0.047})_2(Mn_{0.906}Co_{0.094})Si$ compound.

Atom	Site	Magnetic Moment ($\mu_B/f.u.$)		
		Co_2MnSi	A	B
Co	8c	0.974	1.138	1.114
Mn disorder	8c	-	-0.111	-0.164
Mn	4a	3.49	2.666	2.558
Co disorder	4a	-	0.139	0.18
Si	4b	-0.102	-0.072	-0.069
Interstitial region		-0.298	-0.256	-0.257
Net moment		5.04	4.533	4.311

From Table 5.7, it is evident that the net magnetic moment is significantly reduced with the introduction of the antisite disorder. This suppression is caused mainly by an antiferromagnetic interaction of the Mn antisite disorder with the parent Mn which was also reported in previous theoretical examinations [99, 103]. The emergence of this interaction can be attributed to the reduction of Mn-Mn interatomic distances due to the disordered Mn atoms replacing Co in the 8c site [103]. In the previous study by Pradines et al. [103], it was found that introduction of 6.2% disorder reduces the average magnetic moment of Mn atoms in the 4a to 2.667 $\mu_B/f.u.$ with some Mn atoms coupling antiferromagnetically with the disorder Mn in 8c. As the concentration of disorder increases, more Mn atoms occupy the 8c sites. Consequently, it is expected that antiferromagnetic interaction will be stronger and the reduction of both Mn and hence, the total magnetic moment will be higher, which is reflected in the values for 9.4% Co-Mn swap.

5.1.7 Discussion

Occupancy of Co and Mn antisite disorder

The neutron diffraction data were collected on a polycrystalline sample that was water quenched at 1073 K (800^0C) which necessarily means the system is frozen on the state at that temperature. The refinement of the data found the occupancies of the Mn and Co antisite disorder to be $\sim$6.5% and $\sim$7.6%, respectively (table 5.5) in that state. In contrast, the first-principles calculation showed that the formation of 6.2% and 9.4% equivalent Co-Mn disorder requires a temperature of 173 K and 846 K, respectively. The slight disagreement between the theoretical and experimental observation can be attributed to several experimental and theoretical error factors. Some imbalance can be originating from the smaller theoretically obtained lattice constant which in turn produces slightly lower energy compared to the energy that would be obtained with experimentally observed structures [103]. Additionally, some errors may also be introduced by the experimentally refined antisite disorder with dissimilar amounts of Co and Mn. In contrast, our first-principles calculations suggested the formation of disorder with identical Co and Mn concentrations to be more favorable. Other experimental error factors that are difficult to control can be listed as the contribution from weak magnetic reflections at higher 2θ angle data, evaporation of Mn during arc melting which is a very common problem with Mn based compounds, purity of the starting elements being not perfect, the exact water quenching being less than 800^0C due to the evacuated quartz tube and so on. All these factors can contribute to the observed slight difference in the theoretical and experimental disorder occupancy. Therefore, the first-principles calculated disorder of 9.4% at 846 K and the 1073 K annealed neutron refinement obtained $\sim$6.5-7.6% can be regarded to be in fair agreement with each other.

Comparison of magnetic moments

The first principle calculations predicted a total magnetic moment of 4.53 $\mu_B/f.u.$ for 6.2% disorder and of 4.31 $\mu_B/f.u.$ for 9.4% disorder compared to moment of 5.04 $\mu_B/f.u.$ for defect-free structure. Such suppression with increasing defects was attributed to the antiferromagnetic interactions between Mn atoms that decrease their moment. For the Co atoms, however, an increase in the moment was observed with the introduction of the disorder. These values compare well with results obtained from the neutron refinement. It should be noted that the Mn disorder in Co_2MnSi was found to be in the order of $\sim$6.5%. Obtaining of such a small antiferromagnetic moments ($\sim$-0.111 $\mu_B/f.u.$ from first-principles calculations can be taken as a guide) falls within the error of refinement. Consequently, the refinement was carried out for the particular magnetic sites than individual atoms. The magnetic moments for the $8c$ site that contains Co and disordered Mn were found to be 0.906(18) $\mu_B/f.u.$ at 4 K. In contrast, the first-principles calculation that corresponds to a 0 K condition yielded 1.027 $\mu_B/f.u.$ and 0.95 $\mu_B/f.u.$ for the 6.2% and 9.4% disordered structures, respectively which can be regarded as excellent agreement with experimental observation. The moments for the $4a$ sites at 4 K were refined to be 2.62(20) $\mu_B/f.u.$ which also shows good agreement with the theoretically obtained 2.805 $\mu_B/f.u.$(6.2% disorder) and 2.738 $\mu_B/f.u.$ (9.4% disorder).

Our hysteresis measurement, on the other hand, indicated a saturation magnetization of 4.94, 4.99 and 4.89 $\mu_B/f.u.$ at 298 K, 100 K and 4 K, respectively which is very close to the theoretically predicted value for defect-free 5.04 $\mu_B/f.u.$ where all moments are ferromagnetically aligned. Such a result is not surprising as it indicates that the antiferromagnetic interaction between the Mn atoms is relatively weak in nature. The applied magnetic field

of 4 Tesla aligns all the moments to the direction of the field.

5.2 Characterization of the G-phase compound $Ni_{16}Mn_6Si_7$

5.2.1 Zero-Field Cooled - Field-Cooled Characteristics

Fig. 5.30 shows ZFC-FC magnetic susceptibly of $Ni_{16}Mn_6Si_7$ between 2 K and 350 K under the constant magnetic field of 1000 Oe applied along $< 100 >$, $< 110 >$ and $< 111 >$ directions of the crystal. The data show clearly two transitions at$\sim$50 K and 197 K, the latter in agreement with Kolenda et al. [2]. Additionally, there is a ZFC/FC divergence below 6K suggesting a weak spin freezing effect. Thus, two new transitions are discovered here below the 80 K base temperature of the earlier studies. Further analysis of the data with the Fisher heat capacity [165], $d(\chi T)/dT$ vs. T plot in Fig. 5.31a, shows both transitions quite clearly. The true Néel temperature was identified to be 197 (1) K from the second peak of the graph.

From the inverse FC susceptibly plot along the $< 100 >$ crystal direction, a Curie-Weiss fitting was done above 197 K (Fig. 5.31b). The Curie constant, C of 17.75 (4) emu.K/mol.Oe yielded an effective magnetic moment per Mn atom, μ_{eff}/Mn of 4.83 (24) μ_B which is very close to the effective moment for of 4.90 μ_B for Mn^{3+} (S=2) compared to 5.91 μ_B for Mn^{2+} (S=$\frac{5}{2}$). Some caution should be taken as this fitting region may not be strictly in the paramagnetic regime. The Curie-Weiss temperature, Θ_{CW} were estimated to be -105 (1) K which indicates the presence of a strong antiferromagnetic exchange. Moreover, the susceptibility data continues to increase with decreasing temperature, indicating a persistent paramagnetic contribution which is likely due to the presence of geometrically

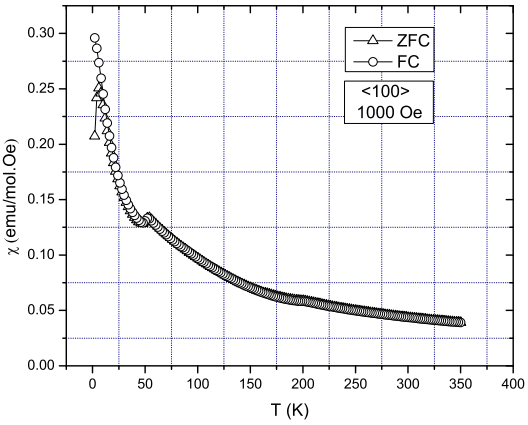

a)

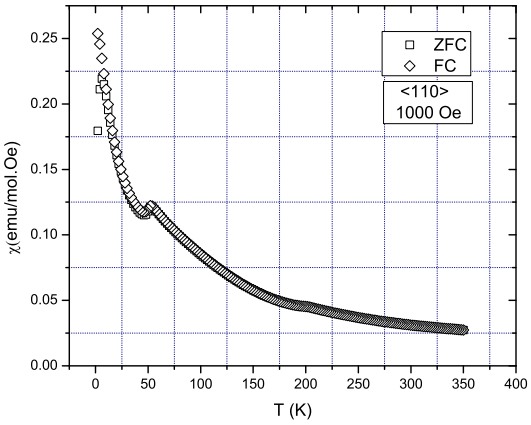

b)

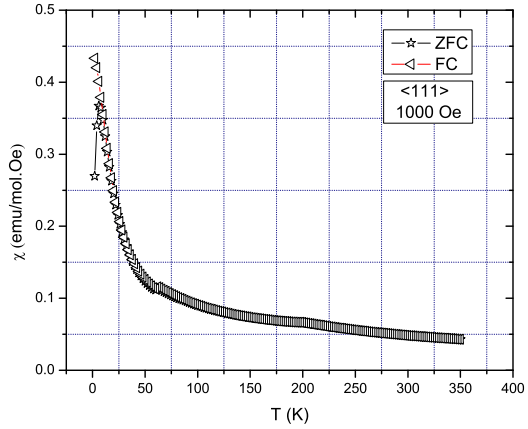

c)

Figure 5.30: ZFC-FC magnetic susceptibility of $Ni_{16}Mn_6Si_7$ crystal at 1000 Oe field applied along a) $< 100 >$, b) $< 110 >$, and c) $< 111 >$..

frustrated paramagnetic ions. ZFC-FC measurement in $< 110 >$ and $< 111 >$ also demonstrated a similar behavior (Figs. 5.30b and 5.30c).

5.2.2 Heat Capacity measurement

Fig. 5.32a shows the heat capacity of $Ni_{16}Mn_6Si_7$ measured under zero magnetic field between 2 K and 302 K. The data clearly depicts a λ anomaly peak at 197 K that corresponds to a transition between antiferromagnetic and paramagnetic states. A second transition at 50 K characterized by a weak, almost undetectable peak in heat capacity data (inset in Fig. 5.32a), is consistent with transition observed in the magnetic susceptibility plots in Fig. 5.30. To obtain the magnetic contribution to the heat capacity of $Ni_{16}Mn_6Si_7$ one needs to subtract that of a suitable lattice match, normally a para magnetic iso-structural compound [166]. A previous study of the magnetic properties of $Ni_{16}Ti_6Si_7$ showed a Pauli paramagnetic like behaviour [68], which was also observed in our measurements of magnetic susceptibility of the compound under an applied magnetic field of 1000 Oe (Fig.5.33). However, the heat capacity as a function of temperature showed a cusp at 140 K for $Ni_{16}Ti_6Si_7$ (closed circles in Fig. 5.32a), which is an indication of a phase transition, which is unexpected, given the data of Holman et al. [68] and our magnetic measurement. The origin of this anomaly is unclear at present, but apart from this feature, $Ni_{16}Ti_6Si_7$ appeared to be a reasonable lattice match. Consequently, the magnetic contribution of the heat capacity for $Ni_{16}Mn_6Si_7$ was thus obtained 5.32b by a direct substraction of the $Ni_{16}Ti_6Si_7$ data. Note that, the 50 K anomaly is now clearly evident. To compute the expected entropy loss for this material requires selection of an oxidation state for Mn. For Mn^{3+} S_{mag} = 80.28 J/mol-K while for Mn^{2+} it is 89.38 J/mol- K. The computed magnetic entropy (Fig. 5.32c) however, showed S_{mag} of 17.14 J/mol.K at 50 K, 94.03 J/mol.K at 197 K and,

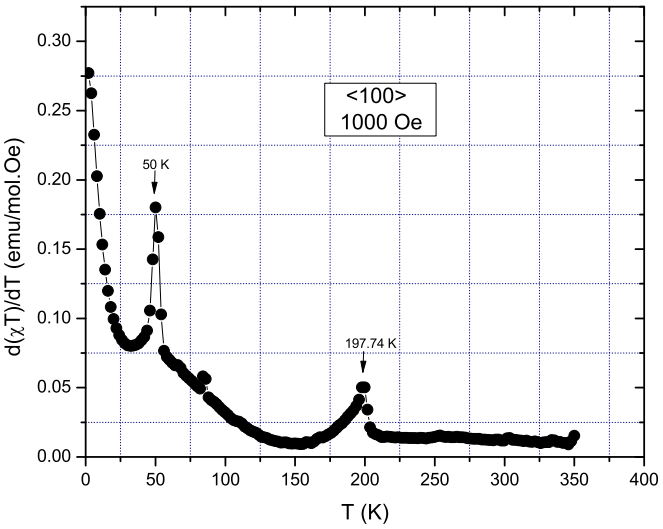

a)

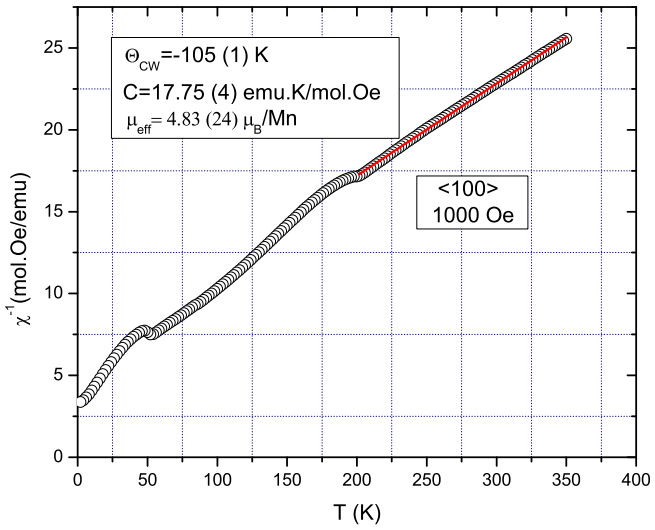

b)

Figure 5.31: a) FC $d(\chi T)/dT$ vs. T plot from the data with the field applied along the $< 100 >$ direction identifying the transition temperatures of $Ni_{16}Mn_6Si_7$. b) A Curie-Weiss fit on the inverse susceptibility data single crystals along the $< 100 >$ above 200 K.

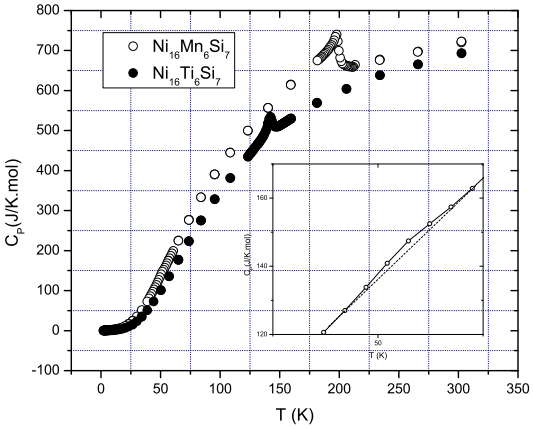

a)

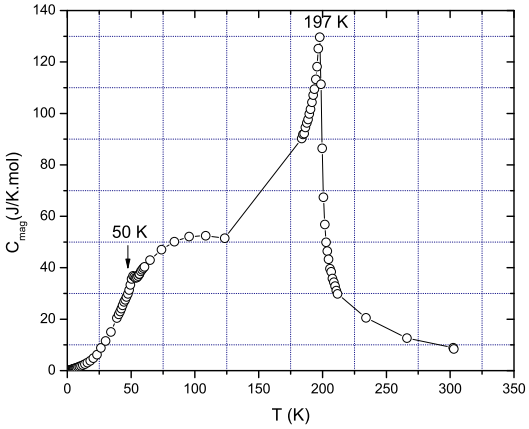

b)

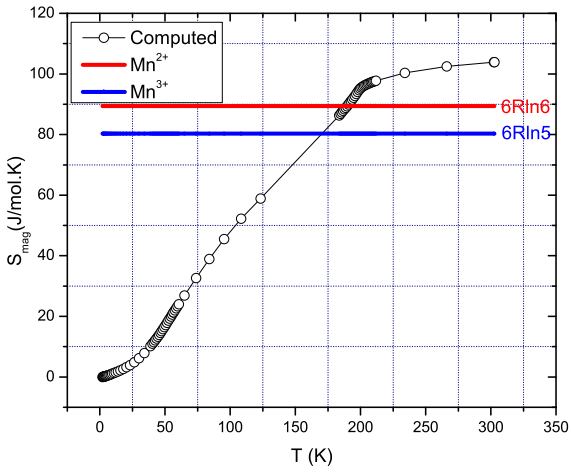

c)

Figure 5.32: a) Zero magnetic field heat capacity of $Ni_{16}Mn_6Si_7$ (open circles) and the lattice match compound $Ni_{16}Ti_6Si_7$ (closed circles) from 2 K to 300 K. $Ni_{16}Mn_6Si_7$ shows a weak transition at 50 K, which is magnified in the inset and a sharp antiferromagnetic to paramagnetic transition at 198 K. $Ni_{16}Ti_6Si_7$ also undergoes a transition at 142 K. b) Magnetic contribution, C_{mag} for $Ni_{16}Mn_6Si_7$ as function of temperature. The magnetic contribution, C_{mag} is obtained by direct substraction of the data from the lattice match compound $Ni_{16}Ti_6Si_7$ ignoring the phase transition. c) Entropy, S_{mag} over the whole temperature range (2 K -302 K) is compared with $6Rln6$ for $S = \frac{5}{2}$ Mn^{2+} and $6Rln5$ for $S = 2$ Mn^{3+}.

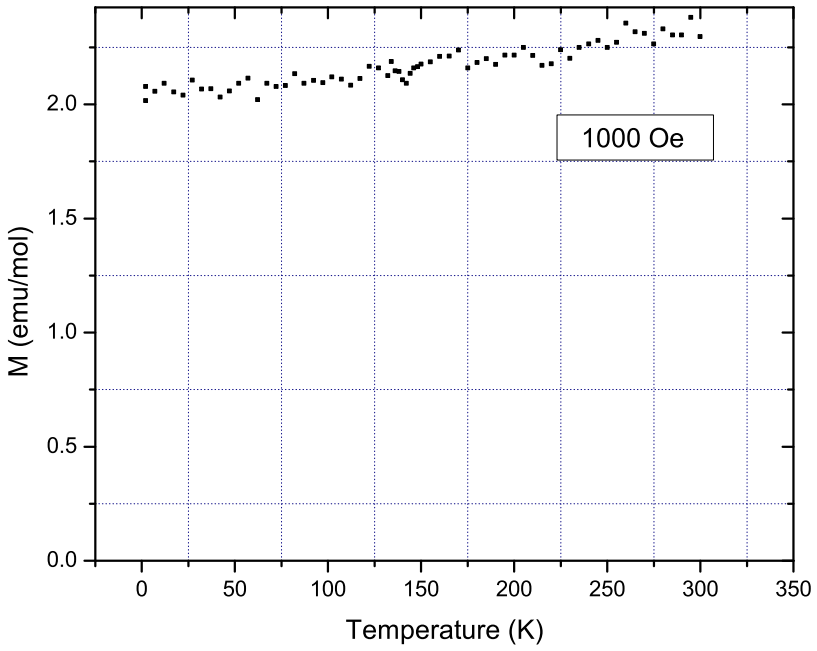

Figure 5.33: ZFC magnetic susceptibility of $Ni_{16}Ti_6Si_7$ under a constant magnetic field of 1000 Oe.

103.9 at J/mol.K which exceeds reasonable values for this material, assuming that Mn is the only magnetic atom. The data of Holman et al. [68] seem to confirm that there is no ordered moment on the Ni sites in this class of materials. The discrepancy might then be attributed to the choice of $Ni_{16}Ti_6Si_7$ as a lattice match which apparently underestimates the lattice contribution in $Ni_{16}Mn_6Si_7$.

5.2.3 Neutron diffraction

Neutron diffraction data were obtained on a polycrystalline powder sample at 298 K, 100 K and 4 K corresponding to the three different regimes of magnetic susceptibility and heat capacity behaviour. As indicated by magnetic measurement, at room temperature the structure was refined to be a paramagnetic type with no additional magnetic contribution (Fig. 5.34a). The room temperature structure was refined by the Rietveld method (Fig. 5.34a), and the structural parameters are listed in Table 5.13. The structural parameters were found to be in excellent agreement with previously reported results for $Ni_{16}Mn_6Si_7$ [2, 109, 167]. It should be mentioned that the occupancy of individual elements is kept constant during the refinement. The Mn atoms occupy the sites of regular octahedra which are not directly connected with other octahedra. Each Mn atom within an octahedron is coupled with four nearest neighbours by exchange constant J_1, one next nearest neighbour by J_2 and with four neighbours of the adjacent octahedra by J_3, as shown in figure 5.35. The J_1, J_2 and J_3 pathway lengths are 0.279 a, 0.393 a and 0.429 a, respectively, where a is the lattice constant.

The neutron diffraction data collected at 100 K show new reflections, relative to room

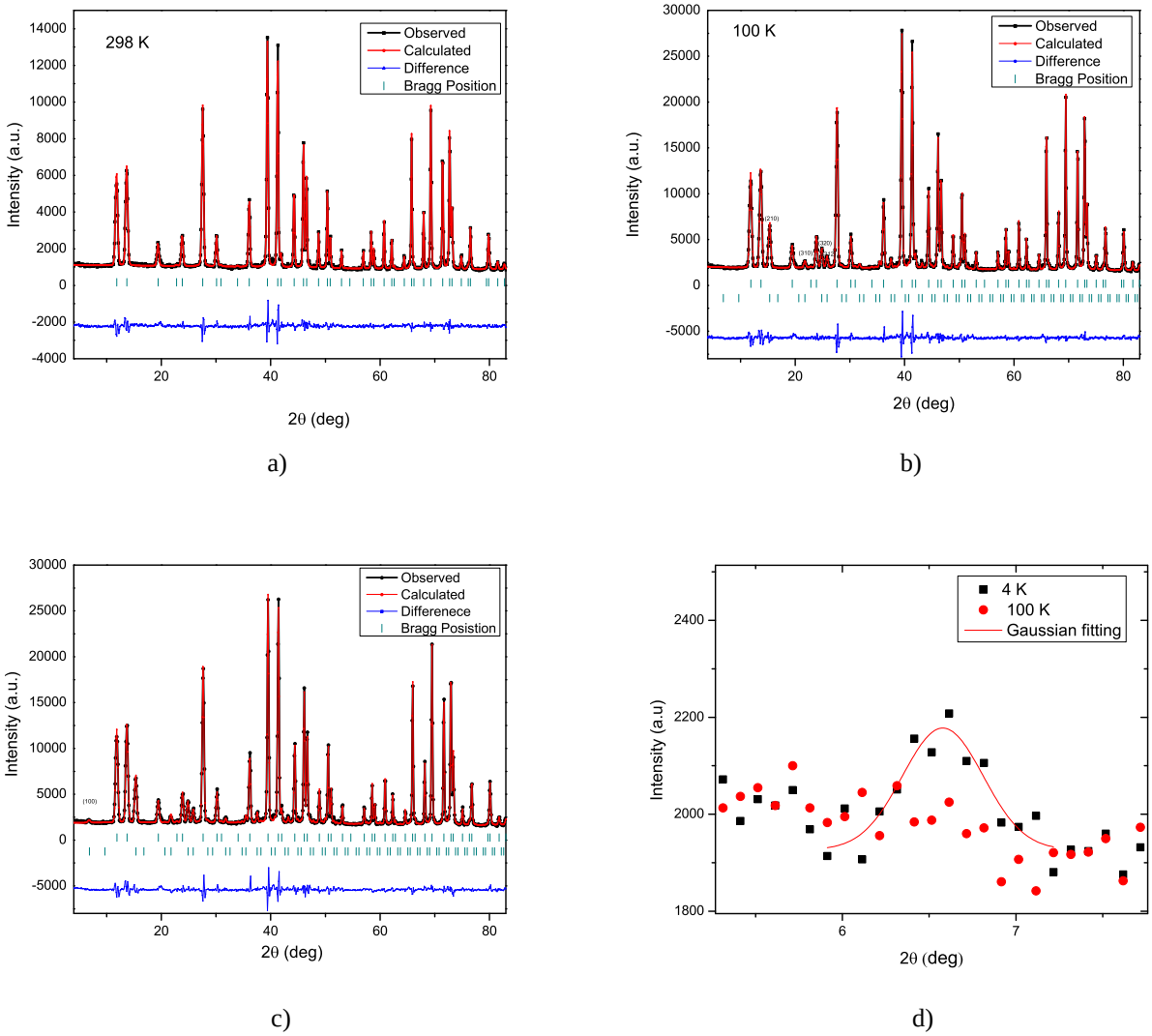

Figure 5.34: Rietveld refinement profile of $Ni_{16}Mn_6Si_7$ a) 298 K, b) 100 K and c) 4 K. (d) A comparison of 4 K and 100 K neutron data at low 2θ showing (100) peak at 4 K.

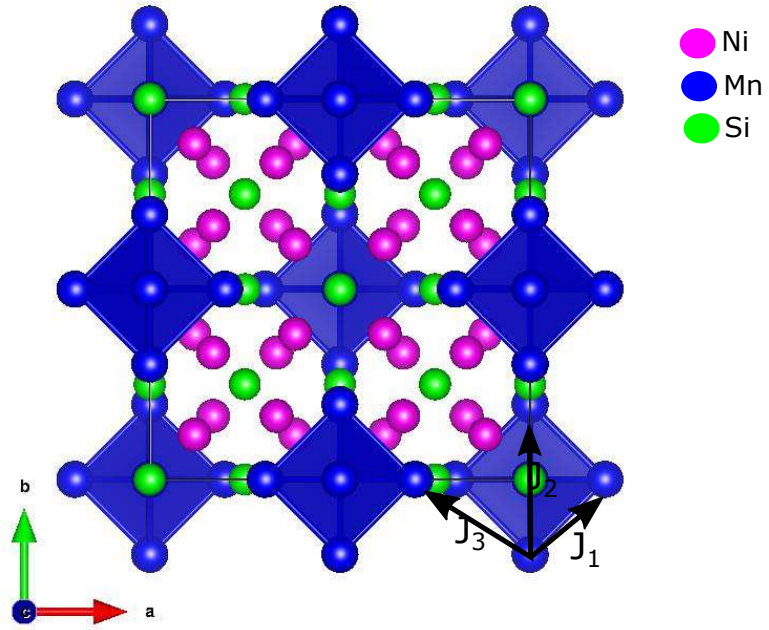

Figure 5.35: Refined crystal structure of $Ni_{16}Mn_6Si_7$ in paramagnetic state. In the structure Mn ions are connected by $4J_1$, $1J_2$ and $4J_3$ bonds.

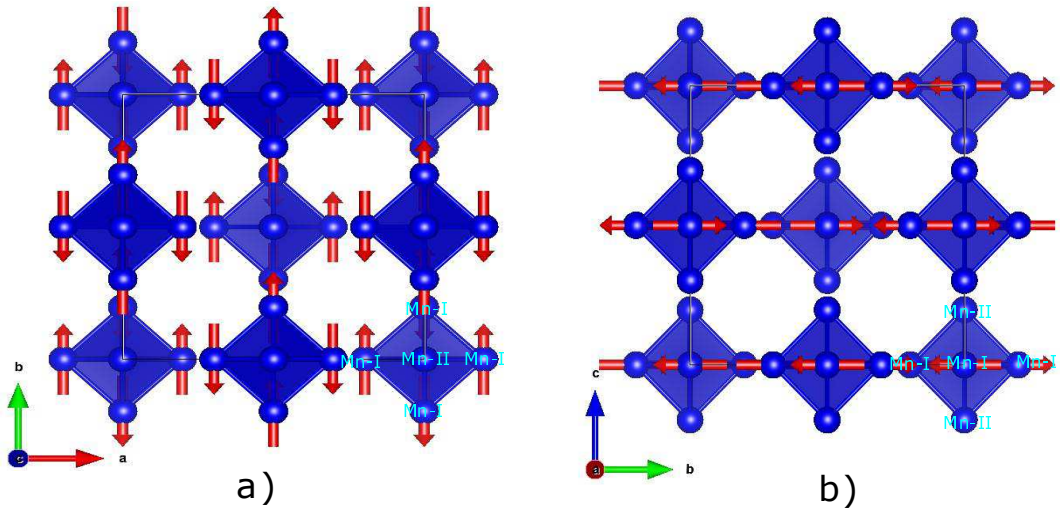

Figure 5.36: Magnetic structure of $Ni_{16}Mn_6Si_7$ at 100 K showing a two-dimensional (2D) magnetic arrangement magnetic moments between Mn-I ions (parallel to (ab) plane in the current coordinate system). Mn-II ions remain frustrated. The structures shown in the figure represent projection along the (ab) and b) (bc) planes, respectively.

Table 5.8: Refined structure parameters for $Ni_{16}Mn_6Si_7$

Temperature	298 K	100 K	4 K
Lattice constant($\mathring{A}$)	11.1497(4)	11.1238(3)	11.1198(4)
Spacegroup	$Fm\bar{3}m$	$Fm\bar{3}m$	$Fm\bar{3}m$
Magnetic phase	Paramagnetic	Antiferromagnetic	Canted Antiferromagnetic
Mn; 24e(x, 1/2, 1/2)	0.6969(3)	0.6969(3)	0.6969(3)
B(Mn) ($\mathring{A}^2$)	0.49(15)	0.32(14)	0.09(5)
M(Mn-I)(μ_B)	-	4.45(5)	4.74(11)
M(Mn-II)(μ_B)	-	0	0.65(24)
Ni1; 32f(x, x, x)	0.33322(11)	0.33322(11)	0.33322(11)
B(Ni1) ($\mathring{A}^2$)	0.58(5)	0.36(5)	0.22(5)
M(Ni1)(μ_B)	-	0	0
Ni2; 32f(x, x, x)	0.11780(12)	0.11780(12)	0.11780(12)
B(Ni2) ($\mathring{A}^2$)	0.58(5)	0.49(5)	0.36(5)
M(Ni2)(μ_B)	-	0	0
Si1; 4a(1/2, 1/2, 0)	-	-	-
B(Si1) ($\mathring{A}^2$)	0.48(10)	0.74(27)	0.66(28)
Si2; 24e(1/2, 1/4, 1/4)	-	-	-
B(Si2) ($\mathring{A}^2$)	0.48(10)	0.35(10)	0.34(10)
χ^2	5.33	9.66	10.4
R_{wp}	11.4	10.3	10.7
R_F	2.51	1.66	1.94
R_{mag}	-	8.81	8.06

temperature, which can be indexed as (210), (310), (320) and (312), which are systematically absent in Fm-3m symmetry and can thus be associated with magnetic ordering . These same reflections were reported by Kolenda et al. [2].

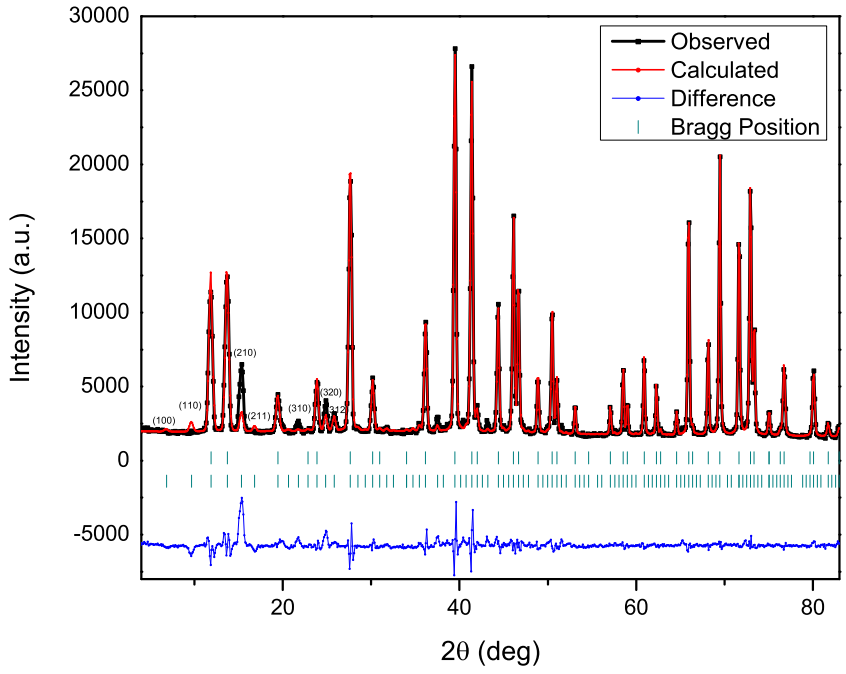

Figure 5.37: Refinement profile of $Ni_{16}Mn_6Si_7$ with the magnetic structure model proposed by Kolenda et al. [2]

The solution of the magnetic structure was based on the representation analysis method using SARAh [140]. For the ordering, wave vector k = (0 0 1) four basis vectors Γ_2, Γ_3, Γ_9 and Γ_{10} resulted from this approach. The best refinement was obtained using Γ_9 (refinement parameters for all Γ configurations are listed in SI-table I). The Rietveld refinement profile is shown in Fig. 5.34b, and magnetic moments are listed in table 5.13. The resulting magnetic structure (Fig. 5.36) shows a 2D antiferromagnetic configuration of Mn^{2+} atoms involving only four of the six sites on the Mn_6 octahedron oriented along (100) directions

Table 5.9: Magnetic refinement of $Ni_{16}Mn_6Si_7$ at 100 K for different Γ configurations

Configurations	R_{mag}	χ^2	R_{wp}
Γ_2	21.18	11.4	11.4
Γ_3	52.24	20.6	15.3
Γ_9	8.81	9.66	10.3
Γ_{10}	97.08	35.6	20.2
Previously published [2]	62.95	23.9	16.5

in an ab plane. Here, Mn occupancy is separated into 2 Mn sublattices, Mn-I and Mn-II. Mn-I contain chains of atoms on a principal plane arranged antiferromagnetically with the nearest neighbour atoms. Mn-III atoms lie on top and bottom of the Mn-I chains and remain paramagnetic providing evidence of spin frustration within each octahedron. It can be seen that two of four J_1 Mn are coupled antiferromagnetically while the remaining two remain paramagnetic. Mn atoms connected by J_2 are coupled ferromagnetically as would be required given dominant nearest neighbour antiferromagnetic exchange. It can also be noticed that two-dimensional planes formed by the ordered Mn ions are coupled antiferromagnetically with each other indicating strong antiferromagnetism in $Ni_{16}Mn_6Si_7$. The Mn-I moments were refined to be 4.45 (5) μ_B per Mn ion. It can be seen that the moment is close to the theoretical and experimentally reported value for Mn^{2+}, i.e., 5 μ_B (with g=2 and $S = \frac{5}{2}$) and 4.7 μ_B [3], respectively. The moment for the Nickel ions were refined to be 0 to within 2σ. It can be seen that our model is different from the one proposed by Kolenda et al. [2]. Refinement of the 100 K data using their proposed magnetic structure showed relatively poor agreement with the observed powder pattern (The Rietveld profile is shown in Fig. 5.37 and the obtained refinement parameters are listed in table 5.9). On the other hand, our model of Fig. 5.36, with frustrated Mn spins is consistent with the observed bulk susceptibility data which shows a paramagnetic like contribution persisting below T_N = 198 K.

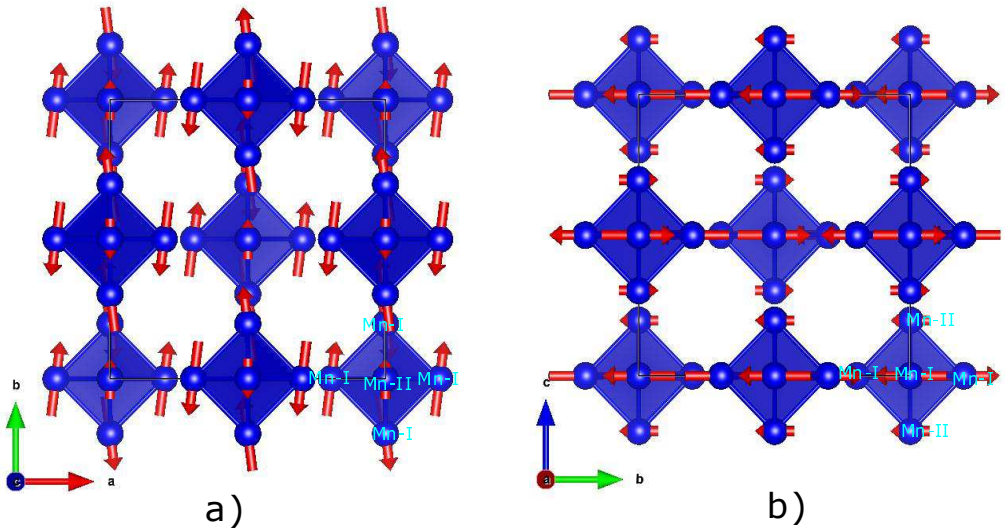

Figure 5.38: A hidden spin canted antiferromagnetic structure is favored for $Ni_{16}Mn_6Si_7$ at 4K. The two dimensional magnetic symmetry is broken and the moments are canted in (ab) plane. Magnetic moment vectors are guide to eye only. The structures presented in the figure corresponds to projection along the (ab) and b) (bc) planes, respectively.

A careful comparison of neutron diffraction at 4 K and 100 K revealed an extra (100) peak at 4 K (Fig. 5.34d). The presence of such a reflection implies the magnetic moments cannot be parallel to (100) directions. Consequently, it can be presumed that the 2D antiferromagnetic symmetry is broken. This result can be associated with phase transition at 50 K. The refinement showed that the Mn-I moment value at 4 K is increased slightly to 4.74(11) μ_B and that the spins make a canting angle with respect to (100) of $9(1)^0$ (Fig. 5.38). This is sometimes called hidden spin canting which refers to configuration where the moments are canted about the axis but still in a collinear arrangement [100]. Note that, the moments are still consistent with values for the $S = \frac{5}{2}$ system [3]. As well, a small moment of 0.65(24) μ_B appears on the Mn-II site which may be real. Note that even below 50K, the model predicts a high concentration of paramagnetic spins which is consistent with the bulk susceptibility which continues to increase to lower temperatures. The relevant refinement

parameters are shown in Table 5.13 and the Rietveld profile is shown in Fig. 5.34c.

5.2.4 Low field temperature dependence of DC magnetization

To examine the thermal variations of the canting strength in $Ni_{16}Mn_6Si_7$, we have analyzed the temperature dependence of magnetization in three low order crystallographic directions of the crystal. An accurate estimation requires the magnetic field to be small enough not to dominate the magnetic spin and yet to be strong enough to produce a magnetic signal. In this study, the temperature dependence of magnetization was measured in a 50 Oe magnetic field applied in $< 100 >$, $< 110 >$ and $< 111 >$ direction, respectively.

The zero-field cooled measurement (Fig. 5.39) showed that the magnetic susceptibility follows the trend $\chi_{111} > \chi_{100} > \chi_{110}$ until 20 K where they converge, and the order reverses ($\chi_{111} < \chi_{100} < \chi_{110}$). Consistent behavior was observed in the field cooled magnetic susceptibility data (inset in Fig. 5.39). A higher χ_{111} below 20 K suggests the ferromagnetic interaction to be stronger in that direction indicating that the net ferromagnetic moment caused by the canting is lying along that direction. The lowest χ_{110} value below 20 K indicates that the antiferromagnetic interaction is stronger in $< 110 >$ at low temperatures. As the temperature increases, the strength of ferromagnetic moments gets weaker with a large drop (evident by the large drop in χ_{111}) in magnetization and antiferromagnetic interaction becomes stronger. It should be noted that the magnetic susceptibility data presented above also includes the contribution from of paramagnetic contribution due to frustration. Note that, even above 50 K, the $< 100 >$ and $< 110 >$ magnetic susceptibilities do not converge indicating the presence of an additional ferromagnetic phase. In contrast with the ZFC-FC data in Fig. 5.30, Fig. 5.39 suggests that above 50 K the ferromagnetic phase is extremely weak, originating from a slight non-collinear or normal spin canting, with the moments

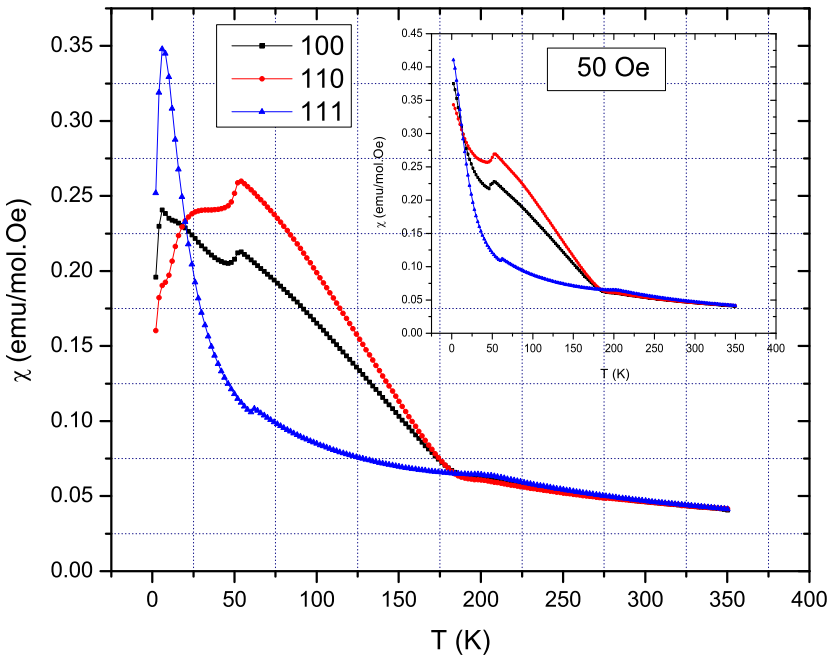

Figure 5.39: ZFC magnetization of $Ni_{16}Mn_6Si_7$ as a function of temperature. A constant magnetic field of 50 Oe is applied in $< 100 >$, $< 110 >$ and $< 111 >$ directions to examine the changes in canting angle with the temperature. Inset shows data for the FC measurements that showed a similar dependence.

getting slightly canted with respect to each other. Detection of such weak phenomenon is beyond the limit of the detectors without a magnetic field. Consequently, it was not observed in the neutron diffraction data. Additionally, it can also be seen that the sudden drop of ZFC susceptibility below 6 K is also evident in the 50 Oe data in Fig. 5.39. Since the system contains a higher concentration of paramagnetic Mn ion, freezing these weak moments that can result in the rapid drop of ZFC magnetization below 6 K, is quite possible. Such a weak phenomenon, however, can not be detected by the neutron diffraction experiment.

5.2.5 Field dependence of DC magnetization

The DC magnetization was measured with the magnetic field applied in $< 100 >$, $< 110 >$ and $< 111 >$ directions of the crystal sample at 2 K, 25 K, 100 K and 298 K that fall to the region of interest pointed by the low field (50 Oe) magnetic susceptibility data. At 2 K, a much stronger ferromagnetic component is expected in $< 111 >$ direction. As the temperature is raised to 25 K, the antiferromagnetic interaction is expected to be dominating the canted moments. At 100 K, a complete antiferromagnetic behavior is to be observed while at 298 K, the compound is paramagnetic.

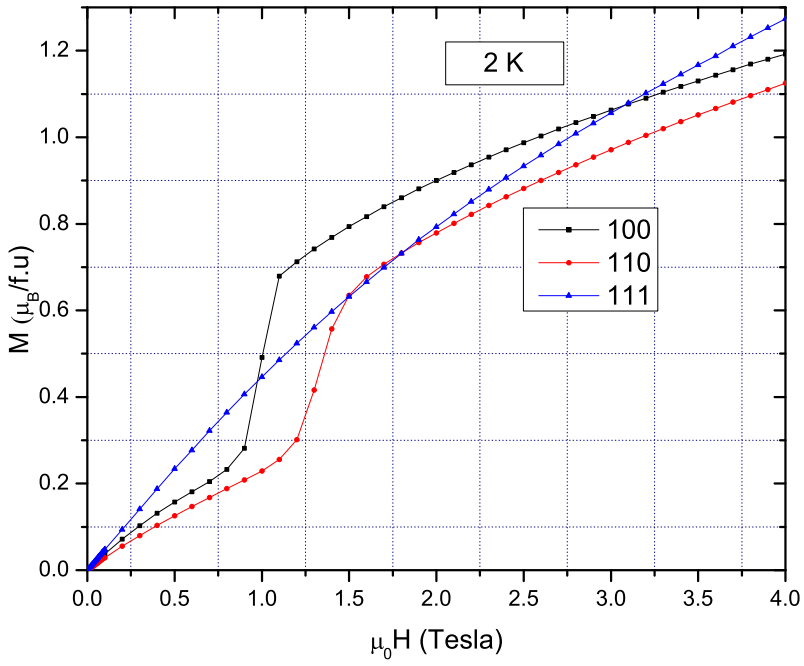

Figure 5.40: ZFC field dependent magnetization behavior of $Ni_{16}Mn_6Si_7$ at 2 K. Magnetic field up to 4 Tesla is applied in $< 100 >$, $< 110 >$ and $< 111 >$ directions.

The magnetization at 2 K (Fig. 5.40) showed a sudden increase in net magnetization

at a critical field of 0.9 Tesla for M_{100} and at 1.2 Tesla for M_{110}. An extrapolation of the data to zero field yielded a positive intercept at $M_{S100} = 0.55\mu_B$, $M_{S110} = 0.35\mu_B$, and $M_{S111} = 0.05\mu_B$, respectively. While a positive intercept confirms a ferromagnetic type behavior, the magnitude of M_S is much smaller compared to the Mn^{2+} spin-only value of $5\mu_B$ per ion. The low M_S value indicates the presence of strong antiferromagnetic coupling between Mn ions that prevent the spins to completely align in the direction of the field. The behavior is consistent with a smeared spin flop type transition to a new magnetic state [3, 168–171]. In this phenomenon, the magnetization of the magnetic sublattices undergoes an abrupt transition in a direction perpendicular to the magnetic field. The nature of the abrupt transition is dependent on the angle, ϕ between the spin axis and the magnetic field. When the field is applied parallel to the spin axis ($\phi = 0^0$), the transition appears as a first-order type transition. However, as the angle becomes non-zero, the spin flop type transition gets smeared [168]. Based on aforementioned, it can be said that ϕ is minimum for M_{100} followed by M_{110}. A very high ϕ angle for M_{111} causes the disappearance of the sharp transition, and the magnetization rotates gradually with the applied field. Nevertheless, because of a strong net ferromagnetic moment in $< 111 >$ direction, the magnetization is higher in that direction. It can also be noted that even at the higher magnetic field induced phase the M_{110} value is still the lowest hinting towards the stronger antiferromagnetic interaction along that direction.

The hysteresis behavior for $< 100 >$ orientation at 2 K (Fig. 5.41a) shows the transition to be an irreversible type, and a persistent ferromagnetic behavior is observed. Such a response indicate that during the spin flop transition, the magnetic moments is oriented in a stable configuration which can not be reversed even when the field is removed. The

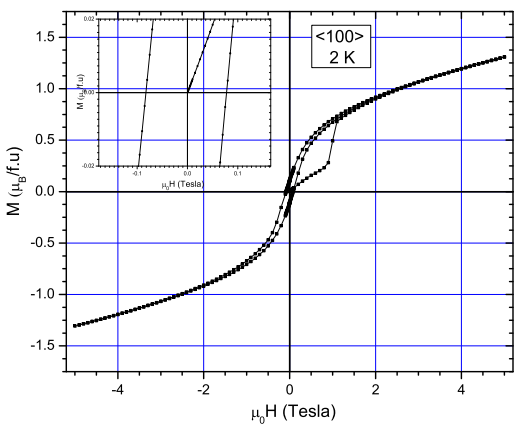

a)

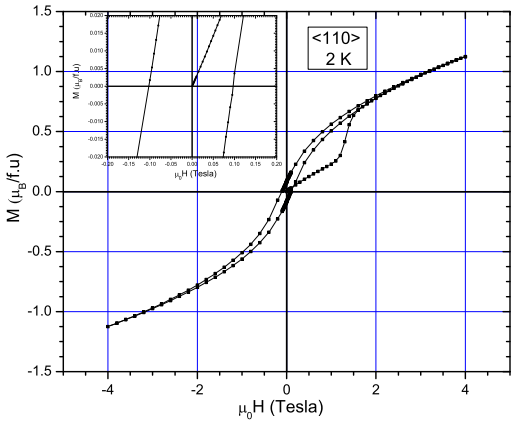

b)

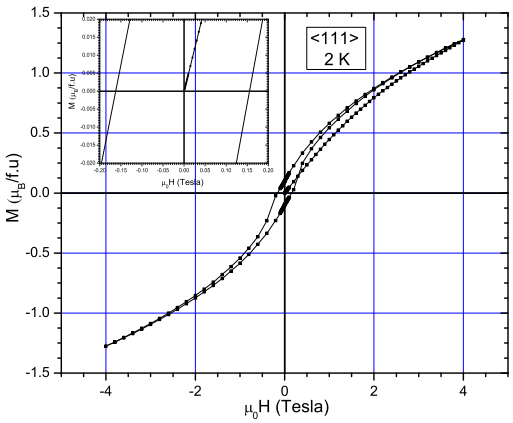

c)

Figure 5.41: ZFC DC hysteresis of $Ni_{16}Mn_6Si_7$ at 2 K as function of magnetic applied field in a)$< 100 >$ b)$< 110 >$ and c)$< 111 >$ directions, respectively. The $< 100 >$ measurement was done with a maximum field upto 5 Tesla.

behavior is significantly different from the other spin-flop type transition reported for the canted antiferromagnetic systems [14, 100]. The coercive field H_{C100} is found to be 0.095 Tesla. The hysteresis measurement for $< 100 >$ orientation is done with an applied field up to 5 Tesla. Since no observable change is detected at the high magnetic field, the rest of the hysteresis measurement is conducted with the field up to 4 Tesla. Hysteresis in $< 110 >$ (Fig. 5.41b) and $< 111 >$ (Fig. 5.41c) direction shows a similar type of behavior with the coercivity for $< 110 >$ direction being H_{C110} =0.095 Tesla and a H_{C110}= 0.012 Tesla for $< 111 >$ direction.

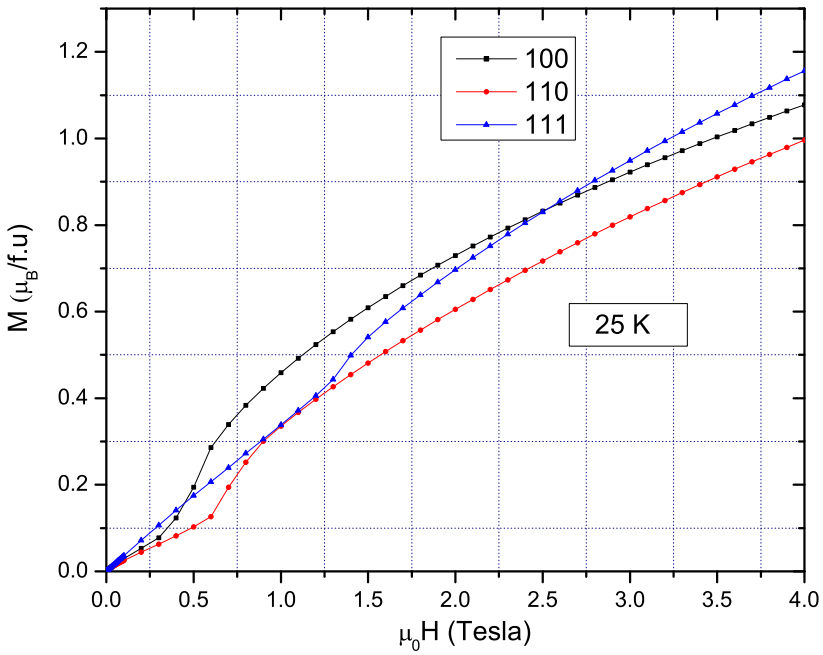

Figure 5.42: ZFC field dependent magnetization behavior of $Ni_{16}Mn_6Si_7$ at 25 K. Magnetic field up to 4 Tesla is applied in $< 100 >$, $< 110 >$ and $< 111 >$ directions. Inset shows stronger/weaker magnetization reversal at 0.04 Tesla magnetic field.

Subsequent field dependent magnetization measurements conducted at 25 K (Fig. 5.42) shows the weakest magnetization in $< 110 >$ direction and strongest magnetization in $< 111 >$ at higher fields which was observed otherwise in the 50 Oe temperature dependent data (Fig. 5.39). It can be seen in the inset of Fig. 5.42 that this stronger magnetization reversal occurs at a field of 0.04 Tesla due to different magnetic field response of antiferromagnetic and ferromagnetic interaction. The magnetization data also reveals a smeared spin-flop type transition in three, $< 100 >$, $< 110 >$ and $< 111 >$ directions. The transitions occur at much smaller critical fields of $H_{SF100} =$ 0.4 Tesla, $H_{SF110} =$ 0.6 Tesla and $H_{SF111} =$ 1.3 Tesla. The extrapolated intercept of magnetization is also found to be smaller ($M_{S100} = 0.075\mu_B$, $M_{S110} = 0.065\mu_B$, and $M_{S111} = 0.04\mu_B$, respectively). This indicates a weakening of the ferromagnetic behavior and dominance of the antiferromagnetism. Such a behavior can be attributed to the effect of temperature. As discussed in the previous section, with increasing temperature the canting angle gets smaller, and the antiferromagnetic interaction becomes dominating. Contrary to the low field susceptibility data, magnetization at a higher field is maximum for M_{111}. Search at the low field region reveal the field to be 0.008 Tesla (80 Oe) where M_{100}, M_{111} and M_{110} reverses. This is due to the different responsive behavior of a ferromagnetic and antiferromagnetic material under magnetic field. At 25 K, a weak nonetheless ferromagnetic moment exists in $< 111 >$ direction whereas a strong antiferromagnetic interaction is present along $< 110 >$. Since ferromagnetic moment is more responsive to the applied magnetic field, the magnetization increases faster in $< 111 >$ direction. Whereas, a strong antiferromagnetic interaction in $< 110 >$ direction tend to oppose the magnetic field and the magnetization increases slowly.

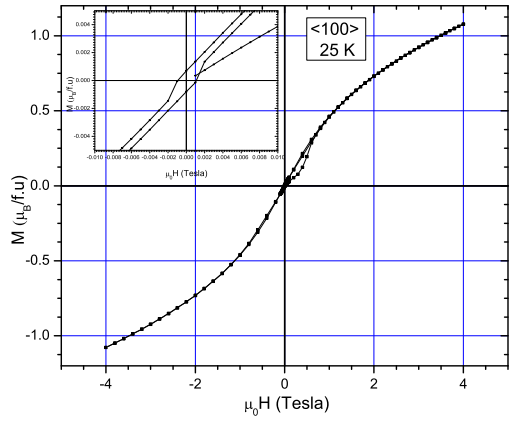

a)

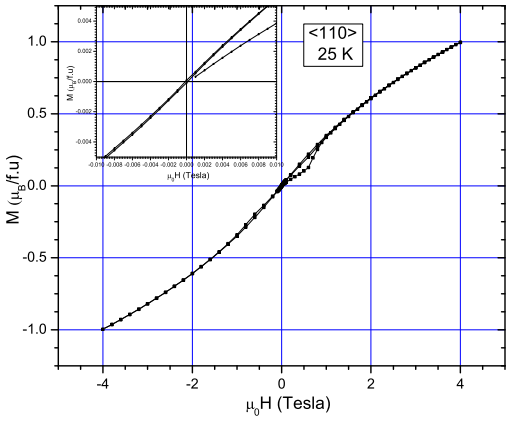

b)

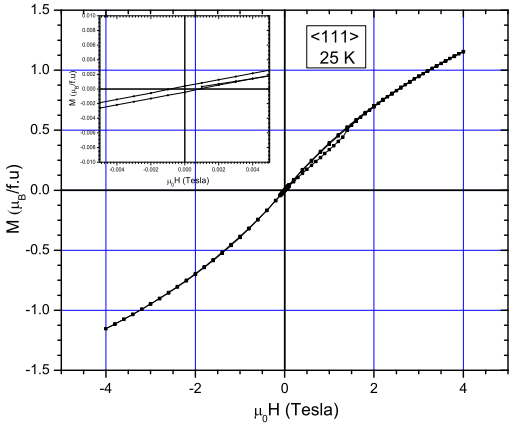

c)

Figure 5.43: ZFC DC hysteresis for $Ni_{16}Mn_6Si_7$ at 25 K measured as function of magnetic applied field in a) $< 100 >$ b) $< 110 >$ and c) $< 111 >$ directions, respectively.

The hysteresis behaviour at 25 K shows a narrowing of the hysteresis loop at the low field region (Fig. 5.43). Such behaviour can be described as a weak ferromagnetic behaviour determined by the dominance of antiferromagnetic interactions. Nevertheless, the compound exhibits a positive coercive field values of H_{C100}=0.001 Tesla, H_{C100}= 0.0003 Tesla and H_{C100}= 0.0012 Tesla at 25 K.

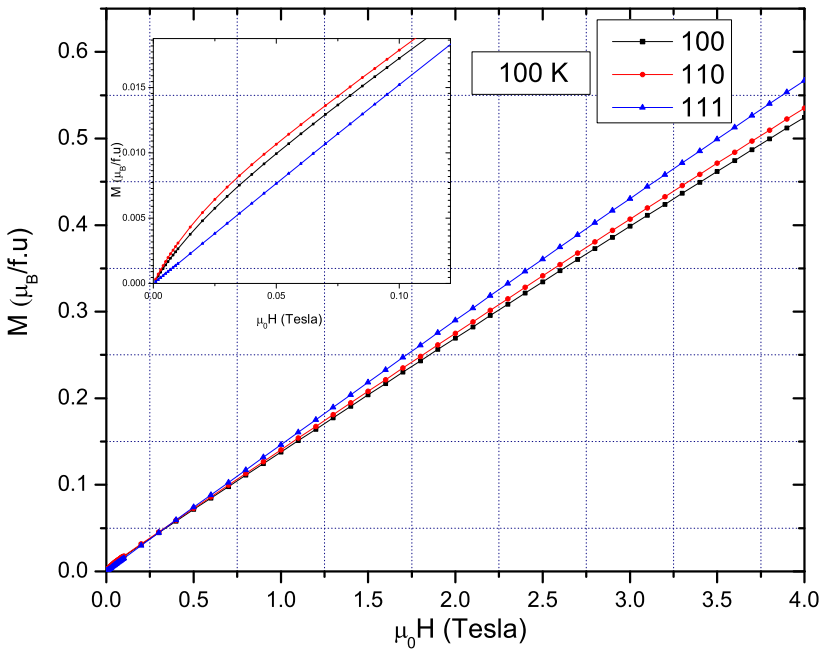

Figure 5.44: ZFC field dependent magnetization behavior of $Ni_{16}Mn_6Si_7$ at 100 K. Magnetic field upto 4 Tesla (40000 Oe)is applied in $< 100 >$, $< 110 >$ and $< 111 >$ direction.

From the analysis of neutron diffraction and low field susceptibility data, the Mn ion spins are nearly (due to slight normal canting) parallel to each other at 100 K. The antiferromagnetic interaction is the highest for such a configuration of spins. Magnetization data at 100 K showed linear dependence at higher field (Fig. 5.44). This is due to a maximum

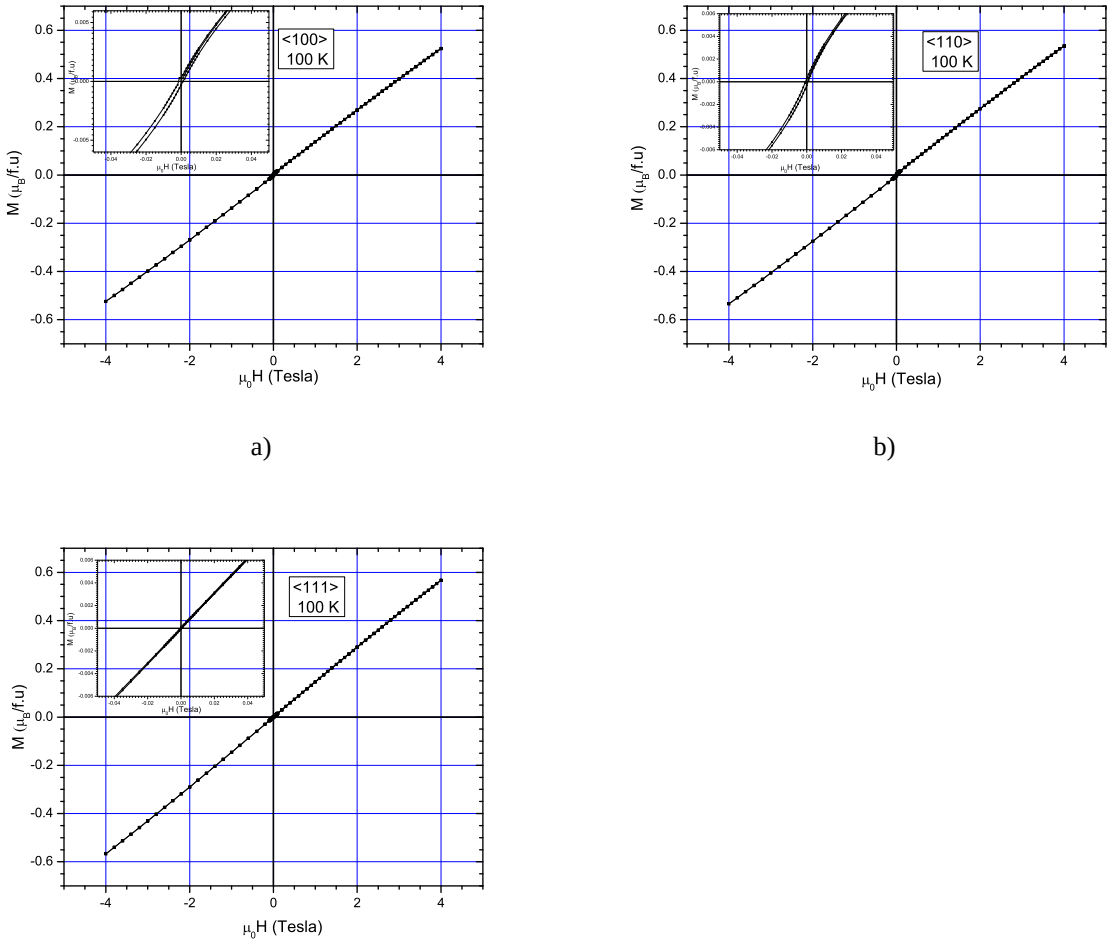

Figure 5.45: ZFC DC hysteresis for $Ni_{16}Mn_6Si_7$ at 100 K measured as function of magnetic applied field in a) $< 100 >$ b) $< 110 >$ and c) $< 111 >$ directions, respectively. Inset shows a small ferromagnetic contribution from slight non-collinear or normal canting of moments

antiferromagnetic exchange interaction for this material. However, as discussed earlier, a very weak ferromagnetism is present above 50 K due to a slight non-collinear canting of moments with respect to each other which was also detected in the 100 K magnetization data at smaller fields (inset in Fig. 5.44). Consequently, a very small $M_{S110} = 0.0025\mu_B$, $M_{S100} = 0.0021\mu_B$, was observed. The M_{111} on the other hand, was found to be linearly dependent on the magnetic field. Such behavior of M_{111} is not surprising as it is an indication that magnetic field is applied nearly perpendicular to the weakly canted spins. The hysteresis measurement reveals a tiny hysteresis in $< 110 >$ and $< 100 >$ direction and a paramagnetic dependence in $< 111 >$ direction (Fig. 5.45).

A paramagnetic behavior is observed at 298K, as shown in Fig. 5.46.

5.2.6 Discussion

The observation of the magnetic susceptibility and heat capacity data suggesting a paramagnetic ordering above 197 K is reflected well in the neutron refinement at 298 K where no magnetic ordering of the $Ni_{16}Mn_6Si_7$ system was observed. The magnetic structure obtained in the 100 K refinement found Mn-II ions to be remaining as paramagnetic, while Mn-I atoms are antiferromagnetically coupled suggesting the system be a 2D geometrically frustrated antiferromagnet. The configuration can be related to the magnetic susceptibility data from 197 K to 50 K. Although negative Θ_{CW}, the Curie-Weiss fitting of the inverse susceptibility confirmed the system to be antiferromagnetic below 197 K, the magnetic susceptibility data showed to be consisting a paramagnetic contribution too that can be explained in terms of geometrically frustrated Mn-II atoms. The refinement at 4 K showed the breaking of the two dimensional symmetry yielding a hidden spin-canted magnetic

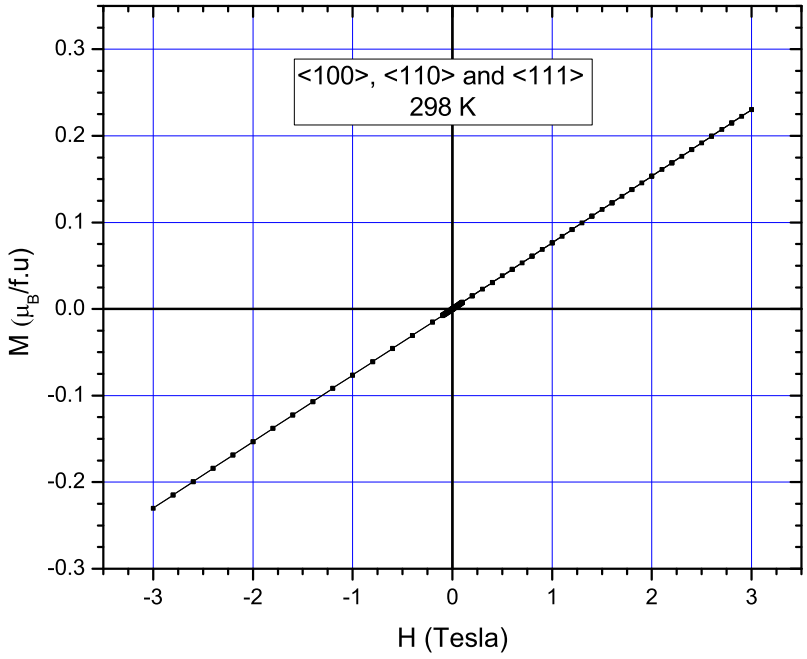

Figure 5.46: ZFC magnetic hysteresis of $Ni_{16}Mn_6Si_7$ at 298 K. A paramagnetic state is observed for the applied field in all directions

.

configuration. Such a system is known to give rise to a ferromagnetic moment that can be connected to the magnetic transition at 50 K. The ZFC-FC magnetic measurement in Section 5.2.1 provided evidence of a ferromagnetic component where the magnetization decreases rapidly till 50 K with increasing temperature along with an evident splitting between ZFC and FC measurements. As a result, it can be assumed that the below 50 K the system undergoes a transition from the 2D frustrated antiferromagnetic state to the hidden spin canted state. Note that, there the system also undergoes another phase transition below 6 K that was mentioned due to the spin freezing effect. Although the refinement at 4 K found the Mn-II to be ordering with small moments, the system still contains a higher concentration of paramagnetic Mn ion. Freezing of these weak moments that can result in the rapid drop of ZFC magnetization below 6 K, is quite possible. Such a weak phenomenon, however, can not be detected by the neutron diffraction experiment.

5.3 Short-range ordering and physical properties of the Ni-Mn-Si based Laves phase Mn($Ni_{0.6}Si_{0.4}$)$_2$

5.3.1 Single crystal diffraction

The refined structural and the atomic parameters of Mn($Ni_{0.6}Si_{0.4}$)$_2$ compound are listed in table 5.10 and table 5.11, respectively which were found to be in good accordance with the previously published results on a slightly different composition [83]. The crystal structure was solved in a $MgZn_2$-type structure (C14 laves phase) in the $P63/mmc$ spacegroup. Best refinement was obtained with the atomic parameters such that the Mn atoms occupy the $4f$ crystallographic site while Ni and Si are located on the $2a$ site with 0.471/0.529 fractional

occupancy and $6h$ position with occupancies of 0.66/0.33. The occupancy parameters obtained are consistent with the crystal chemistry of the $MgZn_2$-type C14 laves phase as in these compound it has been observed that the atoms with the largest radius situate at the $4f$ position (Mn in the present case with the largest atomic radius of $1.61\ \mathring{A}$). Also, in the ternary Laves system, the $2a$ and $6h$ occupancies were found to be distributed in a manner that the atoms with the highest concentration prefer to be in the $6h$ site which evident the major occupancy of Ni atoms in the site [84].

Table 5.10: Crystallographic data and refinement parameters for the $Mn(Ni_{0.6}Si_{0.4})_2$ single crystal (Mo K_α radiation, 298K)

Refined composition	Mn4 $Ni_{4.96}Si_{3.04}$
Space group	$P63/mmc$
Lattice constant $(\mathring{A})$	$a = 4.7639(1)$, $b = 4.7639(1)$ $c = 7.4967(2)$
Volume $(\mathring{A}^3)$	$147.342(7)$
$\rho_{calc}(g/cm^3))$	6.666
Z	4
2θ range	$9.882 - 90.434$
Index ranges	$-8 \leq h \leq 9$,$-9 \leq k \leq 8$ $-14 \leq l \leq -11$
Reflections collected	2373
Independent reflections	$271[R_{int} = 0.0389,\ R_{sigma=0.0232}]$
Data/restraints/parameters	$271/0/13$
Goodness-of-fit on $\lvert F\rvert^2$	1.208
Largest diff. peak/hole (e/$\mathring{A}^3$)	$1.23/-1.18$
R indices $[I >= 2\sigma(I)]$	R_1=0.0222 wR_2 =0.05

Analysis of the three-dimensional reciprocal space using MAX3D [135] revealed triangle shaped diffuse scattering pattern along planes that are parallel to ab which is an indication of short-range ordering (SRO) of atoms within the ab plane. In $Mn(Ni_{0.6}Si_{0.4})_2$, Mn atoms are fully occupied at the $4f$ site and are expected to order periodically. Therefore, it can be assumed that Ni and Si atoms fill the $2a$ and $6h$ positions in a unique short-range pattern that gives rise to the observed pattern. A complex occupancy of atoms in $2a$ and $6h$

Table 5.11: Fractional atomic coordinates, occupancy and isotropic displacement parameters for $Mn(Ni_{0.6}Si_{0.4})_2$ obtained from the single crystal refinement.

Atom	x	y	z	Site	Occupancy	U_{eq} ($\AA^2$)
Mn1	0.3333	0.6667	0.0648(4)	4f	1	0.00720(11)
Ni1	0	0	0	2a	0.471(5)	0.01208(16)
Si1	0	0	0	2a	0.529(5)	0.01208(16)
Ni2	0.82873(3)	0.65746(6)	0.25	6h	0.67(5)	0.00704(9)
Si2	0	0	0.5	6h	0.33(5)	0.00704(9)

has been very well addressed by Kerkau [84]. While there is not an exact model to describe the occupancy, it is expected to give peculiar rise ordering of atoms for the Laves phase.

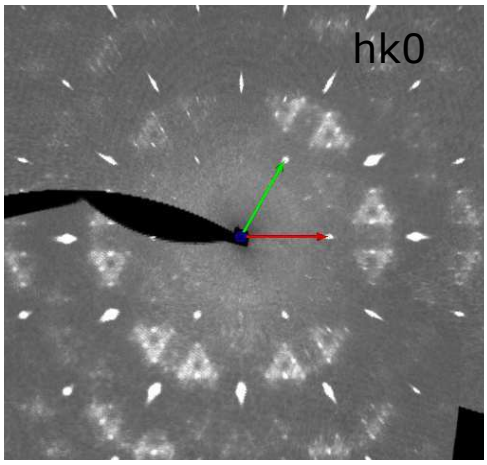

Figure 5.47: Diffraction pattern of $Mn(Ni_{0.6}Si_{0.4})_2$ along (hk0) plane showing triangular shaped diffused scattering patten.

5.3.2 Transmission electron microscopy analysis (HRTEM and EELS)

The high-resolution HAADF-STEM image (Fig. 5.48) of the (0001) surface of $Mn(Ni_{0.6}Si_{0.4})_2$ shows the presence of a distinctive short-range ordering pattern for the compound. It can be noticed that the atomic arrangement within the structure are accommodated in such a

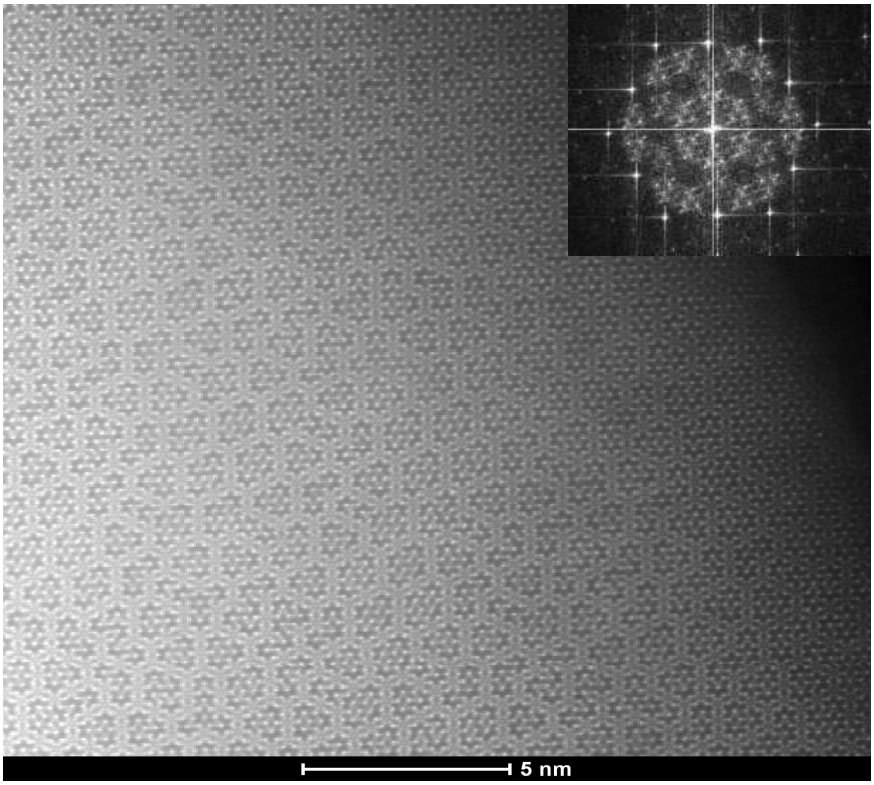

Figure 5.48: HAADF-STEM image of $Mn(Ni_{0.6}Si_{0.4})_2$ (0001) surface showing unique arrangement of the atoms. Inset shows diffused scattering pattern obtained by the fast-fourier transformation (FFT) of the image.

unique manner that several non-periodic units have been formed. These small units of different sizes are arranged randomly to make such a configuration that a single unit cell can not be assigned. The fast-Fourier transformation (FFT) of the image (inset in figure 5.48) demonstrated a diffused scattering pattern similar to that was observed in the single crystal diffraction. Figure 5.49a shows the HAADF-STEM image of the (0001) surface with a higher magnification. The less bright elements can be identified as Si because of their low atomic number of Z=14. Ni and Mn, on the other hand, possess similar atomic numbers of Z=25 and Z=28, respectively. Consequently, the brighter Ni and Mn could not be distinguished in figure 5.49a . To identify the distribution of elements, EELS maps were obtained from the marked cross section of figure 5.49a . Figure 5.49b shows the HAADF signals from the marked area of interest while the elemental map obtained from the region are shown in figure 5.49c-e. The Mn L signal (figure 5.49c) shows a homogenous distribution of the Mn atoms. The effective Mn-Mn distance was determined on the order of $\sim$2.6$\mathring{A}$ which are the horizontal distance between two nearest neighboring Mn atoms in 4f. Consequently, it can be confirmed not only the Mn atoms from the top plane (0001) but the atoms that lie below are also captured in the elemental mapping. Note that, the Mn-Mn distance for the topmost plane is 4.76$\mathring{A}$ (obtained from SCD refinement data). The mapping of Ni atoms 5.49d shows a unique arrangement with the tendency to form a network of three/four/five neighboring atoms. Within the network, the average Ni-Ni nearest neighbor distance of $\sim$4.7$\mathring{A}$ is similar to the lattice constant of 4.7639(1)$\mathring{A}$ confirming that the Ni atoms captured in the mapping are located in the 2a positions. Figure 5.49e shows the elemental maps for the Si atoms which shows that rest of the $2a$ positions are occupied by the Si atoms. Si K signal is not usually detected the in EELS mapping. However, the elemental mapping for Si observed in the present work is due to the use of the powerful

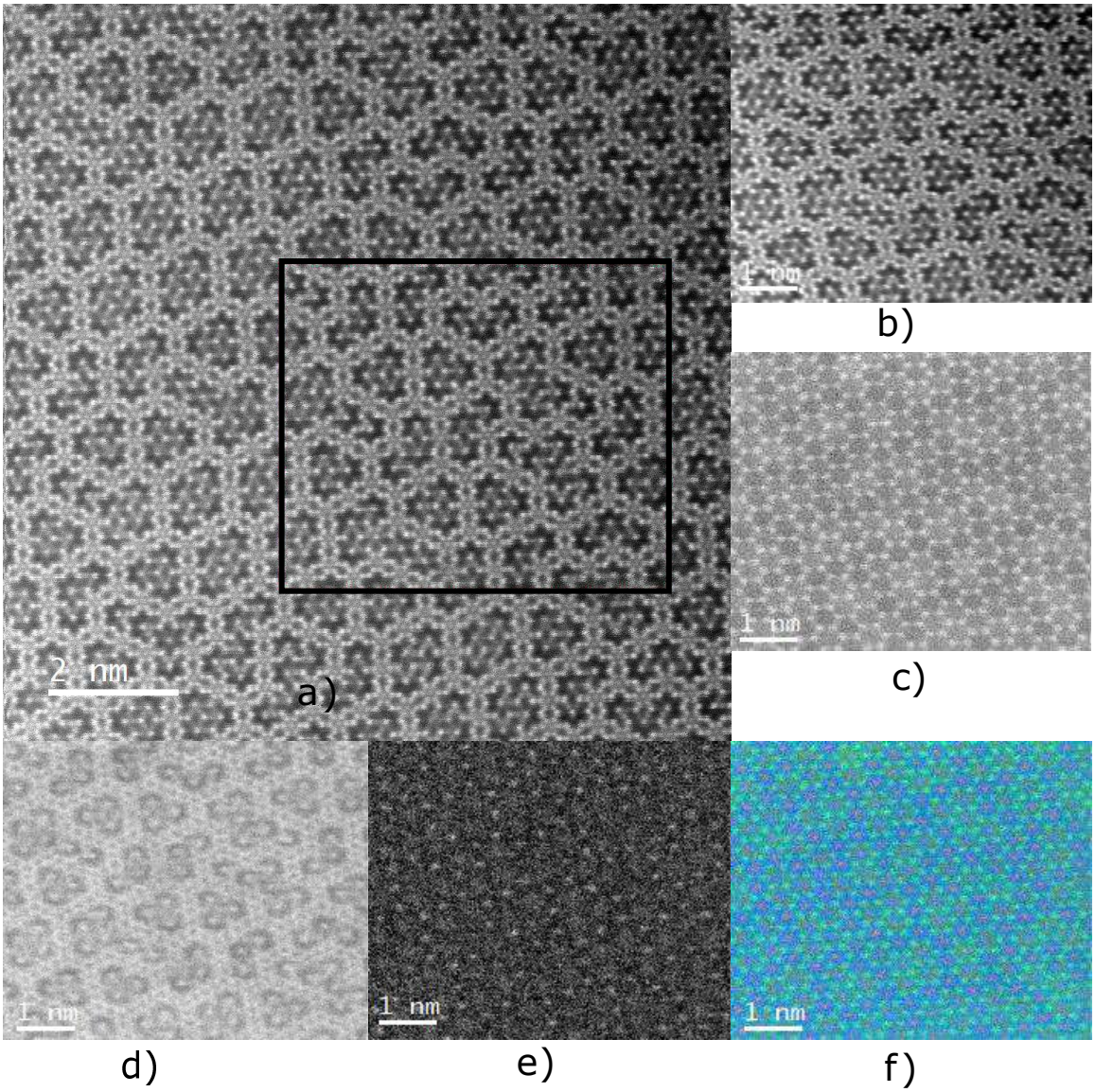

Figure 5.49: a) Higher magnification HAADF-STEM image of the (0001) surface. The box represents area on which EELS data acquisition was done. b) HAADF image of the area of interest acquired in parallel with the EELS mapping. c) Mn L atomic resolution chemical map showing an ordered arrangement of Mn atoms. d) Ni atomic resolution map indicating a distinct non periodic arrangement of the atoms e) 2a Si atomic resolution map capturing the atoms to be located in spaces left by 2a. e) a composite image showing the unique short-range ordering in terms of 2a Ni and Si atoms+ and the Mn atoms located in 4f. Here the Ni atoms are coloured in blue, Si in pink and Mn in green.

Gatan K2 Summit detector [143] that provides unmatched contrast and resolution for all types of molecules. The combined image is shown in figure 5.49a where the Ni atoms are colored in blue, Si in pink and Mn in green. It can be seen that Ni and Si atoms occupy the 2a positions in a unique manner with a Si 2a chain enveloping the network of Ni 2a. The 6h atoms were not observed in EELS which can be due to their close horizontal spacing of $\sim 1\mathring{A}$ that limits the mapping.

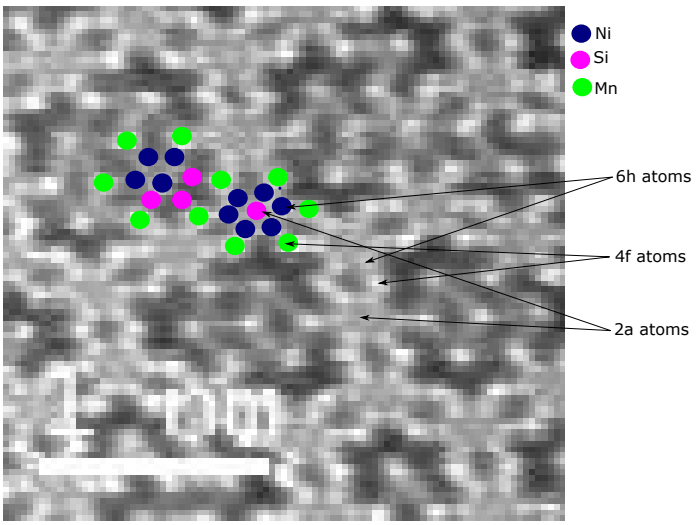

Figure 5.50: a) A magnified section of $Mn(Ni_{0.6}Si_{0.4})_2$ HRTEM image identifying the small tiny dots between the Mn formed hexagons as the Ni 6h atoms. The low scattering Si atoms appears as voids in the 6h positions.

A closer look at the HAADF image (Fig. 5.50) however, shows the presence of the small atoms within the hexagonal unit of Mn that can be identified as the atoms located in the 6h positions. It can be seen that the unit that contains Si in the 2a position (less bright hexagon center) have these small visible atoms in all the 6h position which can be described as the Ni atoms. Weak resolution of 6h Ni atoms compared to half of the lower lying Mn (4f) atoms can again be explained by the close spacing of the atoms in 6h. On the other hand, the unit with Ni in the 2a position contains tiny atoms and empty spaces.

These can be thought to comprise of Ni (tiny atom) and Si (empty space). The 6h Si being invisible is not surprising as these low scattering atoms are lying on a bottom plane with much smaller horizontal spacing between them.

5.3.3 Electrical conductivity measurement

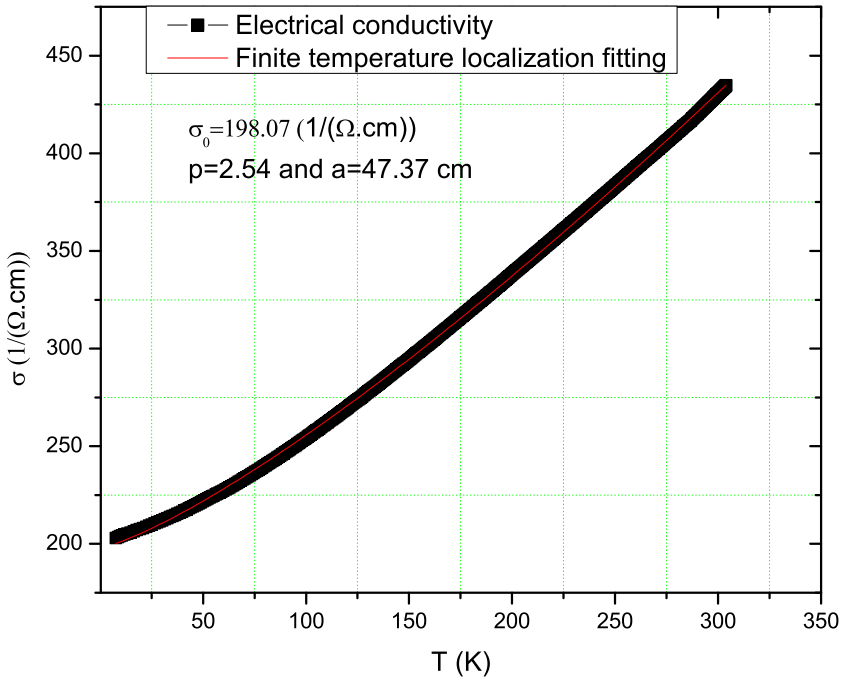

Figure 5.51: Temperature dependence of electrical conductivity of $Mn(Ni_{0.6}Si_{0.4})_2$ from 2 K to 300 K. Data was fitted to the weakening of quantum interference due to random fluctuation.

Yan et al. [83] found the electrical conductivity for the system to be increasing as the temperature increases. Such behaviour is usually an indication of a semiconducting type

system. However, their work confirmed a metallic system for the compound and the electrical conductivity variation with temperature was linked with the localization of conduction electron due to the disorder caused by Ni and Si occupancy. A similar behavior (Fig. 5.51) was also observed in this work. The data were fitted to the three-dimensional temperature dependent electrical conductivity equation for localization [172],

$$\sigma_{3D}(T) = \sigma_0 + \frac{e^2}{\hbar\pi^2}\frac{1}{a}T^{\frac{p}{2}}. \tag{5.28}$$

The fitting yielded the temperature independent conductivity, σ_0=198.07 $\frac{1}{\Omega.cm}$, scattering mechanism index, p=2.54 and a measure of length scale, a=47.37 cm. p and a are related to the length scale of the quantum inference, $L_{th} = aT^{\frac{p}{2}}$. L_{th} is a measure of the weakening of localization by the random fluctuation due to finite temperature. The conductivity data thus provide evidence of localization in the system. The p of 2.54 is an indication of electron-phonon interaction in the system to be a dominant mechanism responsible for limiting the quantum interference [172].

5.3.4 Neutron diffraction

$Mn(Ni_{0.6}Si_{0.4})_2$ possesses a high Néel temperature of $\sim$550 K (will be discussed in a forthcoming section). The inability to collect neutron diffraction data at such a high temperature made it challenging to perform a structure refinement only in the paramagnetic state. Neutron diffraction experiment was carried out in the antiferromagnetic state at 298 K. From the observation of HAADF-TEM, it has been confirmed that the crystal structure of $Mn(Ni_{0.6}Si_{0.4})_2$ cannot be accommodated inside a single hexagonal unit cell. A proper refinement requires considerations of an extended unit cell that is beyond the limitation of a standard refinement software. Consequently, the neutron diffraction refinement in this

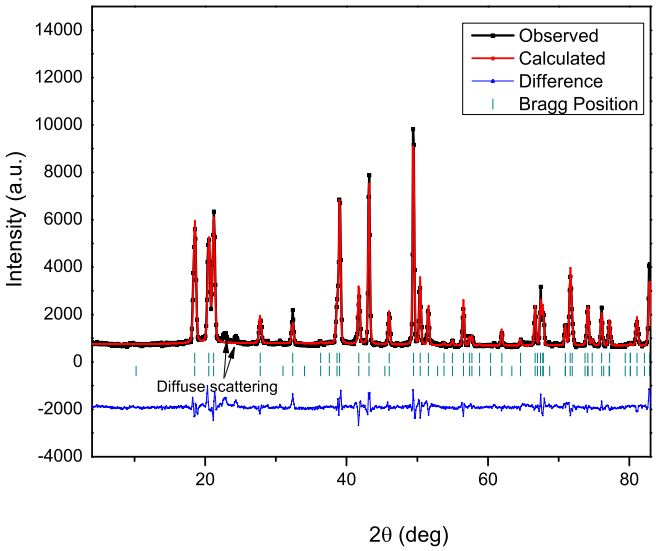

a)

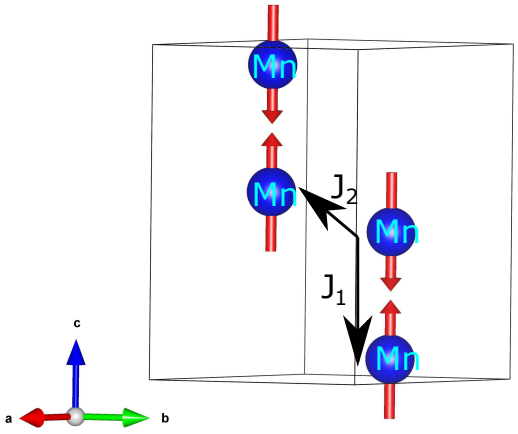

b)

Figure 5.52: a) Rietveld refinement profile of $Mn(Ni_{0.6}Si_{0.4})_2$ at 298 K. b) Magnetic structure of $Mn(Ni_{0.6}Si_{0.4})_2$ displaying the magnetic moments arising only from the antiferromagnetic coupling between Mn atoms.

work was done with a single hexagonal unit cell structure describing average occupancies of the elements which was obtained during the single crystal diffraction. The solution of the magnetic structure was based on the representation analysis approach using the program SARAh [140]. Since no extra magnetic reflections were observed, the wave vector k = (0 0 0) was used for ordering. The method yielded basis vectors Γ_1, Γ_3, Γ_6 Γ_7, Γ_9, Γ_{10}, Γ_{11}, Γ_{12}. The best refinement was obtained with Γ_1 ordering. The refinement profile is shown in figure 5.52a and the structural parameters are listed in table 5.12. The corresponding magnetic structure is presented in figure 5.52b which shows that the magnetism in the system is governed completely by the antiferromagnetic interaction between the Mn atoms. The Mn moment was refined to be 1.52 μ_B/Mn atom which is significantly lower compared to the 2.9 μ_B/Mn obtained by Yan et al. [83]. Note that, the collected neutron diffraction data in figure 5.52a shows some additional peak ear the (1001) reflections which can be identified as diffused scattering peaks due to short-range ordering. The (1001) is also a major magnetic reflection that corresponds to the magnetic moments of Mn. The poor refinement parameters in this work can be attributed to the diffused scattering induced spread of the structural and magnetic peaks which was not taken into account. The magnetic structure of (Fig 5.52b) also shows that both the nearest neighbor and the next nearest neighbor exchange constant, J_1 and J_2 are coupled antiferromagnetically. Therefore, the system is expected to demonstrate strong antiferromagnetism.

5.3.5 Magnetic susceptibility

Figure 5.53a shows the ZFC-FC magnetic susceptibility measured from 300 K to 700 K with an applied field of 1000 Oe. A slight difference between ZFC-FC data was observed that suggests the presence of an impurity ferromagnetic phase in $Mn(Ni_{0.6}Si_{0.4})_2$ along

Table 5.12: Structural parameters for $Mn(Ni_{0.6}Si_{0.4})_2$ obtained from the neutron data refinement

Temperature	298 K
Spacegroup	$P6_3/mmc$
a($\mathring{A}$)	4.7665(4)
c($\mathring{A}$)	7.4605(7))
Magnetic phase	Antiferromagnetic
Mn; 4f (1/3, 2/3, z)	0.0602(10)
B(Mn) ($\mathring{A}^2$)	1.06(15)
M(Mn)(μ_B)	1.52(12)
Ni1 (Occupancy:0.471); 2a (0, 0, 0)	-
B(Ni1) ($\mathring{A}^2$)	1.99(15)
M(Ni1)(μ_B)	0
Si1 (Occupancy:0.529); 2a (0, 0, 0)	-
B(Si1) ($\mathring{A}^2$)	1.99(15)
Ni2 (Occupancy:0.67); 6h (x, 2x, 1/4)	0.8289(7)
B(Ni2) ($\mathring{A}^2$)	0.96(9)
M(Ni2)(μ_B)	-
Si2 (Occupancy:0.33); 6h (x, 2x, 1/4)	0.8289(7)
B(Si2) ($\mathring{A}^2$)	0.96(9)
R_F	5.64
R_{mag}	11.0
χ^2	8.89
R_{wp}	19.2

with the parent antiferromagnetic phase. The impurity phase is, however, can be thought to be extremely small which is indicated by the ZFC-FC difference within the order of 10^{-4} emu. Such a weak phase is not expected to be captured by the neutron refinement as it falls within the errors of the experiment. The ZFC-FC susceptibility was found to diverges at 630 K indicating that to be the Curie temperature of the ferromagnetic phase. The antiferromagnetic to paramagnetic transition was observed at 550 K identifying it to be the Néel temperature. A Curie-Weiss fit was made on the ZFC inverse susceptibility that depicted the Curie constant, C =2.35 (11) emu.K/mol.Oe and the Curie-Weiss temperature Θ_{CW}=-222.02 (40) K.

5.3.6 Discussion

Based on the analysis of the STEM and EELS observations (Sec. 5.3.2), a representation of SRO structure of $Mn(Ni_{0.6}Si_{0.4})_2$ is shown in figures 5.54 (a-c). The Mn atoms order periodically with full occupation the 4f site (Fig. 5.54 (a)). The unique SRO in the crystal is mainly attributed to the arrangement of Ni and Si in 2a that gives rise to several non-periodic units (Fig. 5.54 (b)). These units consist of several small blocks which have Ni or Si 2a atoms as their center. The 6h Ni and Si atoms are arranged depending on which block they belong to (Fig. 5.54 (c)). The Si centered blocks only contain Ni atoms in the 6h positions. While the Ni centered blocks contain the Ni and Si atoms arranged randomly in the 6h. Interestingly, it was observed that each of the non-periodic units have a composition that is somewhat similar to the actual stoichiometry of $Mn(Ni_{0.6}Si_{0.4})_2$. The analysis also points out that 2a sites are predominantly occupied by the Si atoms while the 6h sites by the Ni atoms. The observation is consistent with the occupancy obtained from single crystal refinement. The occupancy of the Ni and Si in the Wyckoff position 2a and 6h

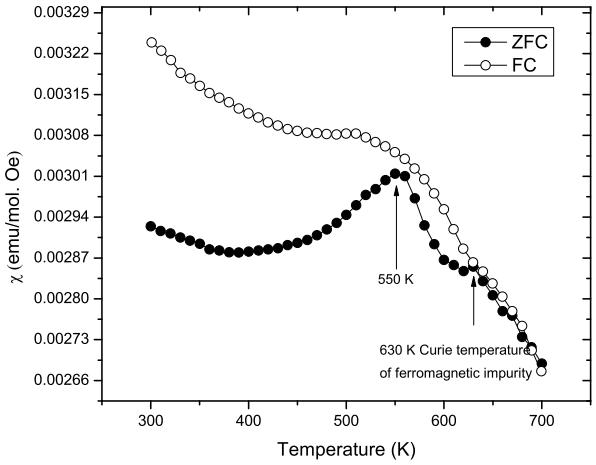

a)

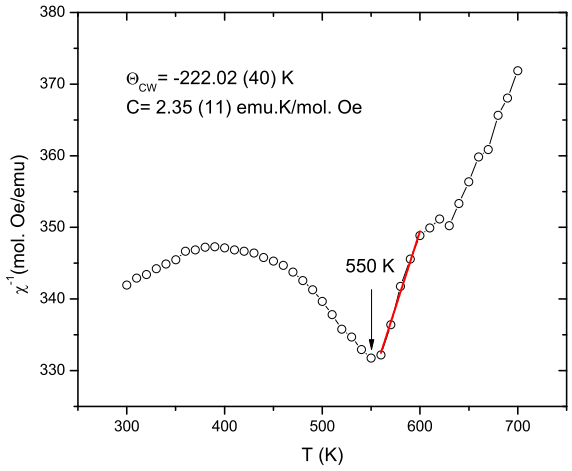

b)

Figure 5.53: a) ZFC-FC magnetic susceptibility of $Mn(Ni_{0.6}Si_{0.4})_2$ with an applied magnetic of 1000 Oe. b) A Curie-Weiss fit on the ZFC inverse susceptibility data above 550 K yielded a Curie constant, C =2.35 (11) emu.K/mol.Oe and the Curie-Weiss temperature Θ_{CW}=-222.02 (40) K

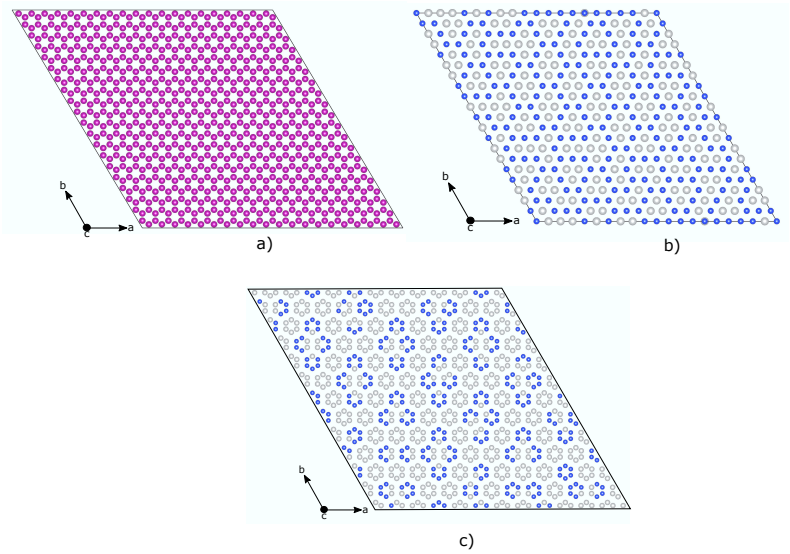

Figure 5.54: A prototype structure of $Mn(Ni_{0.6}Si_{0.4})_2$ generated based on the EELS analysis showing the distribution of a) 4f Mn atoms to form a hexagonal pattern b) Ni and Si in 2a position in a unique manner where Si 2a forms a network containing the Ni 2a atoms inside and c) Ni and Si atoms in 6h.

can be explained in terms of the explanation by Faller and Skolnick [92] (discussed in chapter 1) that the 2a sites will be mostly occupied by the lowest concentration atom if a heteronuclear type bonds are preferred by the occupants of 2a and 6h. Amongst the element Ni and Si in the ternary C14 $Mn(Ni_{0.6}Si_{0.4})_2$, the Si atoms are present in the lowest concentration. Therefore, the occupation of majority 2a sites by Si that is reflected in single crystal occupancy in table 5.11 and, in figure 5.54 (b) can be justified. It is also evident that the system prefers to form heteronuclear Ni-Si bonds more than the homonuclear Ni-Ni or Si-Si bond.

The EELS analysis in (Sec. 5.3.2) captured the atomic resolution mapping of Si in Fig. 5.49e which is a notable observation. To the best of our knowledge, no other previous studies were able to show such accurate mapping of Si atoms.

The electrical conductivity behavior observed in Fig. 5.51 can be considered as a consequence of the unique ordering of the Ni and Si atoms in $Mn(Ni_{0.6}Si_{0.4})_2$. Despite a small range periodicity (Fig 5.54 b and c), the absence of the long-range order is strong enough to destroy the periodic potential which is reflected in the electrical conductivity measurement.

The magnetic structure refined in section 5.3.4 suggested a strong antiferromagnetic interaction between the Mn atoms. The magnetic behavior study in section 5.3.5 showed the susceptibility to be within the range from $\sim$0.003-0.0026 (emu/mol.Oe) with an applied field of 1000 Oe. Such a small value is a confirmation that antiferromagnetic interaction in the system is dominant.

5.4 Stability of Ni_2MnSi

5.4.1 High temperature quenching

Inspired by the work of Adem et al. [130] in stabilizing a Ni_2MnGe type Heusler compound by annealing at a higher temperature, attempts were made to synthesize a single phase Ni_2MnSi by quenching it from higher temperatures. This heat treatment aimed to induce an expected transformation of the $Ni_{16}Mn_6Si_7$ ternary G Phase and $Mn(Ni_{0.6}Si_{0.4})_2$ Laves phase composition to a full L_{21} type Heusler compound at higher temperatures in a similar manner it occured for Ni_2MnGe. It should be mentioned that the Ni-Mn-Si phase diagram modeled by Hu et al. [113] does not indicate any high temperature phase transition or any stable structure for the Ni_2MnSi system. However, this can be due to the fact that modeling did not include any possible Heusler phase for the Ni-Mn-Si system. Our study was conducted with the anticipation that inclusion of the Heusler phase in the modeling by Hu et al. [113] may have resulted in the appearance of the L_{21} type Ni_2MnSi at a higher

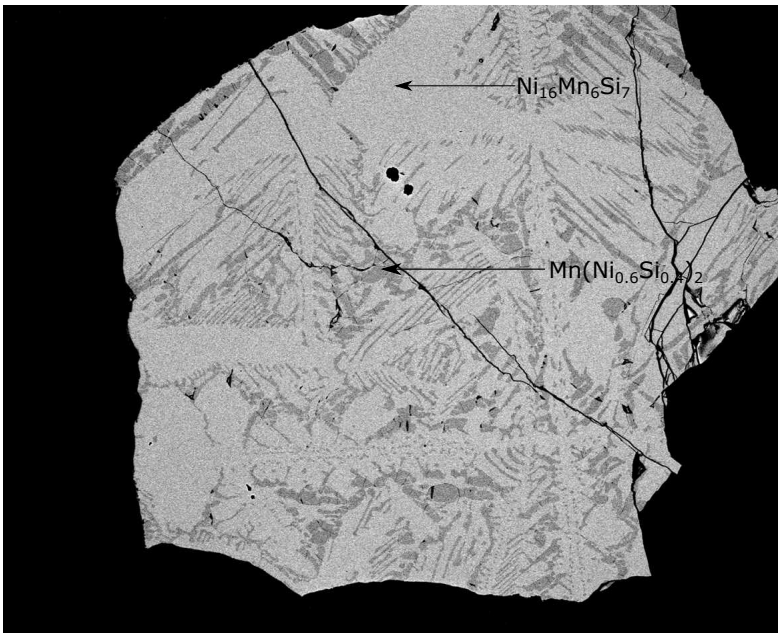

Figure 5.55: SEM image in the backscatter electron mode (BEC) for the Ni_2MnSi composition annealed at 1100^0C for 3 days showing the system to be consisting of $Ni_{16}Mn_6Si_7$ ternary G Phase and $Mn(Ni_{0.6}Si_{0.4})_2$ Laves phase.

temperature.

The first attempt was conducted by annealing the sample at 1100^0C for three days and then, subsequent quenching in an ice-water mixture. However, the scanning electron microscopy (SEM) image (Fig. 5.55) of the Ni_2MnSi clearly showed the presence of multiple phases. The phase composition was determined at several sites of a smaller cross-section area SEM image by means of the energy dispersive X-ray spectroscopy (EDX) method (Fig.5.56). The results indicated the composition of the major phase to be $\sim$61% Ni, 24% Mn and 14% Si that corresponds well to the $\sim$64% Ni, 22.5% Mn and 13.5% Si for the Ni-Mn-Si G phase, $Ni_{16}Mn_6Si_7$. The second phase with an average composition of $\sim$47% Ni, 37% Mn and 15% Si belongs to that of the Ni-Mn-Si Laves phase, $Mn(Ni_{0.6}Si_{0.4})_2$.

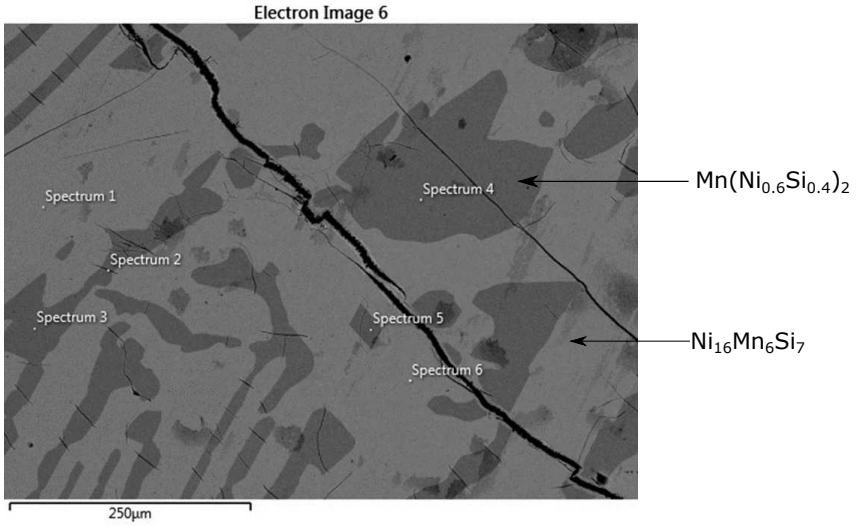

Site	Ni(Wt%)	Mn (Wt%)	Si (Wt%)
Spectrum 1	60.8	25.2	13.9
Spectrum 2	47.6	37.8	14.6
Spectrum 3	46.9	37.9	15.2
Spectrum 4	47.7	37.2	15.1
Spectrum 5	47.1	37.6	15.3
Spectrum 6	61.2	24.8	14

Figure 5.56: SEM/EDX image of the 1100^0C annealed Ni_2MnSi composition showing the composition of $Ni_{16}Mn_6Si_7$ and $Mn(Ni_{0.6}Si_{0.4})_2$ at the selected sites.

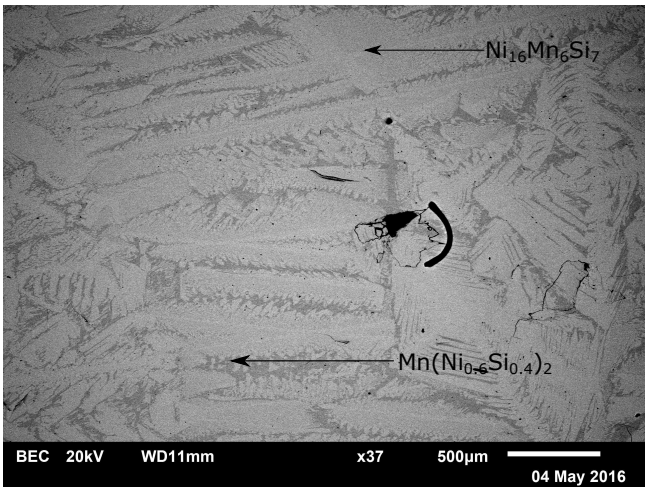

Figure 5.57: SEM image of the arc-melted Ni_2MnSi composition consisting of $Ni_{16}Mn_6Si_7$ and $Mn(Ni_{0.6}Si_{0.4})_2$.

Another observation was done on the as arc-melted sample with no annealing that corresponds to a state obtained by rapidly quenching in the water-cooled copper crucible from the molten state. The SEM image of the sample (Fig. 5.57) again showed the presence of the two phases observed earlier. The SEM/EDX observation (Fig 5.58) at multiples sites pointed out the majority phase having compositions that belong to the Ni-Mn-Si G phase and the second phase being the Ni-Mn-Si Laves phase, $Mn(Ni_{0.6}Si_{0.4})_2$. The study thus found that unlike the Ni_2MnGe system, the high temperature annealing cannot stabilize a L_{21} type Ni_2MnSi. As a consequence, it can be concluded that a single phase Heusler type of structure is not favorable for the Ni_2MnSi composition despite the system having a negative formation energy.

5.4.2 Neutron diffraction study

Neutron diffraction studies were carried out on the sample annealed at 800 °C. The data were collected at 298 K, 100 K, and 4 K, respectively to examine if there are any interesting

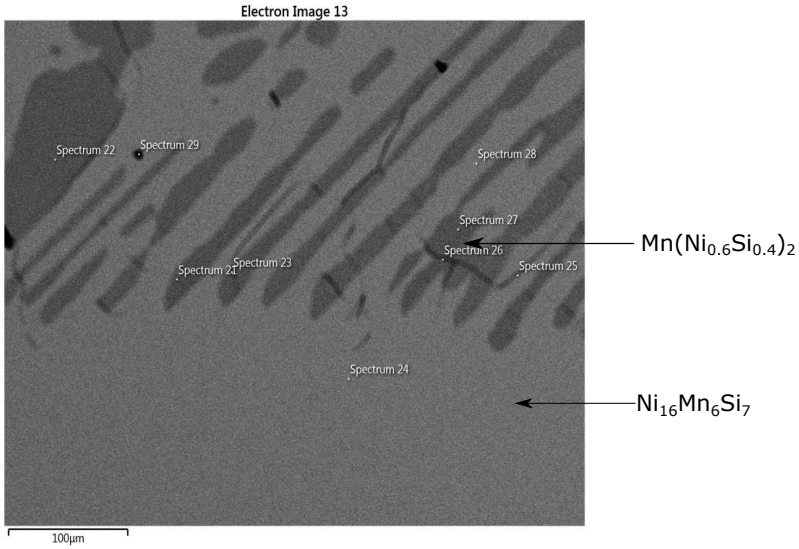

Site	Ni(Wt%)	Mn (Wt%)	Si (Wt%)
Spectrum 21	47.3	37.6	15.1
Spectrum 22	47.3	38	14.6
Spectrum 23	47.6	37.7	14.7
Spectrum 24	59.6	26.7	13.3
Spectrum 28	58.0	28.1	13.9

Figure 5.58: SEM/EDX image of the arc-melted Ni_2MnSi showing the composition of $Ni_{16}Mn_6Si_7$ and $Mn(Ni_{0.6}Si_{0.4})_2$ at the selected sites.

phase transition or appearance of a new phase that can occur at low temperatures.

The 298 K structure was refined to be composed of roughly 60% $Ni_{16}Mn_6Si_7$ and 40% $Mn(Ni_{0.6}Si_{0.4})_2$ which was expected based on the previous observations. The Rietveld refinement profile is shown in Fig. 5.59a. The relevant structural and magnetic parameters are listed in Table 5.13. The refinement for $Mn(Ni_{0.6}Si_{0.4})_2$ was done with occupancy parameters obtained from the single crystal diffraction experiment in section 5.3. Note that, section 5.3 addressed and discussed $Mn(Ni_{0.6}Si_{0.4})_2$ to be antiferromagnetic below 550 K which is also reflected in this room temperature refinement with the magnetic phase refinement finding only the Mn atoms to be ordering antiferromagnetically. All the structural parameters obtained from the refinement was found to be nearly identical to the results from section 5.2.3 and 5.3.4 for the individual phases.

Neutron diffraction data collected at 100 K did not show any sign of additional structural phase transition. Similar to the results of section 5.2, extra reflections that can be indexed as (210), (310), (320) and (312) originated due to the magnetic ordering of $Ni_{16}Mn_6Si_7$. The Rietveld refinement profile is shown in Fig. 5.59b. The relevant structural and magnetic parameters are listed in Table 5.13. All the refined magnetic parameters and the magnetic structure for $Ni_{16}Mn_6Si_7$ were found to be comparable to the single phase refinement performed at 100 K that found a 2D antiferromagnetic arrangement of Mn-I atoms and the Mn-II atoms being geometrically frustrated (Fig5.36). For $Mn(Ni_{0.6}Si_{0.4})_2$, a similar antiferromagnetic configuration as observed in the 298 K data was found. The phase composition was also refined as $\sim$60% $Ni_{16}Mn_6Si_7$ and 40% $Mn(Ni_{0.6}Si_{0.4})_2$.

The 4 K diffraction data also did not show any indications of any extra phase or phase transformation appearing in the structure of the compound. The only difference observed with 100 K data was the extra (100) peak originating due to the canted antiferromagnetism

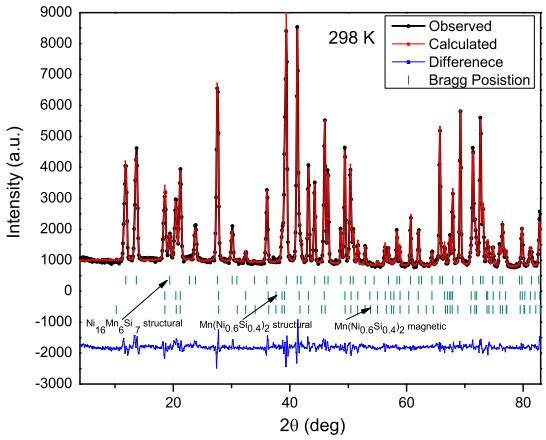

a)

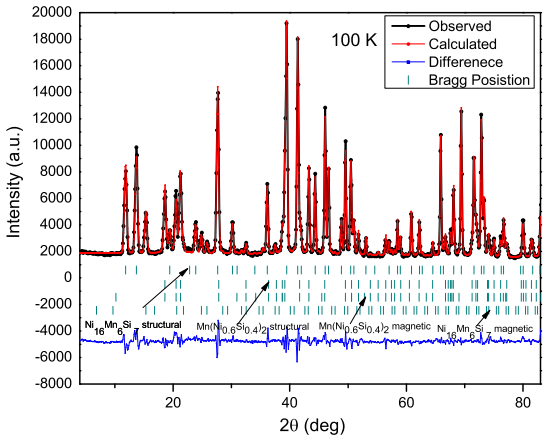

b)

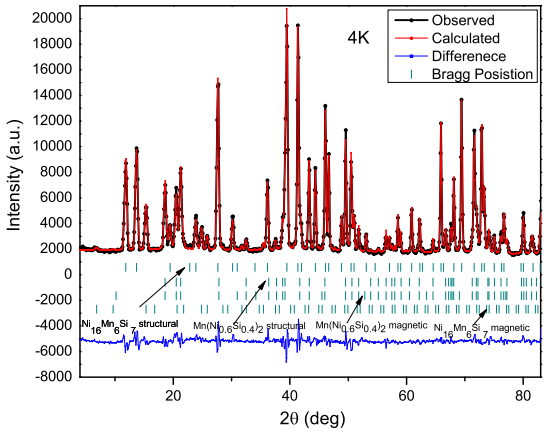

c)

Figure 5.59: Rietveld refinement of the neutron diffraction data for the Ni_2MnSi compositions consisting of $Ni_{16}Mn_6Si_7$ and $Mn(Ni_{0.6}Si_{0.4})_2$ at a) 298 K, b) 100 K and c) 4 K, respectively.

Table 5.13: Refined structural parameters for $Ni_{16}Mn_6Si_7$ and $Mn(Ni_{0.6}Si_{0.4})_2$ in the the Ni_2MnSi composition.

Temperature	298 K	100 K	4 K
	$Ni_{16}Mn_6Si_7$		
Spacegroup	$Fm\bar{3}m$	$Fm\bar{3}m$	$Fm\bar{3}m$
Lattice constant($\AA$)	11.1563(6)	11.1307(4)	11.1273(4)
Magnetic state	Paramagnetic	Antiferromagnetic	Canted Antiferromagnetic
Mn; 24e(x, 1/2, 1/2)	0.6980(7)	0.6980	0.6980
B(Mn) ($\AA^2$)	0.42(22)	0.42(20)	0.11(5)
M(Mn-I)(μ_B)	-	4.42(6)	4.702(11)
M(Mn-II)(μ_B)	-	0	0.895(24)
Ni1; 32f(x, x, x)	0.33312(14)	0.33312	0.33312
B(Ni1) ($\AA^2$)	0.37(7)	0.23(6)	0.32(6)
M(Ni1)(μ_B)	-	0	0
Ni2; 32f(x, x, x)	0.11813(15)	0.11780	0.11780
B(Ni2) ($\AA^2$)	0.54(8)	0.58(7)	0.49(6)
M(Ni2)(μ_B)	-	0	0
Si1; 4a(1/2, 1/2, 0)	-	-	-
B(Si1) ($\AA^2$)	0.40(10)	0.67(37)	0.73(36)
Si2; 24e(1/2, 1/4, 1/4)	-	-	-
B(Si2) ($\AA^2$)	0.34(15)	0.55(14)	0.34(10)
R_F	2.90	2.58	2.88
R_{mag}	-	9.86	9.45
Phase Composition	61.91(1.32)	60.75(1.17)	60.87(1.08)
	$Mn(Ni_{0.6}Si_{0.4})_2$		
Spacegroup	$P6_3/mmc$	$P6_3/mmc$	$P6_3/mmc$
a($\AA$)	4.7591(3)	4.7485(3)	4.7473(3)
c($\AA$)	7.4872(8)	7.4697(7)	7.4675(7)
Magnetic phase	Antiferromagnetic	Antiferromagnetic	Antiferromagnetic
Mn; 4f(1/3, 2/3, z)	0.06579(3)	0.06579	0.06579
B(Mn) ($\AA^2$)	1.26(25)	1.64(25)	1.44(23)
M(Mn)(μ_B)	1.98(8)	2.12(10)	2.07(10)
Ni1 (Occupancy:0.471); 2a(0, 0, 0)	-	-	-
B(Ni1) ($\AA^2$)	1.21(21)	1.51(21)	1.71(21)
M(Ni1)(μ_B)	0	0	0
Si1 (Occupancy:0.529); 2a(0, 0, 0)	-	-	-
B(Si1) ($\AA^2$)	1.21(21)	1.51(21)	1.71(21)
Ni2 (Occupancy:0.67); 6h(x, 2x, 1/4)	0.82873(14)	0.82873	0.82873
B(Ni2) ($\AA^2$)	0.91(15)	1.03(14)	0.93(13)
M(Ni2)(μ_B)	-	0	0
Si2 (Occupancy:0.33); 6h(x, 2x, 1/4)	0.82873(14)	0.82873	0.82873
B(Si2) ($\AA^2$)	0.91(15)	1.03(14)	0.93(13)
R_F	3.26	3.06	3.07
R_{mag}	3.40	5.15	5.58
Phase Composition	38.09(1.22)	39.25(1.11)	39.13(1.10)
χ^2	4.65	9.94	10.3
R_{wp}	11.6	11.2	11.0

of $Ni_{16}Mn_6Si_7$ appearing below 50 K due to the collinear rotation of magnetic moments about the axis (Fig. 5.38). The Rietveld refinement profile is shown in Fig. 5.59b and all the relevant parameters are listed in Table 5.13. The phase composition was identical to the composition at 100 K and 298 K (∼60% $Ni_{16}Mn_6Si_7$ and 40% $Mn(Ni_{0.6}Si_{0.4})_2$).

5.4.3 Stability of Ni_2MnSi from first-principles

Our initial first-principles calculation computed a formation energy of -1.46 eV/f.u indicating stable Heusler Ni_2MnSi. However, as discussed in previous sections such a stable phase is not formable in any ambient temperature conditions. The Ni_2MnSi composition always consists of two phases, i.e., $Ni_{16}Mn_6Si_7$ ternary G phase and $Mn(Ni_{0.6}Si_{0.4})_2$) ternary C14 Laves phase. In this section, we attempt to address that with our first-principles study. The decomposition of Ni_2MnSi into two phases can be expressed in terms of a reaction as,

$$11\, Ni_2MnSi \rightarrow Ni_{16}Mn_6Si_7 + 5\, Mn(Ni_{0.6}Si_{0.4})_2. \tag{5.29}$$

In the framework of the first-principles calculation, the ground state formation enthalpy per formula unit for Ni_2MnSi can be computed in terms of the decomposition to the neighboring phases as,

$$\Delta H = E_{tot}(Ni_2MnSi) - \frac{1}{11}E_{tot}(Ni_{16}Mn_6Si_7) - \frac{5}{11}E_{tot}(Mn(Ni_{0.6}Si_{0.4})_2) \tag{5.30}$$

where, $E_{tot}(Ni_2MnSi)$ is the total energy per formula unit for the hypothetical L_{21} Ni_2MnSi structure, $E_{tot}(Ni_{16}Mn_6Si_7)$ and $E_{tot}(\, Mn(Ni_{0.6}Si_{0.4})_2))$ are the total energy per formula unit for $Ni_{16}Mn_6Si_7$ ternary G phase and $Mn(Ni_{0.6}Si_{0.4})_2$) ternary C14 Laves phase, respectively.

The energy calculations for all the structures were done with the first-principles computation implemented in the VASP. The generalized gradient approximation (GGA) exchange correlation functional [156] along with Hubbard correction U of 1.98 and 1.62 eV was used to properly address the electron localization of 3d states of Ni and Mn, respectively [48, 173]. The calculation yielded a positive ΔH of 0.77 eV/f.u. for the hypothetical L_{21} Ni_2MnSi which is an indication of the unstable configuration of the system in contrast to the two neighboring phases. In terms of external temperature effects, the high energy corresponds to a thermal barrier of $\sim$9000 K that is required to be overcome in order to move reaction 5.29 in the opposite direction, i.e., a stable Ni_2MnSi formation which is not possible to achieve. Consequently, a stable Heusler phase does not exist for the Ni-Mn-Si system under ambient conditions.

5.4.4 Discussion

Analysis of section 5.4.1 and 5.4.2 confirms that it is not possible to synthesize a single phase Heusler type Ni_2MnSi and the system forms a mixture of $Ni_{16}Mn_6Si_7$ ternary G phase and $Mn(Ni_{0.6}Si_{0.4})_2$) ternary C14 Laves phase at any ambient temperatures. This results can be explained in terms of the first-principles calculations which showed that Ni_2MnSi is characterized by high formation enthalpy of 0.77 eV/f.u., which needs to be overcome by an external source such as temperature or pressure. If considered the external temperature effect only, the system would require $\sim$9000 K for the Ni_2MnSi to form. In comparison, in our experiment the highest quenching condition maintained was for the as arc-melted samples that involved temperatures within the range of $\sim$2000-2500 K, which is still much lower from what is required for formations of a single phase Ni_2MnSi. It is indeed not practical to achieve such a condition of formation for the bulk Heulser Ni_2MnSi.

Chapter 6

Summary

In this work, we have studied the crystal structure and range of physical properties, including magnetic and transport properties, of three single phase systems Co_2MnSi, $Ni_{16}Mn_6Si_7$ and $Mn(Ni_{0.6}Si_{0.4})_2$. Additionally, we characterized the Ni_2MnSi compound that exists as a mixture of $Ni_{16}Mn_6Si_7$ and $Mn(Ni_{0.6}Si_{0.4})_2$. The summary of present studies can be described as follows.

6.1 Co_2MnSi

We performed an experimental and theoretical study of the structural disorder and magnetic interactions in the half-metallic Co_2MnSi system. The results pointed out that the system mainly consists of equivalent concentrations of disorders involving Co and Mn sites. From the neutron refinement, the Co and Mn disorder of $\sim$6.5% and $\sim$7.6% was obtained which was corroborated by the theoretical study. Our work on the disorder occupancies also showed that the antisite disorder in the half-metallic Co_2MnSi is unavoidable as the

formation of such disorder is energetically favorable in ambient conditions. An antiferromagnetic interaction due to disordered Mn atoms were detected in the first-principles study which was reflected as a reduction in the neutron refined magnetic moments at 298 K, 100 K, and 4 K. The system exhibits a ferromagnetic to paramagnetic transition at $\sim$1014 K that was confirmed by the high temperature dilatometry and electrical resistivity measurement on a Czochralski grown single crystal.

Disorders are one of the causes of the destruction of half-metallicity in a system, and our work showed that this is unavoidable for the Co_2MnSi system. Consequently, a 100% spin polarization is not achievable. The search for new Heusler compounds for half-metallicity thus should consider the disorder effect factor in alloy design.

6.2 $Ni_{16}Mn_6Si_7$

We have addressed the complex magnetic ordering of the $Ni_{16}Mn_6Si_7$ system involving a geometric frustration, canted antiferromagnetism and spin freezing that is corroborated by the magnetic behavior. Below the Néel temperature of 197 K, $Ni_{16}Mn_6Si_7$ undergoes a transition to the antiferromagnetic system with 2/3 of magnetic Mn spins getting ordered, and the rest of the Mn remain geometrically frustrated. Another phase transition occurs below 50 K where the ordered moments cant away by an angle of 9^0 to give rise to weak ferromagnetism that has also been detected by the magnetic hysteresis measurement. The evidence of a weak spin freezing effect was detected below 6 K with a gradual drop in the ZFC magnetic susceptibility. A magnetic field induced smeared spin-flop type transition was also observed at lower temperatures.

Due to the complex nature of the magnetic structure and properties, there have been a very limited number of investigations of the physical properties of the ternary G phase

systems. However, as discussed in this work, such system possesses some unique magnetic ordering that leads to interesting properties such as canted antiferromagnetism, geometric frustration. Our observations can encourage future studies to explore new ternary G phase systems for interesting magneto-structural coupling. In addition, studies of properties of $Ni_{16}Mn_6Si_7$ can provide guidance to characterize other complex G phase systems.

6.3 $Mn(Ni_{0.6}Si_{0.4})_2$

We resolved the short-range atomic ordering and characterized physical properties of the antiferromagnetic Ni-Mn-Si based Laves phase with the composition $Mn(Ni_{0.6}Si_{0.4})_2$. The system is stabilized as a strong antiferromagnet below 550 K. The atomic ordering determined with the high-resolution transmission electron microscopy (HRTEM) and electron energy loss spectroscopy analysis (EELS) revealed a short-range atomic arrangement between Ni and Si atoms that produces small blocks of unit cells that are non-periodic but have the $Mn(Ni_{0.6}Si_{0.4})_2$ stoichiometry. The EELS analysis in this work was also able to produce the atomic resolution mapping of Si which has not been detected before by any other research. During further physical property characterization, the study also reported a semiconductor like temperature dependence of the electrical conductivity for the metallic $Mn(Ni_{0.6}Si_{0.4})_2$ which was associated with short-range ordering that induced localization of conduction electrons.

Despite being a frequently encountered phenomenon for the C14 Laves phase, there have been no previous reports of the short-range atomic ordering in these compounds. However, as evident by the semiconductor like temperature dependence of electrical conductivity of $Mn(Ni_{0.6}Si_{0.4})_2$, such ordering gives rise to unusual behavior and can be topic of scientific interest. Our work should encourage future investigations of the short-range

structure-properties relationship of other ternary Laves phases.

6.4 Ni_2MnSi

We have attempted to stabilize a single phase Ni_2MnSi with high-temperature heat treatment. All our efforts ended with the conclusion that a single phase Ni_2MnSi is not formable at any ambient temperature conditions. With a further first-principles formation enthalpy analysis in terms of $Ni_{16}Mn_6Si_7$ and $Mn(Ni_{0.6}Si_{0.4})_2$, our study explained the unstability of Ni_2MnSi to be due to the neighboring phases being energetically more favorable by 0.77 eV/f.u.. We then discussed that possibility of forming stable Ni_2MnSi require the system to overcome such higher energy barrier that corresponds to being in the state with an external temperature of $\sim$9000 K which is not achievable.

One important conclusion can be drawn from our inability to synthesize a single phase Ni_2MnSi. Most of the first-principles studies rely on the calculation of the formation enthalpy of a phase in terms of the constituting elements to predict the stability of an unknown compound. Our results pointed out that such a calculation may not always lead to a stable compound. Despite having a negative formation enthalpy, a system might still be unstable due to the neighboring phases being more stable with a marginal energy difference. In such a case, the compound decomposes into those more favorable phases which occurred during our synthesis attempt. An ideal approach would be to compute phase diagram using thermodynamic techniques, but to our best knowledge no thermodynamic database is available for these systems.

Bibliography

[1] J Kübler, GH Fecher, and C Felser. Understanding the trend in the curie temperatures of co 2-based heusler compounds: Ab initio calculations. *Phys. Rev. B*, 76(2): 024414, 2007.

[2] M Kolenda, A Szytuła, J Leciejewicz, and C Maletka. Magnetic properties of mn6 ni16 si7 and mn3 cr3 ni16 si7. *Journal of magnetism and magnetic materials*, 96(1): 121–124, 1991.

[3] T Fries, Y Shapira, Fernando Palacio, M Carmen Morón, Garry J McIntyre, R Kershaw, A Wold, EJ McNiff, et al. Magnetic ordering of the antiferromagnet cu 2 mnsns 4 from magnetization and neutron-scattering measurements. *Phys. Rev. B*, 56 (9):5424, 1997.

[4] AP Ramirez. Strongly geometrically frustrated magnets. *Annu. Rev. Mater. Sci.*, 24 (1):453–480, 1994.

[5] John E. Greedan. Geometrically frustrated magnetic materials. *J. Mater. Chem.*, 11: 37–53, 2001.

[6] N Hur, S Park, PA Sharma, JS Ahn, S Guha, and SW Cheong. Electric polarization

reversal and memory in a multiferroic material induced by magnetic fields. *Nature*, 429(6990):392, 2004.

[7] John E Greedan. Frustrated rare earth magnetism: Spin glasses, spin liquids and spin ices in pyrochlore oxides. *J. Alloys Compd.*, 408:444–455, 2006.

[8] Feng Ye, Jaime A Fernandez-Baca, Randy Scott Fishman, Y Ren, HJ Kang, Y Qiu, and T Kimura. Magnetic interactions in the geometrically frustrated triangular lattice antiferromagnet cufeo 2. *Phys. Rev. Lett.*, 99(15):157201, 2007.

[9] P-É Melchy and ME Zhitomirsky. Interplay of anisotropy and frustration: Triple transitions in a triangular-lattice antiferromagnet. *Phys. Rev. B*, 80(6):064411, 2009.

[10] Sihao Deng, Ying Sun, Lei Wang, Zaixing Shi, Hui Wu, Qingzhen Huang, Jun Yan, Kewen Shi, Pengwei Hu, Ali Zaoui, et al. Frustrated triangular magnetic structures of mn3znn: Applications in thermal expansion. *J. Phys. Chem. C*, 119(44):24983–24990, 2015.

[11] D Fruchart. Magnetic studies of the metallic perovskite-type compounds of manganese. *J Phys Soc Jpn*, 44(3):781–791, 1978.

[12] Ming-Hui Yu, LH Lewis, and AR Moodenbaugh. Large magnetic entropy change in the metallic antiperovskite mn 3 gac. *J Appl Phys*, 93(12):10128–10130, 2003.

[13] En-Cui Yang, Zhong-Yi Liu, Xiao-Yun Wu, Hong Chang, En-Chan Wang, and Xiao-Jun Zhao. Co ii, mn ii and cu ii-directed coordination polymers with mixed tetrazolate–dicarboxylate heterobridges exhibiting spin-canted, spin-frustrated antiferromagnetism and a slight spin-flop transition. *Dalton Trans.*, 40(39):10082–10089, 2011.

[14] K Matan, BM Bartlett, JS Helton, V Sikolenko, S Mat'aš, K Prokeš, Ying Chen, Jeffrey W Lynn, D Grohol, TJ Sato, et al. Dzyaloshinskii-moriya interaction and spin reorientation transition in the frustrated kagome lattice antiferromagnet. *Phys. Rev. B*, 83(21):214406, 2011.

[15] Jun Yan, Ying Sun, Hui Wu, Qingzhen Huang, Cong Wang, Zaixing Shi, Sihao Deng, Kewen Shi, Huiqing Lu, and Lihua Chu. Phase transitions and magnetocaloric effect in mn3cu0. 89n0. 96. *Acta Mater.*, 74:58–65, 2014.

[16] Catherine Dendrinou-Samara, James PS Walsh, Christopher A Muryn, David Collison, Richard EP Winpenny, and Floriana Tuna. Evidence of spin canting, metamagnetism, negative coercivity and slow relaxation in a two-dimensional network of {Mn6} cages. *Eur. J. Inorg. Chem.*, pages 485–492, 2018.

[17] T Shimizu, T Shibayama, K Asano, and K Takenaka. Giant magnetostriction in tetragonally distorted antiperovskite manganese nitrides. *J. Appl. Phys.*, 111(7): 07A903, 2012.

[18] T Shibayama and K Takenaka. Giant magnetostriction in antiperovskite mn3cun. *J Appl Phys*, 109(7):07A928, 2011.

[19] Ying Sun, Yanfeng Guo, Yoshihiro Tsujimoto, Cong Wang, Jun Li, Xia Wang, Hai L Feng, Clastin I Sathish, Yoshitaka Matsushita, and Kazunari Yamaura. Unusual magnetic hysteresis and the weakened transition behavior induced by sn substitution in mn3sbn. *J. Appl. Phys.*, 115(4):043509, 2014.

[20] K Kamishima, T Goto, H Nakagawa, N Miura, M Ohashi, N Mori, T Sasaki, and

T Kanomata. Giant magnetoresistance in the intermetallic compound mn 3 gac. *Phys. Rev. B*, 63(2):024426, 2000.

[21] Philip CE Stamp and Alejandro Gaita-Arino. Spin-based quantum computers made by chemistry: hows and whys. *J. Mater. Chem.*, 19(12):1718–1730, 2009.

[22] Marco Evangelisti and Euan K Brechin. Recipes for enhanced molecular cooling. *Dalton Trans.*, 39(20):4672–4676, 2010.

[23] Filippo Troiani and Marco Affronte. Molecular spins for quantum information technologies. *Chem. Soc. Rev.*, 40(6):3119–3129, 2011.

[24] Grigore A Timco, Thomas B Faust, Floriana Tuna, and Richard EP Winpenny. Linking heterometallic rings for quantum information processing and amusement. *Chem. Soc. Rev.*, 40(6):3067–3075, 2011.

[25] Liang Dong, Hemant Kumar, Babak Anasori, Yury Gogotsi, and Vivek B Shenoy. Rational design of two-dimensional metallic and semiconducting spintronic materials based on ordered double-transition-metal mxenes. *J. Phys. Chem. Lett.*, 8(2): 422–428, 2017.

[26] F Heusler. *Verh Dtsch Phys Ges*, 5:219, 1903.

[27] F Heusler, W Starck, and E Haupt. *Verh Dtsch Phys Ges*, 5:220, 1903.

[28] Tanja Graf and Claudia Felser. Heusler compounds at a glance. In *Spintronics*, pages 1–13. Springer, 2013.

[29] J Kübler, AR William, and CB Sommers. Formation and coupling of magnetic moments in heusler alloys. *Physical Review B*, 28(4):1745, 1983.

[30] A Planes, Ll Mañosa, X Moya, T Krenke, M Acet, and EF Wassermann. Magnetocaloric effect in heusler shape-memory alloys. *Journal of Magnetism and Magnetic Materials*, 310(2):2767–2769, 2007.

[31] D Jung, H-J Koo, and M-H Whangbo. Study of the 18-electron band gap and ferromagnetism in semi-heusler compounds by non-spin-polarized electronic band structure calculations. *Journal of Molecular Structure: THEOCHEM*, 527(1):113–119, 2000.

[32] David Kieven, Reiner Klenk, Shahab Naghavi, Claudia Felser, and Thomas Gruhn. I-ii-v half-heusler compounds for optoelectronics: Ab initio calculations. *Physical Review B*, 81(7):075208, 2010.

[33] Tanja Graf, Claudia Felser, and Stuart SP Parkin. Simple rules for the understanding of heusler compounds. *Progress in solid state chemistry*, 39(1):1–50, 2011.

[34] RA De Groot, AM van der Kraan, and KHJ Buschow. Femnsb: a half-metallic ferrimagnet. *Journal of magnetism and magnetic materials*, 61(3):330–336, 1986.

[35] Robert A de Groot. Half-metallic magnetism in the 1990s. *Physica B: Condensed Matter*, 172(1):45–50, 1991.

[36] Vadim Ksenofontov, Gennadiy Melnyk, Marek Wojcik, Sabine Wurmehl, Kristian Kroth, Sergey Reiman, Peter Blaha, and Claudia Felser. Structure and properties of comnsb in the context of half-metallic ferromagnetism. *Physical Review B*, 74(13): 134426, 2006.

[37] Ch Hordequin, E Lelievre-Berna, and J Pierre. Magnetization density in the half-metallic ferromagnet nimnsb. *Physica B: Condensed Matter*, 234:602–604, 1997.

[38] J. Slater. *Phys. Rev.*, 49:537, 1936.

[39] L. Pauling. *Phys. Rev.*, 54:899, 1938.

[40] Peter Grünberg, R Schreiber, Y Pang, MB Brodsky, and H Sowers. Layered magnetic structures: evidence for antiferromagnetic coupling of fe layers across cr interlayers. *Phys. Rev. Lett.*, 57(19):2442, 1986.

[41] Mario Norberto Baibich, Jean Marc Broto, Albert Fert, F Nguyen Van Dau, Frédéric Petroff, P Etienne, G Creuzet, A Friederich, and J Chazelas. Giant magnetoresistance of (001) fe/(001) cr magnetic superlattices. *Phys. Rev. Lett.*, 61(21):2472, 1988.

[42] RA De Groot, FM Mueller, PG Van Engen, and KHJ Buschow. New class of materials: half-metallic ferromagnets. *Phys. Rev. Lett.*, 50(25):2024, 1983.

[43] J Kübler, AR William, and CB Sommers. Formation and coupling of magnetic moments in heusler alloys. *Phys. Rev. B*, 28(4):1745, 1983.

[44] J Kübler. First principle theory of metallic magnetism. *Physica B+ C*, 127(1-3): 257–263, 1984.

[45] S Fujii, S Sugimura, S Asano, et al. Hyperfine fields and electronic structures of the heusler alloys co2mnx (x= al, ga, si, ge, sn). *J. Phys.: Condens. Matter*, 2(43):8583, 1990.

[46] Valentin Yu Irkhin and Mikhail Iosifovich Katsnel'son. Half-metallic ferromagnets. *Physics-Uspekhi*, 37(7):659, 1994.

[47] Gerhard H Fecher, Hem Chandra Kandpal, Sabine Wurmehl, Jonder Morais, Hong-Ji Lin, Hans-Joachim Elmers, Gerd Schönhense, and Claudia Felser. Design of magnetic materials: the electronic structure of the ordered, doped heusler compound co2cr1- xfexal. *J. Phys.: Condens. Matter*, 17(46):7237, 2005.

[48] Hem C Kandpal, Gerhard H Fecher, and Claudia Felser. Calculated electronic and magnetic properties of the half-metallic, transition metal based heusler compounds. *J. Phys. D: Appl. Phys.*, 40(6):1507, 2007.

[49] William H Butler, Claudia KA Mewes, Chunsheng Liu, and Tianyi Xu. Rational design of half-metallic heterostructures. *arXiv preprint arXiv:1103.3855*, 2011.

[50] Shoji Ishida, Shinpei Fujii, Shoei Kashiwagi, and Setsuro Asano. Search for half-metallic compounds in co2mnz (z= iiib, ivb, vb element). *J. Phys. Soc. Jpn.*, 64(6): 2152–2157, 1995.

[51] Koichiro Inomata, Susumu Okamura, Ryota Goto, and Nobuki Tezuka. Large tunneling magnetoresistance at room temperature using a heusler alloy with the b2 structure. *Japanese journal of applied physics*, 42(4B):L419, 2003.

[52] S Kämmerer, Andy Thomas, Andreas Hütten, and Günter Reiss. Co2mnsi heusler alloy as magnetic electrodes in magnetic tunnel junctions. *Appl. Phys. Lett.*, 85(1): 79–81, 2004.

[53] XY Dong, C Adelmann, JQ Xie, CJ Palmstrøm, X Lou, J Strand, PA Crowell, J-P Barnes, and AK Petford-Long. Spin injection from the heusler alloy co 2 mnge into al 0.1 ga 0.9 as/ gaas heterostructures. *Appl. Phys. Lett.*, 86(10):102107, 2005.

[54] K Yakushiji, K Saito, S Mitani, K Takanashi, YK Takahashi, and K Hono. Current-perpendicular-to-plane magnetoresistance in epitaxial co 2 mnsi/cr/co 2 mnsi trilayers. *Appl. Phys. Lett.*, 88(22):222504–222504, 2006.

[55] T Furubayashi, K Kodama, H Sukegawa, YK Takahashi, K Inomata, and K Hono. Current-perpendicular-to-plane giant magnetoresistance in spin-valve structures using epitaxial co 2 feal 0.5 si 0.5/ag/co 2 feal 0.5 si 0.5 trilayers. *Appl. Phys. Lett.*, 93 (12):122507, 2008.

[56] K Kodama, T Furubayashi, H Sukegawa, TM Nakatani, K Inomata, and K Hono. Current-perpendicular-to-plane giant magnetoresistance of a spin valve using co 2 mnsi heusler alloy electrodes. *J. Appl. Phys.*, 105(7):07E905, 2009.

[57] Konstantin Nikolaev, Paul Kolbo, Taras Pokhil, Xilin Peng, Yonghua Chen, Thomas Ambrose, and Oleg Mryasov. “all-heusler alloy” current-perpendicular-to-plane giant magnetoresistance. *Appl. Phys. Lett.*, 94(22):222501, 2009.

[58] S Tsunegi, Y Sakuraba, M Oogane, ND Telling, LR Shelford, E Arenholz, G Van Der Laan, RJ Hicken, K Takanashi, and Y Ando. Tunnel magnetoresistance in epitaxially grown magnetic tunnel junctions using heusler alloy electrode and mgo barrier. *J. Phys. D: Appl. Phys.*, 42(19):195004, 2009.

[59] Christian Herbort, Elena Arbelo Jorge, and Martin Jourdan. Morphology induced magnetoresistance enhancement of tunneling junctions with the heusler electrode co 2 cr 0.6 fe 0.4 al. *Appl. Phys. Lett.*, 94(14):142504, 2009.

[60] AH MacDonald, T Jungwirth, and M Kasner. Temperature dependence of itinerant electron junction magnetoresistance. *Phys. Rev. Lett.*, 81(3):705, 1998.

[61] Peter A Dowben and Ralph Skomski. Finite-temperature spin polarization in half-metallic ferromagnets. *J. Appl. Phys.*, 93(10):7948–7950, 2003.

[62] MI Katsnelson, V Yu Irkhin, Liviu Chioncel, AI Lichtenstein, and Robert A de Groot. Half-metallic ferromagnets: From band structure to many-body effects. *Rev. Mod. Phys.*, 80(2):315, 2008.

[63] Liviu Chioncel, Yuya Sakuraba, Enrico Arrigoni, MI Katsnelson, M Oogane, Y Ando, T Miyazaki, Emil Burzo, and AI Lichtenstein. Nonquasiparticle states in co 2 mnsi evidenced through magnetic tunnel junction spectroscopy measurements. *Phys. Rev. Lett.*, 100(8):086402, 2008.

[64] P. Blaha, K. Schwarz, G. K. H. Madsen, D. Kvasnicka, and J. Luitz. *WIEN2K, An Augmented Plane Wave + Local Orbitals Program for Calculating Crystal Properties*. Karlheinz Schwarz, Techn. Universität Wien, Austria, 2001.

[65] HJ Beattie and FL VerSnyder. A new complex phase in a high-temperature alloy. 1956.

[66] FX Spiegel, PA BECK, and D BARDOS. Ternary g and e silicides and germanides of transition elements. *Trans. Metall. AIME*, 227(3):575, 1963.

[67] P Chaudouet, R Madar, R Fruchart, and B Lambert. Etude de nouveaux pnictures ternaires de metaux de transition isostructuraux des phases g, ni16mn6p7, ni16mn6as7. *Mater. Res. Bull.*, 18(6):713–719, 1983.

[68] KL Holman, E Morosan, PA Casey, Lu Li, NP Ong, T Klimczuk, C Felser, and RJ Cava. Crystal structure and physical properties of mg6cu16si7-type m6ni16si7, for m= mg, sc, ti, nb, and ta. *Mater. Res. Bull.*, 43(1):9–15, 2008.

[69] GJ Bowden, JM Cadogan, H De Leon, and DH Ryan. The easy magnetization directions in r 6 fe 23 intermetallic compounds: A crystal field analysis. *J Appl Phys*, 81(8):4186–4188, 1997.

[70] J Ostorero. Magnetic properties of (ho, y) 6fe23 intermetallic compounds. *J Alloys Compd*, 317:450–454, 2001.

[71] J Ostoréro, V Paul-Boncour, F Bourée, and G André. Neutron diffraction study of ho5yfe23 and ho5yfe23d16 deuteride. *J Alloys Compd*, 404:191–194, 2005.

[72] PHILIP W Anderson. Ordering and antiferromagnetism in ferrites. *Phys. Rev.*, 102 (4):1008, 1956.

[73] G Toulouse. Theory of the frustration effect in spin glasses: I. *Spin Glass Theory and Beyond: An Introduction to the Replica Method and Its Applications*, 9:99, 1987.

[74] I Dzyaloshinsky. A thermodynamic theory of "weak" ferromagnetism of antiferromagnetics. *J. Phys. Chem. Solids*, 4(4):241–255, 1958.

[75] Tôru Moriya. Anisotropic superexchange interaction and weak ferromagnetism. *Phys. Rev.*, 120(1):91, 1960.

[76] James B Friauf. The crystal structures of two intermetallic compounds. *J. Am. Chem. Soc.*, 49(12):3107–3114, 1927.

[77] James B Friauf. The crystal structure of magnesium di-zincide. *Phys. Rev.*, 29(1): 34, 1927.

[78] Fritz Laves. Kristallographie der legierungen. *Naturwissenschaften*, 27(5):65–73, 1939.

[79] Frank Stein, Martin Palm, and Gerhard Sauthoff. Structure and stability of laves phases. part i. critical assessment of factors controlling laves phase stability. *Intermetallics*, 12(7-9):713–720, 2004.

[80] RC Mittal, SK Si, and KP Gupta. Si-stabilised c14 laves phases in the transition metal systems. *J. Less. Common. Met.*, 60(1):75–82, 1978.

[81] XL Yan, Xing-Qiu Chen, A Grytsiv, VT Witusiewicz, P Rogl, R Podloucky, and G Giester. On the ternary laves phases {Sc, Ti} 2m3si (m= cr, mn, fe, co, ni) with mgzn2-type. *J. Alloys Compd.*, 429(1-2):10–18, 2007.

[82] Ayan Bhowmik, Hon Tong Pang, Steffen Neumeier, Howard J Stone, and Ian Edmonds. Microstructure and oxidation resistance of cr-ta-si alloys. *MRS Online Proceedings Library Archive*, 1295, 2011.

[83] X Yan, MW Pieper, H Michor, G Hilscher, M Reissner, A Grytsiv, P Rogl, V Pomjakushin, G Giester, E Bauer, et al. Phase relations, crystal chemistry, and physical properties of mgzn 2-type laves phases in the mn-cu-si and mn-ni-si systems. *Phys. Rev. B*, 88(17):174416, 2013.

[84] Alexander Kerkau. Disorder in laves phases. 2012.

[85] Q Yao, J Sun, Y Zhang, and B Jiang. First-principles studies of ternary site occupancy in the c15 nbcr2 laves phase. *Acta Mater*, 54(13):3585–3591, 2006.

[86] M Palm, G Inden, and N Thomas. The fe-a1-ti system. *Journal of phase equilibria*, 16(3):209–222, 1995.

[87] T Buhler, SG Fries, PJ Spencer, and HL Lukas. A thermodynamic assessment of the al-cu-mg ternary system. *Journal of phase equilibria*, 19(4):317–333, 1998.

[88] CT Liu, JH Zhu, MP Brady, CG McKamey, and LM Pike. Physical metallurgy and mechanical properties of transition-metal laves phase alloys. *Intermetallics*, 8(9-11): 1119–1129, 2000.

[89] M Bououdina, B Lambert-Andron, B Ouladdiaf, S Pairis, and D Fruchart. Structural investigations by neutron diffraction of equi-atomic zr–ti (v)–ni (co) compounds and their related hydrides. *Journal of alloys and compounds*, 356:54–58, 2003.

[90] M Palm, W Sanders, and G Sauthoff. Phase equilibria in the ni-al-ta system. *Zeitschrift für Metallkunde*, 87(5):390–398, 1996.

[91] Xinlin Yan, X-Q Chen, A Grytsiv, P Rogl, R Podloucky, V Pomjakushin, H Schmidt, and G Giester. Crystal structure, phase stability and elastic properties of the laves phase zrticu2. *Intermetallics*, 16(5):651–657, 2008.

[92] JG Faller and LP Skolnick. Atomic arrangements in the c14 laves phase zr (vco) $sub2$. *Trans. AIME*, 227, 1963.

[93] SF Cheng, B Nadgomy, K Bussmann, EE Carpenter, BN Das, G Trotter, MP Raphael, and VG Harris. Growth and magnetic properties of single crystal co/sub 2/mnx (x= si, ge) heusler alloys. *IEEE transactions on magnetics*, 37(4): 2176–2178, 2001.

[94] B Ravel, MP Raphael, VG Harris, and Q Huang. Exafs and neutron diffraction study of the heusler alloy co 2 mnsi. *Physical Review B*, 65(18):184431, 2002.

[95] MP Raphael, B Ravel, Q Huang, MA Willard, SF Cheng, BN Das, RM Stroud, KM Bussmann, JH Claassen, and VG Harris. Presence of antisite disorder and its

characterization in the predicted half-metal co 2 mnsi. *Phys. Rev. B*, 66(10):104429, 2002.

[96] Lance Ritchie, Gang Xiao, Yi Ji, TY Chen, CL Chien, Ming Zhang, Jinglan Chen, Zhuhong Liu, Guangheng Wu, and XX Zhang. Magnetic, structural, and transport properties of the heusler alloys co 2 mnsi and nimnsb. *Phys. Rev. B*, 68(10):104430, 2003.

[97] Yuya Sakuraba, Jun Nakata, Mikihiko Oogane, Hitoshi Kubota, Yasuo Ando, Akimasa Sakuma, and Terunobu Miyazaki. Huge spin-polarization of l21-ordered co2mnsi epitaxial heusler alloy film. *Jpn. J. Appl. Phys.*, 44(8L):L1100, 2005.

[98] Laura Jane Singh, Zoe Helen Barber, Y Miyoshi, Y Bugoslavsky, WR Branford, and LF Cohen. Structural, magnetic, and transport properties of thin films of the heusler alloy co 2 mnsi. *Appl. Phys. Lett.*, 84(13):2367–2369, 2004.

[99] S Picozzi, AJFA Continenza, and Arthur J Freeman. Role of structural defects on the half-metallic character of co 2 mnge and co 2 mnsi heusler alloys. *Phys. Rev. B*, 69(9):094423, 2004.

[100] Xin-Yi Wang, Lu Wang, Zhe-Ming Wang, Gang Su, and Song Gao. Coexistence of spin-canting, metamagnetism, and spin-flop in a (4, 4) layered manganese azide polymer. *Chem. Mater.*, 17(25):6369–6380, 2005.

[101] Takafumi Akiho, Jinhai Shan, Hong-xi Liu, Ken-ichi Matsuda, Masafumi Yamamoto, and Tetsuya Uemura. Electrical injection of spin-polarized electrons and electrical detection of dynamic nuclear polarization using a heusler alloy spin source. *Phys. Rev. B*, 87(23):235205, 2013.

[102] M Jourdan, J Minár, J Braun, A Kronenberg, S Chadov, B Balke, A Gloskovskii, M Kolbe, HJ Elmers, G Schönhense, et al. Direct observation of half-metallicity in the heusler compound co2mnsi. *Nature communications*, 5, 2014.

[103] B Pradines, R Arras, I Abdallah, N Biziere, and L Calmels. First-principles calculation of the effects of partial alloy disorder on the static and dynamic magnetic properties of co 2 mnsi. *Phys. Rev. B*, 95(9):094425, 2017.

[104] Ashutosh Rath, Chockalingam Sivakumar, C Sun, Sahil J Patel, Jong Seok Jeong, J Feng, G Stecklein, Paul A Crowell, Chris J Palmstrøm, William H Butler, et al. Reduced interface spin polarization by antiferromagnetically coupled mn segregated to the c o 2 mnsi/gaas (001) interface. *Phys. Rev. B*, 97(4):045304, 2018.

[105] PJ Webster. Magnetic and chemical order in heusler alloys containing cobalt and manganese. *J. Phys. Chem. Solids*, 32(6):1221–1231, 1971.

[106] PJ Brown, KU Neumann, PJ Webster, and KRA Ziebeck. The magnetization distributions in some heusler alloys proposed as half-metallic ferromagnets. *Journal of Physics: Condensed Matter*, 12(8):1827, 2000.

[107] R Yilgin, M Oogane, Y Ando, and T Miyazaki. Gilbert damping constant in polycrystalline co 2 mnsi heusler alloy films. *Journal of Magnetism and Magnetic Materials*, 310(2):2322–2323, 2007.

[108] Kidist Moges, Yusuke Honda, Hong-xi Liu, Tetsuya Uemura, Masafumi Yamamoto, Yoshio Miura, and Masafumi Shirai. Enhanced half-metallicity of off-stoichiometric quaternary heusler alloy c o 2 (mn, fe) si investigated through saturation magnetization and tunneling magnetoresistance. *Physical Review B*, 93(13):134403, 2016.

[109] YV Stadnik and RV Sklozdra. Magnetic-properties of me6ni16 (si, ge) 7 compounds (me-transition metals of iva-viia subgroups. *Ukr. Fiz. Zh.*, 28(7):1031–1035, 1983.

[110] P.I.; Kuz'ma Yu.B Gladyshevskii, E.I.; Kripyakevich. *Dopovidi Akademii Nauk Ukrains'koi RSR*, 1956:121–124, 1956.

[111] E. I. Gladyshevskii Y. B. Kuzma and E. E. Cherkashin. *Russ. J. Inorg. Chem.*, 9: 1028, 1964.

[112] DI Bardos, RK Malik, FX Spiegel, and Paul A Beck. Beta-manganese phases in ternary systems of transition elements with silicon, germanium, or tin. *AIME MET SOC TRANS*, 236(1):40–48, 1966.

[113] Biao Hu, Honghui Xu, Shuhong Liu, Yong Du, Cuiyun He, Chunsheng Sha, Dongdong Zhao, and Yingbiao Peng. Experimental investigation and thermodynamic modeling of the mn–ni–si system. *Calphad*, 35(3):346–354, 2011.

[114] DI Bardos, KP Gupta, and Paul A Beck. Ternary laves phases with transition elements and silicon. *Trans. Met. Soc. AIME*, 221, 1961.

[115] AM Bardos, PA Beck, and DI Bardos. Effective atomic radius of silicon in ternary laves phase alloys. *Trans. Metall. AIME*, 227(4):991, 1963.

[116] EM Savitskii, VV Baron, Yu V Efimov, and EI Gladyshevskii. Investigation of the structure and properties of alloys in the v 3 si-v 3 sn system. *IZV AKAD NAUK SSSR NEORGAN MATERIALY*, 1(2):208–210, 1965.

[117] V Ya Markiv, EI Gladyshevskii, PI Kripyakevich, and TI Fedoruk. The titanium-nickel-silicon system. *IZV AKAD NAUK SSSR NEORGAN MATERIALY*, 2(7):1317–1319, 1966.

[118] W. Hume-Rothery. *Trans. Metall. Sot. AIME,*, 233:848, 1965.

[119] Yukitomo Komura. Stacking faults and two new modifications of the laves phase in mg–cu–al system. *Acta Crystallogr.*, 15(8):770–778, 1962.

[120] Y Komura and K Tokunaga. Structural studies of stacking variants in mg-base friauf–laves phases. *Acta Crystallographica Section B: Structural Crystallography and Crystal Chemistry*, 36(7):1548–1554, 1980.

[121] AV Skripov, M Pionke, O Randl, and R Hempelmann. Quasielastic neutron scattering study of hydrogen motion in c14-and c15-type zrcr2hx. *J. Phys.: Condens. Matter*, 11(6):1489, 1999.

[122] AV Irodova and E Suard. Order–disorder phase transition in the deuterated hexagonal (c14-type) laves phase zrcr2d3. 8. *J. Alloys Compd.*, 299(1-2):32–38, 2000.

[123] KF Kelton, GW Lee, A Kt Gangopadhyay, RW Hyers, TJ Rathz, JR Rogers, MB Robinson, and DS Robinson. First x-ray scattering studies on electrostatically levitated metallic liquids: demonstrated influence of local icosahedral order on the nucleation barrier. *Phys. Rev. Lett.*, 90(19):195504, 2003.

[124] AV Skripov. Hydrogen diffusion in laves-phase compounds. In *Defect and Diffusion Forum*, volume 224, pages 75–92. Trans Tech Publ, 2004.

[125] Hua Wu, Peter Kratzer, and Matthias Scheffler. First-principles study of thin magnetic transition-metal silicide films on si (001). *Physical Review B*, 72(14):144425, 2005.

[126] AT Zayak, WA Adeagbo, P Entel, and KM Rabe. e/ a dependence of the lattice

instability of cubic heusler alloys from first principles. *Applied physics letters*, 88 (11):111903, 2006.

[127] Qing-Long Fang, Jian-Min Zhang, Xu-Mei Zhao, Ke-Wei Xu, and Vincent Ji. Magnetic properties and possible martensitic transformation in mn 2 nisi and ni 2 mnsi heusler alloys. *Journal of Magnetism and Magnetic Materials*, 362:42–46, 2014.

[128] Wei Wang, She-Sheng Gao, and Yang Meng. First-principle investigations of the magnetic properties and possible martensitic transformation in ni2mnx (x= al, ga, in, si, ge and sn). *Journal of Magnetism and Magnetic Materials*, 371:135–138, 2014.

[129] Anton O Oliynyk, Erin Antono, Taylor D Sparks, Leila Ghadbeigi, Michael W Gaultois, Bryce Meredig, and Arthur Mar. High-throughput machine-learning-driven synthesis of full-heusler compounds. *Chem. Mater.*, 28(20):7324–7331, 2016.

[130] U Adem, I Dincer, S Aktürk, M Acet, and Y Elerman. Phase formation characteristics and magnetic properties of bulk ni2mnge heusler alloy. *J. Alloys Compd.*, 618: 115–119, 2015.

[131] Jan Czochralski. A new method for the measurement of the crystallization rate of metals. *Zeitschrift für physikalische Chemie*, 92:219–221, 1918.

[132] William Henry Bragg, BA WL Bragg, et al. The reflection of x-rays by crystals. *Proc. R. Soc. Lond. A*, 88(605):428–438, 1913.

[133] PP Ewald. Introduction to the dynamical theory of x-ray diffraction. *Acta Crystallographica Section A: Crystal Physics, Diffraction, Theoretical and General Crystallography*, 25(1):103–108, 1969.

[134] Arthur L Patterson. A direct method for the determination of the components of interatomic distances in crystals. *Zeitschrift für Kristallographie-Crystalline Materials*, 90(1):517–542, 1935.

[135] James F. Britten and Weiguang Guan. *IUCr Commun. Cryst. Comput., Newsl.*, 8:96, 2007.

[136] Gt M Sheldrick. shelxs 97, program for the solution of crystal structure, 1997.

[137] Juan Rodriguez-Carvajal. Fullprof: a program for rietveld refinement and pattern matching analysis. In *satellite meeting on powder diffraction of the XV congress of the IUCr*, volume 127. Toulouse, France:[sn], 1990.

[138] Juan Rodríguez-Carvajal. Recent developments of the program fullprof. *Commission on powder diffraction (IUCr). Newsletter*, 26:12–19, 2001.

[139] J Rodriguez-Carvajal. Fullprof. 2k. *Computer program, Version*, 2011.

[140] AS Wills. A new protocol for the determination of magnetic structures using simulated annealing and representational analysis (sarah). *Physica B*, 276:680–681, 2000.

[141] James Chadwick. The existence of a neutron. *Proceedings of the Royal Society of London. Series A*, 136(830):692–708, 1932.

[142] Sem introduction: an overview of scanning electron microscopy. `https://www.understanding-cement.com/sem-introduction.html`, 2005-2018.

[143] Sriram Subramaniam, Werner Kühlbrandt, and Richard Henderson. Cryoem at iucrj: a new era. *IUCrJ*, 3(Pt 1):3, 2016.

[144] YC Liu, F Sommer, and EJ Mittemeijer. Calibration of the differential dilatometric measurement signal upon heating and cooling; thermal expansion of pure iron. *Thermochim. Acta*, 413(1-2):215–225, 2004.

[145] G Mohapatra, F Sommer, and EJ Mittemeijer. Calibration of a quenching and deformation differential dilatometer upon heating and cooling: Thermal expansion of fe and fe–ni alloys. *Thermochim. Acta*, 453(1):31–41, 2007.

[146] G Mohapatra, F Sommer, and EJ Mittemeijer. The austenite to ferrite transformation of fe–ni under the influence of a uniaxially applied tensile stress. *Acta Mater.*, 55 (13):4359–4368, 2007.

[147] A Verma, M Sundararaman, JB Singh, and SA Nalawade. A new method for determining the curie temperature using a dilatometer. *Meas. Sci. Technol.*, 21(10): 105106, 2010.

[148] Georg Kresse and Jürgen Hafner. Ab initio molecular dynamics for liquid metals. *Phys. Rev. B*, 47(1):558, 1993.

[149] Georg Kresse and Jürgen Furthmüller. Efficient iterative schemes for ab initio total-energy calculations using a plane-wave basis set. *Phys. Rev. B*, 54(16):11169, 1996.

[150] Erwin Schrödinger. An undulatory theory of the mechanics of atoms and molecules. *Phys. Rev.*, 28(6):1049, 1926.

[151] M. Born and R. Oppenheimer. Zur quantentheorie der molekeln. *Annalen der Physik*, 389(20):457–484, 1927. ISSN 1521-3889.

[152] D. R. Hartree. The wave mechanics of an atom with a non-coulomb central field. part i. theory and methods. *Mathematical Proceedings of the Cambridge Philosophical Society*, 24:89–110, 1928. ISSN 1469-8064.

[153] Vladimir Fock. Näherungsmethode zur lösung des quantenmechanischen mehrkörperproblems. *Zeitschrift für Physik*, 61(1-2):126–148, 1930.

[154] Pierre Hohenberg and Walter Kohn. Inhomogeneous electron gas. *Phys. Rev.*, 136 (3B):B864, 1964.

[155] W. Kohn and L. J. Sham. Self-consistent equations including exchange and correlation effects. *Phys. Rev.*, 140:A1133–A1138, 1965.

[156] John P Perdew, Kieron Burke, and Matthias Ernzerhof. Generalized gradient approximation made simple. *Phys. Rev. Lett.*, 77(18):3865, 1996.

[157] Aliaksandr V Krukau, Oleg A Vydrov, Artur F Izmaylov, and Gustavo E Scuseria. Influence of the exchange screening parameter on the performance of screened hybrid functionals. *J. Chem. Phys*, 125(22):224106, 2006.

[158] EI Gladyshevskii, PI Kripyakevich, M Yu Teslyuk, OS t Zarechnyuk, and Yu B Kuz'ma. Crystal structures of some intermetallic compounds. *Sov. Phys.-Crystallogr*, 6:207–208, 1961.

[159] Rudolf Sobczak. Magnetische messungen anheusler-phasen co 2 xy. *Monatshefte für Chemie/Chemical Monthly*, 107(4):977–983, 1976.

[160] KHJ Buschow, PG Van Engen, and R Jongebreur. Magneto-optical properties of metallic ferromagnetic materials. *J. Magn. Magn. Mater.*, 38(1):1–22, 1983.

[161] H Ido and S Yasuda. Magnetic properties of co-heusler and related mixed alloys. *Le Journal de Physique Colloques*, 49(C8):C8–141, 1988.

[162] Shinpei Fujii, Shoji Ishida, and Setsuro Asano. Electronic and magnetic properties of x2mn1-x v x si (x= fe and co). *J. Phys. Soc. Jpn.*, 63(5):1881–1888, 1994.

[163] G Bergerhoff and ID Brown. Inorganic crystal structure database. 1987.

[164] Y Kota and A Sakuma. First-principles study of electrical resistivity in co $_{2}$ mnsi compounds. *IEEE Trans. Magn.*, 47(10):4405–4408, 2011.

[165] Michael E Fisher. Relation between the specific heat and susceptibility of an antiferromagnet. *Philos. Mag.*, 7(82):1731–1743, 1962.

[166] Casey A Marjerrison, Cole Mauws, Arzoo Z Sharma, Christopher R Wiebe, Shahab Derakhshan, Chad Boyer, Bruce D Gaulin, and John E Greedan. Structure and magnetic properties of kruo4. *Inorg. Chem.*, 55(24):12897–12903, 2016.

[167] Xinlin Yan, A Grytsiv, P Rogl, V Pomjakushin, and Xiangxin Xue. On the crystal structure of the mn–ni–si g-phase. *Journal of Alloys and Compounds*, 469(1):152–155, 2009.

[168] Simon Foner. 9 - antiferromagnetic and ferrimagnetic resonance. In George T. Rado and Harry Suhl, editors, *Magnetism*, pages 383 – 447. Academic Press, 1963. ISBN 978-0-12-575301-2.

[169] Y Shapira and S Foner. Magnetic phase diagram of mn f 2 from ultrasonic and differential magnetization measurements. *Phys. Rev. B*, 1(7):3083, 1970.

[170] Y Shapira. Observation of antiferromagnetic phase transitions by ultrasonic techniques. *Journal of Applied Physics*, 42(4):1588–1594, 1971.

[171] LJ De Jongh. Lj de jongh and ar miedema, adv. phys. 23, 1 (1974). *Adv. Phys.*, 23: 1, 1974.

[172] Patrick A Lee and TV Ramakrishnan. Disordered electronic systems. *Rev. Mod. Phys.*, 57(2):287, 1985.

[173] T Bandyopadhyay and DD Sarma. Calculation of coulomb interaction strengths for 3d transition metals and actinides. *Phys. Rev. B*, 39(6):3517, 1989.